Alma Mater Studiorum · Università di Bologna

Scuola di Scienze
Corso di Laurea Magistrale in Fisica del Sistema Terra

Nocturnal Low-Level Jets over Complex Terrain: Driving Mechanisms and Analytical Modeling

Relatore:
Prof. Silvana Di Sabatino

Presentata da:
Luigi Brogno

Correlatori:
Dott. Francesco Barbano
Dott. Laura Sandra Leo

Sessione III
Anno Accademico 2019/2020

Abstract

Molti studi nell'ambito della Fisica dell'Atmosfera si sono focalizzati sull'analisi dei numerosi fenomeni di circolazione atmosferica a piccola scala e processi turbolenti nel PBL (planetary boundary layer, ovvero strato limite planetario) la cui formazione ed evoluzione è complicata dalla topografia. Fra i fenomeni più studiati e tuttora non ancora del tutto compresi, vi è la formazione di low-level jets (LLJs), cioè la presenza di venti molto forti confinati in uno strato molto sottile del PBL. In presenza di un LLJ, il profilo verticale di velocità del vento assume dunque la caratteristica forma di un nose (naso), con elevati gradienti di velocità in corrispondenza di esso e un rapido decadimento della velocità alle quote inferiori e superiori. Una deviazione da questo modello semplicato è rappresentata dalla formazione di double-nose LLJs (o multiple LLJs), cioè la simultanea presenza di due (o multipli) noses nel PBL. Analizzando dati rilevati in terreno complesso durante il progetto di ricerca MATERHORN, gli scopi dell'attuale studio sono di comprendere i meccanismi che guidano la formazione dei double-nose LLJs identificati usando nuovi criteri che aggiornano quelli già esistenti, e di verificare se l'evoluzione dei LLJs segue la dinamica delle oscillazioni inerziali attraverso due modelli proposti in letteratura. I criteri proposti in letteratura per identificare i LLJs e i multiple LLJs sono analizzati ed è proposto un nuovo criterio basato su soglie assolute e relative (cioè percentuali) applicate ai massimi di velocità. Anche un criterio di identificazione per i minimi di velocità è proposto per descrivere meglio la forma complessa dei multiple LLJs. Inoltre, la forma di ogni nose viene caratterizzata secondo la loro larghezza e simmetria definendo nuove variabili chiamate nose width (ampiezza del naso) e simmetry ratio (rapporto di simmetria). Questi nuovi criteri e variabili sono usati per analizzare Intensive Observing Periods (IOPs) quiescenti, in cui le condizioni di boundary-layer stabile durante la notte e la circolazione termica locale non sono alterate o guidate dal forcing sinottico. Durante questi IOPs, la formazione di un LLJ dovuto ad oscillazioni inerziali avviene tipicamente poche ore dopo il tramonto. Tuttavia, la struttura del LLJ può essere temporaneamente perturbata generando un double-nose LLJ. Due meccanismi di formazione sono identificati per i double-nose LLJs. Il wind-driven mechanism avviene quando i due noses sono associati a differenti masse d'aria che fluiscono una al di sopra dall'altra. Il wave-driven mechanism avviene quando una perturbazione alla superficie genera un'onda gravito-inertiale, la quale trasporta momento durante la sua propagazione. Momento è perso dal nose caratterizzante il LLJ ed è trasportato verso l'alto producendo un nose secondario. Questo studio è focalizzato sul wave-driven mechanism e sulla sua verifica attraverso l'analisi di specifici double-nose LLJs. Inoltre, l'evoluzione di LLJs guidata dalle oscillazioni inerziali è investigata attraverso due modelli proposti in letteratura. I modelli forniscono una rappresentazione simile dei LLJs osservati, concludendo che i LLJs sono ben simulati quando sono pienamente sviluppati.

Abstract

Several studies in the Atmospheric Physics have focused on the analysis of the numerous atmospheric circulation phenomena at the small scale and turbulent processes within the planetary boundary layer (PBL), whose formation and evolution is complicated by the topography. The Low-Level Jet (LLJ) is one of the most studied phenomena and it is not yet completely understood. The LLJ consists in the occurrence of strong winds within a thin layer of the PBL. When the LLJ occurs, the shape of the wind-speed profile is like a nose. It is characterised by large wind-speed gradients in correspondence of the nose and by a fast decay of the wind speed above and below it. A particular case which is different from this simplified model, is the formation of double-nose LLJs (or multiple LLJs), i.e. the simultaneous occurrence of two (or multiple) noses within the PBL. Analysing data retrieved in complex terrain during the MATERHORN field campaigns, the objectives of the current thesis are to understand the mechanisms which drive the formation of the double-nose LLJs identified using newly-proposed criteria that upgrade the already existing ones, and to verify if the evolution of the LLJs follows the inertial-oscillations dynamics through two models proposed in literature. The criteria proposed in literature to identify the LLJs and the multiple LLJs are analysed and a new one is proposed, based on absolute and relative (i.e. percentage) thresholds on the wind-speed maxima. An identification criterion for the wind-speed minima is also proposed to better detail the complex shape of the multiple LLJs. In addition, the nose shape is characterised in terms of width and symmetry defining new variables named nose width and symmetry ratio. These new criteria and variables are used to analyse quiescent Intensive Observing Periods (IOPs), in which nocturnal stable boundary-layer conditions and local thermal circulation are not altered or driven by synoptic forcing. During these IOPs, the formation of a LLJ due to inertial oscillations is typical few hours after the sunset. However, this LLJ structure can be temporary perturbed generating a double-nose LLJ. Two double-nose LLJ driving mechanisms are identified. The wind-driven mechanism is when the two noses are associated with different air masses flowing one on top of the other. The wave-driven mechanism is when a surface perturbation generates an inertial-gravity wave which transports momentum during its propagation. Momentum is lost by the LLJ nose and transported upward where a second one is generated. This study is focused on the wave-driven mechanism and its reliability is verified through specific double-nose LLJs analyses. Furthermore, the evolution of the LLJs driven by the inertial oscillations is investigated by means of two models retrieved from the literature. The models provides similar representation of the observed LLJs, concluding that the LLJs are well simulated when they are fully developed.

Contents

Chapter 1

Introduction

The Low-Level Jet (LLJ) is a thin stream of air in fast motion that occurs in the planetary boundary layer (PBL). Several phenomena have been identified as mechanisms that drive the LLJs formation. The main driving mechanism involving in LLJs formation within the nocturnal stable boundary layer is the inertial oscillations. The inertial oscillations are undamped oscillations around a nocturnal equilibrium wind vector, induced by the Coriolis force for the abrupt drop of the frictional terms during the evening transition, i.e. when the diurnal force balance is dismantled (Van de Wiel et al., 2010). The LLJ is usually characterised by a single wind-speed maximum, however some previous studies reported cases with more than a maximum (Hoecker 1963; Banta et al. 2002, 2004; Pichugina et al. 2007; Banta 2008; Tuononen et al. 2017). These cases are named multiple LLJs. The multiple LLJs consists in more thin streams of air in fast motion, usually addressed as noses. As the multiple LLJs are particular case of LLJs, limited studies have been found in literature concerning the mechanism that drives their formation and the implication of their occurrence on the local environment. As the LLJs, the multiple LLJs could have impact on many human activities like the aviation (Cole et al. 2000; Mamrosh et al. 2006) and the wind-energy production (Storm et al., 2009), or they could have implication on the human safety because they can interfere with the forest fire propagation (Charney et al., 2003) and with the transport of pollutants impacting the urban areas (Beyrich, 1994).
In the current thesis, LLJs and double-nose LLJs (multiple LLJs characterised by two noses) will be examined by means of measurements collected on complex terrain during the MATERHORN Program. This thesis aims to understand if the complex terrain could interfere with the LLJ dynamics and if it could contribute to the formation of double-nose LLJs. The attention is focused on the complex terrain because the 70% of the Earth surface is covered by slopes, valleys, canyons, escarpments, gullies and buttes. Only data retrieved during quiescent intensive observing periods (IOPs) are analysed because they are characterised by the establishment of stable nocturnal boundary-layer conditions and the dynamics is dominated by the local thermal circulation limiting the influence of the synoptic scale. Since the objective to understand the mechanisms which drive the double-nose LLJs formation, these data are analysed with a newly-proposed criterion to identify

the LLJs and the multiple LLJs, starting from the ones previously proposed in literature. This criterion is based on absolute and relative (i.e. percentage) thresholds on the wind-speed maxima. Since limited criteria have been proposed in literature to identify the wind-speed minima, an identification criterion for them is also proposed to better detail the complex shape of the multiple LLJs. These new criteria will be used to identify and characterise the retrieved LLJs and double-nose LLJs. Specific double-nose LLJs analyses will be conducted to verify the identified mechanisms that drive their formation. Another objective of the current thesis is to verify if the evolution in complex terrain of the analysed LLJs follows the inertial-oscillations dynamics by means of two models retrieved from the literature.
After this Introduction, the current thesis is divided in 5 chapters, followed by the conclusions. Chapter 2 describes the theoretical background introducing the planetary boundary layer, especially the stable boundary layer, and the phenomena which occurs within it. This chapter reports the general features of the LLJs, as the mechanisms which drive their formation, the implication of their occurrence,the criteria proposed in literature for their identification. The last part of the chapter is dedicated to the models proposed in previous studies to describe the LLJ formation causes by the inertial-oscillations dynamics. Chapter 3 describes the field campaigns and the measurement site in which the analysed data were retrieved and the equipment which was used. This chapter also reports the preliminary data processing, conducted before the analyses reported in the subsequent chapters. Chapter 4 describes the newly-proposed criteria and variables, used to identify and classify the LLJ and the Multiple LLJs detected during the MATERHORN Program. This chapter also reports the identified double-nose LLJ driving mechanisms, i.e. the wind-driven mechanism and the wave-driven one. Chapter 5 describes the specific double-nose LLJs analyses conducted to verify the reliability of the wave-driven mechanism. Chapter 6 reports the comparison between the LLJ evolution observed in the spring quiescent IOPs and the evolution simulated through a flat-terrain model as the one proposed by Van de Wiel et al. (2010) and a sloped-terrain model as the one proposed by Shapiro and Fedorovich (2009). Chapter 7 summarises the analyses conducted in the current thesis and the obtained results.

Chapter 2

Theoretical Background

In this chapter the theoretical background concerning the stable boundary layer and the phenomena which can occur within it,as the sub-mesoscale motions and the low-level jets (LLJs), are discussed. Section 2.1 reports the general features of the planetary boundary layer. The features of the stable boundary layer, and the phenomena which can affect it, are described more in detail in Sect. 2.2. Section 2.3 reports the theoretical background on the inertial-gravity wave, which is a phenomenon that can occur in stable conditions. Section 2.4 describes the LLJs and the multiple LLJs, which are another phenomena typically observed in stable conditions. Section 2.5 reports the significant implications of the occurrence of LLJs and multiple LLJs. Section 2.6 describes the criteria proposed in literature to identify the LLJs and the multiple LLJs. Section 2.7 reports the main connections between the stable conditions with the occurrence and the features of the LLJs. Section 2.8 describes the theory proposed by Blackadar (1957) on the inertial oscillations as mechanism which drives the LLJ formation. This theory has been resumed and upgraded by a flat-terrain model proposed by Van de Wiel et al. (2010) (reported in Sect. 2.9) and by a sloped-terrain model proposed by Shapiro and Fedorovich (2009) (reported in Sect. 2.10).

2.1 The Planetary Boundary Layer

The planetary boundary layer (PBL) is the part of the troposphere in direct contact with the surface, reacting to surface variations of roughness and temperature on time scale of about an hour. The average thickness of this layer is 1 km, approximately the 10% of the troposphere. The boundary layer is dynamically different from the rest of the troposphere because the dynamics is driven by the viscosity and the radiative heating and cooling of the surface. The PBL is characterised by three-dimensional mainly isotropic turbulence induced by the interaction of the air masses with the roughness elements of the ground, sustained or suppressed by heat exchanges at the surface. This means that a mechanical and a thermal source of turbulence are established at the interface between ground and atmosphere. The mechanical source is due to the motion of the air masses over

a roughness surface and it is influenced by the roughness changes, especially over the sea in which the roughness is easily changed by the wave motion. This source generates eddies of relatively limited dimension. Instead, the thermal source generates eddies (named thermals) of larger dimension in which the driving force is the buoyancy, therefore their generation is connected with the difference in density between the air masses inside each thermal and the surrounding air masses. This source depends on the radiative heating and cooling, which are driven by the diurnal cycle. Figure 2.1 shows the diurnal cycle of the PBL. During the day, the boundary-layer is usually convective and characterised by

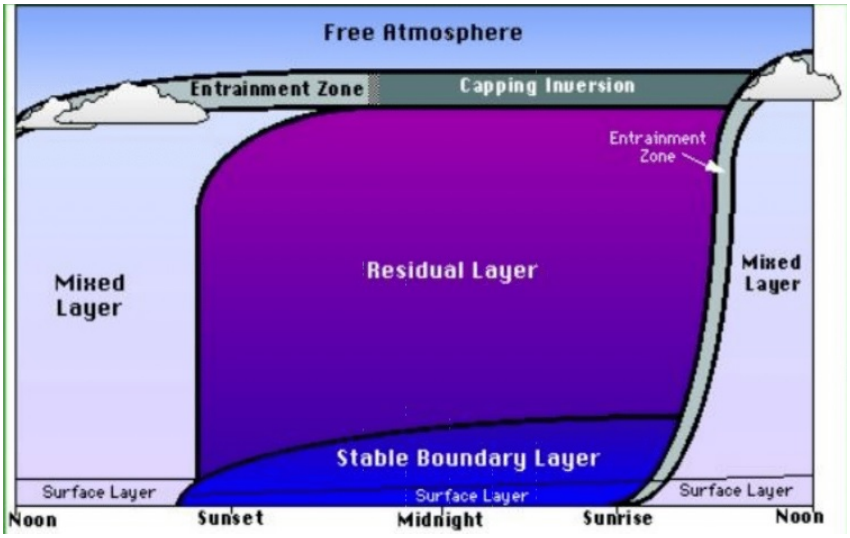

Figure 2.1: Scheme of the PBL diurnal cycle (Stull, 1988).

the generation of thermals, which erodes the atmosphere above increasing the thickness of the boundary layer until few kilometres of width. The convective boundary layer can be divided in three layers, namely from the ground to the boundary layer top: the surface layer, the mixed layer and the entrainment layer. The surface layer is in direct contact with the surface and generally represents the 10% of the boundary layer depth. Larger is the roughness of the surface, the higher the height at which the wind speed U (ms^{-1}) will be null for the presence of a rigid obstacle as the surface. This height is the roughness length z_0. Above it, the wind speed has a logarithmic increase within the surface layer as follow:

$$U = \frac{u_*}{k}\left[\ln\left(\frac{z}{z_0}\right) - \Psi_m\right], \tag{2.1}$$

in which $k = 0.4$ is the Von Karman constant and u_* (ms^{-1}) is the friction velocity, i.e. a characteristic scaling for the mechanical turbulence defined as

$$u_* = \sqrt{-\overline{u'w'}}, \tag{2.2}$$

where $\overline{u'w'}$ (m^2s^{-2}) is the turbulent kinetic momentum flux. Ψ_m is a correction that depends on the stability. In the convective case, this stability correction is:

$$\Psi_m = +2\ln\left(\frac{1+x}{2}\right) + \ln\left(\frac{1+x^2}{2}\right) - 2\arctan(x) + \frac{\pi}{2}, \tag{2.3}$$

where the parameter $x = \left(1 - \frac{15z}{L}\right)^{\frac{1}{4}}$ ((Stull, 1988)). The variable L is the Obukhov lenght (m), i.e. the height in which the thermal and the mechanical turbulence are equivalent in magnitude. It is defined as follow:

$$L = -\frac{\bar{\theta}}{kg}\frac{u_*^3}{\overline{w'\theta'}}, \tag{2.4}$$

in which g (ms^{-2}) is the gravitational acceleration, $\bar{\theta}$ (K) is the mean potential temperature and $\overline{w'\theta'}$ ($ms^{-1}K$) is the turbulent heat flux. As a consequence of the large wind-speed shear within the surface layer, the turbulence is mostly mechanically driven within it. In this layer, the temperature T (K) decreases with respect to the height more rapidly than the dry adiabatic (i.e. the temperature of a dry particle if it is moved without exchanges of heat with the surrounding environment). Therefore, the potential temperature θ (K) also decreases in this layer because it is the temperature of an air mass at pressure P (hPa) and temperature T (K) if this air mass is adiabatically moved at the height characterised by a standard reference pressure $P_0 = 1000\ hPa$. The potential temperature is given by:

$$\theta = T\left(\frac{P_0}{P}\right)^{\frac{R}{c_p}}, \tag{2.5}$$

in which $R = 287\ \frac{J}{kgK}$ is the gas constant and $c_p = 1004\ \frac{J}{kgK}$ the specific heat capacity of the dry air. The thermals develop within the mixed layer. The capacity of mixing is larger causing the potential temperature and the wind speed are approximately constant. Instead the entrainment layer is characterised by less powerful thermals, therefore the potential temperature and the wind speed tend to increase and the mixing with the free-atmosphere air masses is possible. During the sunset, the radiative heating ends, and the passage from the convective conditions to the stable ones is verified. This phase is named evening transition. During this phase, the beginning of the surface radiative cooling coincides with the formation of a stable boundary layer. It develops from the surface and grows during the night reaching a thickness of few tens to few hundreds metres. The rest of the atmosphere affected by the convective boundary layer during the day is characterised by the decay of the thermals and of their mixing effect. This layer is named residual layer and it is characterised by residual convection in rapidly decay. Instead, the stable boundary layer can be characterised by local strong shear of wind speed with consequent development of intermittent turbulence. However, a shallow surface layer is maintained in which mechanical turbulence is generated by shear at the surface. In this layer, the wind speed increases with the height following a logarithmic

Figure 2.2: Example of stable boundary layer during the MATERHORN Program (Fernando et al. 2015; University of Utah 2017).

equation Eq. (2.1) in which the stability correction is linear ((Stull, 1988)):

$$\Psi_m = -4.7\frac{z}{L}. \tag{2.6}$$

When the wind in free atmosphere are weak and the sky is clear supporting a large cooling of the surface (Fig. 2.2), the stable boundary layer can be characterised by a strong stratification. If the stratification is strong, the surface cannot longer be connected to the higher part of the stable boundary layer. When this decoupling occurs, the stable boundary layer is classified as upside-down boundary layer. It is characterised by the formation of a low-level jet (LLJ), which is a thin stream of hair in fast motion. The turbulent momentum can be locally transported upwards above the LLJ wind-speed maximum and transported downwards below the maximum because of the occurrence of intermittent turbulence. The sunrise represents the end of the described diurnal cycle. This phase is named morning transition after which the convective boundary layer is re-established. Obviously, a neutral boundary layer is possible too, as during cloudy day in which the radiative heating is too low to develops strong thermals. The neutral stable boundary layer is mainly characterised by mechanical turbulence generated by shear at the surface and its height is usual of hundred metres.

2.2 The Stable Boundary Layer

The stable boundary layer is characterised by intermittent turbulence and various non-turbulent sub-mesoscale motions, including wavelike motion characterised by a broad range of amplitudes and periods. Intermittent turbulence means turbulence variability, i.e. the temporal and spatial appearance of turbulence patches (Mahrt, 1989). Using the definition of the atmospheric scale proposed by Orlanski (1975) and reported in Appendix A, Mahrt (2009) defined the sub-mesoscale motions as motions with dimensions between the Micro-α scale (order of hundred metres) and the Meso-γ scale (order of few thousand kilometres). These motions can have various structures as steps, ramps, pulses, waves or complex signature that cannot be approximated by a single shape (Mahrt 2010; Belušić and Mahrt 2012; Kang et al. 2014). Many studies focused on the interaction between turbulence with the sub-mesoscale motions (for example Staquet and Sommeria (2002)), both to understand how sub-mesoscale motions lead turbulence and how turbulence influences the evolution of the sub-mesoscale motions. The interaction between turbulence and sub-mesoscale motions represents a mechanism to generate newly intermittent turbulence. However, this interaction is not fully understood in a stably stratified flow limiting the numerical prediction of the intermittent turbulent events in stable boundary layers. These events are critically important because they influence the momentum, energy, heat and pollutant transports. For example fog and frost formation depends on intermittent heat transport near the surface or high concentrations of pollutants trapped near the ground can be decreased by intermittent turbulent events within the stable boundary layer (Sun et al., 2015). Despite the mechanism to generate intermittent turbulence is not well understood, the sub-mesoscale motions can also create sufficient shear to generate local turbulence patches (Baklanov et al. 2011; Mahrt et al. 2012). Some sub-mesoscale motions are the wavelike motions which are ubiquitous in the stable boundary layer. They can be divided in two categories according to the restoring force: the buoyancy waves as the gravity waves or the inertial-gravity waves, and the vorticity waves as the Kelvin-Helmholtz billows. Figure 2.3 shows the general scheme of the wave generation for both the category. The buoyancy waves are usually due to a vertical displacement of the flow streamlines in a stratified laminar fluid. This displacement can be resulted by the interaction of the flow with another one, with a physical obstacles as the topography, or with an interface characterising by a different density as a cold pool, a density current or a local convective system. The buoyancy is the restoring force and acts causing a periodic energy exchange between potential and kinetic energy generating a wind-speed oscillations. The temperature can also oscillate out of phase with the wind speed. The buoyancy waves can modify the local conditions within the stable boundary layer redistributing a large amount of energy and momentum or break down generating intermittent turbulence in time and space. The vorticity waves derives by initial wave disturbance that can grow rapidly for the non-linearity terms developing a periodic vortex sheet (i.e. vertically confined periodic transverse vortices) and periodic large transverse roll (Drazin, 2002). The vorticity waves are transverse because they are characterised by vorticity in the crosswind direction. The initial wave disturbance is generally caused by a shear instability at the

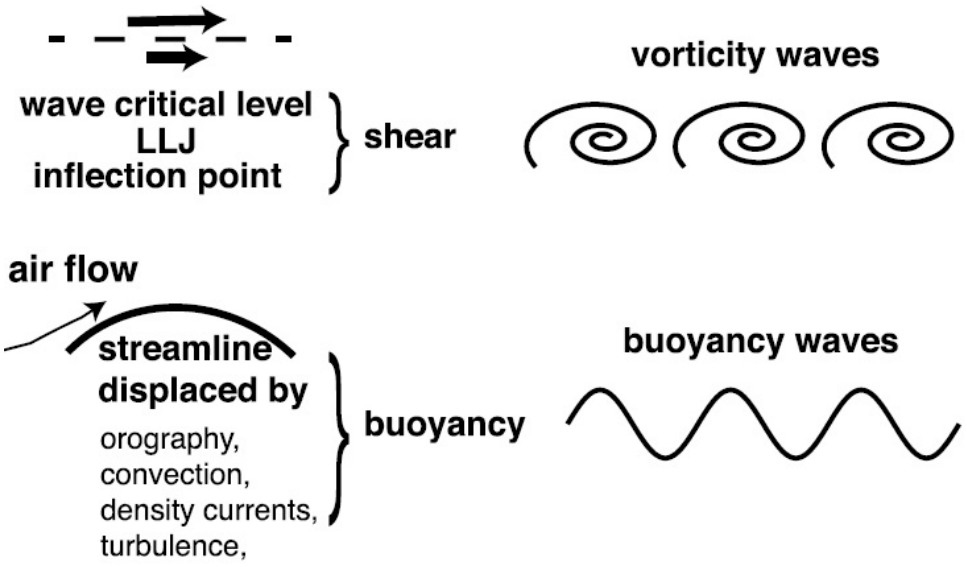

Figure 2.3: Scheme of the wave generation for buoyancy and vorticity waves (Sun et al., 2015).

critical level established by another wave, or to the presence of a LLJ or a local inflection point. The critical level is the height at which the mean wind-speed flow is equal to the wave phase speed. It is involved in wave generation and wave property changes as wave dissipation or breaking. The buoyancy can also have a role in the vorticity-wave formation, as in Kelvin-Helmholtz billows in which the overturning of a stably stratified flow is also relevant. Indeed, Kelvin-Helmholtz billows are interface waves driven by the nonlinear expansion of a vortex sheet previously due to shear instability between a stratified layer causing density jumps. The disturbance grows until it generates vortex rolls. Likewise the buoyancy waves, the vorticity waves can generate intermittent turbulence because they can lead turbulence embedded in each transverse vorticity roll characterising these waves.

2.3 The Inertial-Gravity Wave

An inertial-gravity wave is a gravity wave characterised by a wavelength large enough to be affected by the planetary rotation. Therefore, both the fluid stratification and the planetary rotation are restoring force of the inertial-gravity wave. It is a transverse wave, i.e. the wave oscillations occur perpendicular to the direction of the wave travel, and a dispersive wave, i.e. the wave is formed by the superposition of waves characterised by different wavelengths and these waves will disperse during their motion through the space at different phase velocities. The phase velocity describes the propagation of the phase in the space, therefore the propagation of each crest and trough, while the group velocity describes the propagation of the energy. These two velocities are perpendicular in an inertial-gravity wave. The concepts reported in this section will be resumed in Sect.

4.3 in which a double-nose LLJ driving mechanism connected to the mean-momentum transport by an inertial-gravity wave is proposed, and in Sect. 5.2 in which the reliability of this driving mechanism will be proved. To find the dispersion relation of the inertial-gravity wave, the incompressible continuity and the momentum equations of the turbulent wind-speed components (highlighted by the apostrophe as superscript) are considered:

$$\frac{\partial u^{'}}{\partial x} + \frac{\partial v^{'}}{\partial y} + \frac{\partial w^{'}}{\partial z} = 0 \tag{2.7a}$$

$$\frac{\partial u^{'}}{\partial t} = -\frac{1}{\rho}\frac{\partial P^{'}}{\partial x} + f v^{'} \tag{2.7b}$$

$$\frac{\partial v^{'}}{\partial t} = -\frac{1}{\rho}\frac{\partial P^{'}}{\partial y} - f u^{'} \tag{2.7c}$$

$$\frac{\partial w^{'}}{\partial t} = -\frac{1}{\rho}\frac{\partial P^{'}}{\partial z} - \frac{\rho^{\prime}}{\rho} g, \tag{2.7d}$$

where u, v and w (ms^{-1}) are the streamwise, the cross-stream and the vertical wind components respectively, ρ the air density (kgm^{-3}), P (hPa) the air pressure, g (ms^{-2}) the gravitational acceleration, f (s^{-1}) $= 2\Omega \sin(\phi)$ the Coriolis parameter, $\Omega = 7.29 \times 10^{-5}$ rads^{-1} the intrinsic frequency of Earth's rotation and ϕ the latitude. Using the first-order Taylor expansion, the perturbation of the air density can be written as

$$\rho^{'} = \frac{\rho}{g} N^2 \mathrm{d}z \tag{2.8}$$

in which $N = \sqrt{\frac{g}{\rho}\frac{\partial \rho}{\partial z}}$ (s^{-1}) is the Brunt-Väisälä frequency, i.e. the intrinsic frequency at which a vertically displaced air mass oscillates in a statically stable layer. Substituting Eq. (2.8) into Eq. (2.7d) and deriving with respect to time, it becomes

$$\frac{\partial^2 w^{'}}{\partial t^2} = -\frac{1}{\rho}\frac{\partial^2 P^{'}}{\partial z \partial t} - N^2 w^{'}. \tag{2.9}$$

The following sinusoidal equations are assumed as solutions of the equation system formed by Eqs. (2.7a), (2.7b), (2.7c) and (2.9):

$$u^{'} = A e^{i(k_x x + k_y y + k_z z - \omega t)} \tag{2.10a}$$

$$v^{'} = B e^{i(k_x x + k_y y + k_z z - \omega t)} \tag{2.10b}$$

$$w^{'} = C e^{i(k_x x + k_y y + k_z z - \omega t)} \tag{2.10c}$$

$$P^{'} = D e^{i(k_x x + k_y y + k_z z - \omega t)}, \tag{2.10d}$$

where $k = (k_x, k_y, k_z)$ (radm^{-1}) is the wavenumber and ω (rads^{-1}) the intrinsic frequency. Imposing the solutions into the equation system and solving for ω, the dispersion relation of the inertial-gravity wave is obtained:

$$\omega = \sqrt{\frac{k_z^2 f^2 + k_H^2 N^2}{k^2}} \tag{2.11}$$

where $k_H = \sqrt{k_x^2 + k_y^2}$ (radm^{-1}) and $k = \sqrt{k_H^2 + k_z^2}$ (radm^{-1}) are respectively the horizontal and total wavenumber. Therefore,

$$k_H = k\cos(\phi) \tag{2.12}$$

$$k_z = k\sin(\phi), \tag{2.13}$$

where ϕ (°) is the propagation angle. Substituting Eqs. (2.12), (2.13) into Eq. (2.11), the dispersion relation can be rewritten as

$$\omega = \sqrt{f^2\sin^2(\phi) + N^2\cos^2(\phi)}. \tag{2.14}$$

Inverting Eq. (2.14), a relation for the propagation angle is obtained:

$$\phi = \sqrt{\arccos\left(\frac{\omega^2 - f^2}{N^2 - f^2}\right)}, \tag{2.15}$$

in which the intrinsic frequency can be computed knowing the wave period T_w, through

$$\omega = \frac{2\pi}{T_w}. \tag{2.16}$$

When the propagation angle ϕ is approximately 90°, the momentum transport associated with the wave is vertical and the inertial-gravity wave transports momentum upward or downward. Following Kim and Mahrt (1992), internal inertial-gravity waves carry a wind momentum M_w (kgm^{-2}s^{-1}) equal to

$$M_w = \rho\sqrt{\frac{(wu, wv)\cdot(u, v)}{\mid U \mid}}, \tag{2.17}$$

where U (ms^{-1}) is the wind-speed vector and wu and wv (m^{2}s^{-2}) are the streamwise and cross-stream wave momentum fluxes, i.e. the fluxes of the horizontal wave momentum components along the vertical direction per unit of density. Instead, the horizontal and vertical wave phase velocities $c_{pH} = \sqrt{c_{px}^2 + c_{py}^2}$ and c_{pz} (ms^{-1}) can be obtained by

$$c_{pH} = \frac{\omega}{k_H} \tag{2.18}$$

$$c_{pz} = \frac{\omega}{k_z}. \tag{2.19}$$

The wave phase velocity is $c_p = \sqrt{c_{pH}^2 + c_{pz}^2}$. Finally, the wave group velocity is $c_g = \sqrt{c_{gH}^2 + c_{gz}^2}$ (ms^{-1}), in which $c_{gH} = \sqrt{c_{gx}^2 + c_{gy}^2}$ is the horizontal component and c_{gz} the vertical one. The horizontal and vertical wave group can be obtained by the following equations:

$$c_{gH} = \frac{(N^2 - f^2)\sin^2(\phi)\cos^2(\phi)}{\omega k_H} \tag{2.20}$$

$$c_{gz} = \frac{(N^2 - f^2)\sin^2(\phi)\cos^2(\phi)}{\omega k_z}. \tag{2.21}$$

These equations can be calculated deriving the dispersion relation, Eq. (2.14), with respect to each wavenumber component.

2.4 The Low-Level Jet

The Low-Level Jet (LLJ) (blue line, Fig. 2.4) is a worldwide phenomenon observed for the first time in the 1930s over Africa (Goualt 1938; Farquharson 1939). It consists in a thin stream of air in fast motion that occurs in the PBL. It can be supergeostrophic and it is often associated with extremely large wind shear in the low levels. As reported by Stull (1988), several studies concluded the LLJs can be characterised by width of hundreds kilometres and length of a thousand kilometres, therefore it can be more similar to a sheet that a narrow ribbon. Banta et al. (2002) showed by observational data measured during CASES-99 in three different sites in Kansas that the LLJ cannot be terrain following. Banta et al. (2002) found the wind-speed maximum is located at the same height above the sea level in the analysed three sites and they defined the LLJ as a sheet or an extensive layer of high-momentum flow established on large scale.

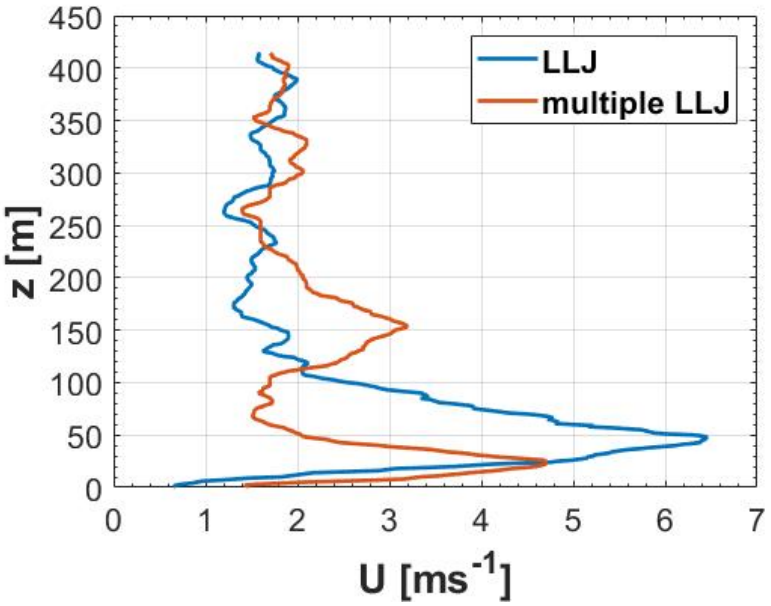

Figure 2.4: Esample of LLJ (blue line) and multiple LLJ (red line).

The LLJ is associated with the formation of the upside-down boundary layer during the nights in strongly stable conditions (Sect. 2.1). The upside-down boundary layer is characterised by intermittent turbulence episodes due to dynamic instabilities for the great

wind-speed shear. The turbulence is generated aloft and transported downward, in contrast with the traditional boundary layer in which it is generated at the surface. Wind tunnel experiments also confirmed this phenomenon (Ohya et al., 2008). The main driving mechanism associated with the LLJs formation in strongly stable conditions is the inertial oscillations. The inertial oscillations have been firstly theorised as driving mechanism for the LLJ formation by Blackadar (1957). Blackadar (1957) described them as undamped oscillations around the geostrophic wind vector above the planetary boundary layer induced by the Coriolis force for an abrupt annulment of the frictional terms after sunset when the diurnal force balance is dismantled. These oscillations are characterised by an amplitude equal to the ageostrophic wind component at sunset and period T (s)

$$T = 2\pi f^{-1}, \tag{2.22}$$

named inertial period. The maximum wind speed of these LLJs occurs during the predawn hours and they are also named Nocturnal Jets. Starting from this large-scale theory, Van de Wiel et al. (2010) recently assumes that inertial oscillations can also develop as a perturbation of a nocturnal equilibrium wind vector within the planetary boundary layer caused by the surface friction. The evolution of these inertial oscillations is characterised by the same period identified by Blackadar (1957) and has been considered to be the LLJ dynamics. Shapiro and Fedorovich (2009) analysed the case of inertial-gravity oscillations including the effects of the buoyancy on a gently planar slope in the formation theory proposed by Blackadar (1957). However, the inertial oscillations are not the only possible LLJ driving mechanism. A LLJ can be caused by other phenomena, including:

- synoptic-scale baroclinicity associated with weather patterns (Wexler 1961; Kotroni and Lagouvardos 1993; Whiteman et al. 1997)
- baroclinicity associated with sloping terrain (Holton 1967; Lettau 1967)
- fronts (Droegemeier and Wilhelmson 1987; Bowen 1996; Darby et al. 2002)
- advective accelerations (Paegle and Rasch, 1973)
- splitting, ducting and confluence around mountain barriers (Parish 1982; Stauffer and Warner 1987)
- land and sea breezes (Parish 2000; Orr et al. 2005; Ranjha et al. 2015)
- mountain and valley winds (Renfrew and Anderson, 2006).

The LLJs are usually characterised by a single wind-speed maximum, but cases with more than a maximum are reported in literature (Hoecker 1963; Banta et al. 2002, 2004; Pichugina et al. 2007; Banta 2008; Tuononen et al. 2017) and named multiple LLJs. Therefore, a multiple LLJ differs from a LLJ because it has more thin streams of air in fast motion, named noses, each characterised by a wind-speed maximum (red line, Fig. 2.4). Due to the very local and evanescent nature of this phenomenon, none ad-hoc field

campaign investigations have ever been conducted and multiple LLJ systems have been discovered from analyses of simple LLJs. However, multiple LLJs have been retrieved in literature since Hoecker (1963) using a pilot-balloon network stretching east to west from Little Rock (Arkansas) to Amarillo (Texas). Only Banta et al. (2002) proposed a theory to explain their formation. Banta et al. (2002) suggested that the multiple LLJs detected in the Great Plains could be due to inertial oscillations responding to different scales of horizontal pressure gradients, one more local and one with the dimension of the Great Plains.

2.5 Why Studying Low-Level Jets?

Studying the LLJs is important because they can influence many other phenomena in different field of studies as well reported in literature. Instead, limited investigations have been found in literature concerning the nature and the implication that a multiple LLJ dynamics can produce on the local environment. Being the multiple LLJs particular cases of LLJs with more than a single wind-speed maximum, they could have similar applications. As reported in literature, the LLJs can have an impact on human activities as the wind-energy production influencing the wind-power performances (Storm et al., 2009) or as the aviation, where LLJs affect the planes takeoff and landing because of the great shear in the first hundred metres above the surface and the possible consequent intermittent turbulence production (Cole et al. 2000; Mamrosh et al. 2006). Indeed the LLJs can cause clear-air turbulence influencing the turbulent exchange between the surface and the atmosphere (Banta et al. 2002, 2006; Conangla and Cuxart 2006). They can also have implication in human safety because they can modify the forest fire propagation (Charney et al., 2003) or the transport of pollutants over hundred of kilometres also impacting the urban area concentration (Beyrich, 1994) and of specific atmospheric constituents like ozone (Banta et al. 1998; Hu et al. 2013), carbon dioxide (Mathieu et al. 2005; Karipot et al. 2006) and dust (Fiedler et al., 2013). The intermittent turbulence associated with the presence of great shear inside the boundary layer can influence the vertical transport of pollutants causing spikes in pollutant concentration in the early morning hours (Clark et al., 2002). Moreover, the LLJs can transport fungi, pollen, spores, insects, among which allergen, agricultural pests and plant or animal pathogens (Drake and Farrow 1988; Wolf et al. 1990; Westbrook and Isard 1999; Isard and Gage 2001; Zhu et al. 2006; Westbrook 2008). The LLJs could affected the weather conditions influencing the weather patterns at the mesoscale or at the synoptic scale and the convective storm formation (Means 1952; Curtis and Panofsky 1958). For example, the Great Plains LLJs are connected with the nighttime maximum in storm formation in the Midwest United States (Pitchford and London 1962; Pu and Dickinson 2014). Furthermore, LLJs can transport moisture on considerable horizontal distances influencing the precipitation patterns and the hydrological cycle (Higgins et al., 1997), and the shear-driven turbulence caused by LLJs can transport aerosol and water vapour vertically influencing the cloud formation (Su et al., 2016). They can also influence the bird migration (Liechti and Schaller, 1999). Another

research field is the comprehension of how the LLJs influence the development and the intensity of the urban heat islands and how the urban heat islands influence the LLJ dynamics. Hu et al. (2013) studied the role of mixing in the nocturnal boundary layer during the formation of the urban heat island in Oklahoma City showing that the thermal contrast between the rural and the urban area is smaller in presence of a strong LLJ, the latter favouring mixing, while the temperature gradient is larger with relatively weak or absent LLJs. Before Hu et al. (2013), the study conducted by Wang et al. (2007) concluded the downtown of Oklahoma City causes the increase of $(25 \div 100)$ m of the LLJ wind-speed maximum height and the decrease of $(10 \div 15)$ % of the wind speed, while the direct transport of turbulent momentum flux from the LLJ nose to the street level is not remarkable. Finally, understanding Low-Level Jets is important to build parametrisation schemes to model the stable boundary layer, like Banta et al. (2003) showed that knowing correctly the bulk properties of the LLJ is essential to obtain realistic vertical turbulent mixing properties, but at the same time the parametrisation of turbulent diffusion is essential to simulate the LLJs.

2.6 Low-Level Jet Identification Criteria

Several criteria have been proposed in literature to identify the LLJs from the wind-speed profiles. Most of these criteria uses an absolute or relative (i.e. percentage) threshold on the wind-speed maximum because the main feature of LLJs is to be a thin stream of air in fast motion. Table 2.1 summarises the key studies where a LLJ identification criterion has been proposed and applied to field investigations. These criteria will be resumed in Sect. 4.1 upgrading them and proposing a new LLJ identification criterion. Blackadar (1957) was the first to propose a LLJ identification criterion consisting in an absolute threshold. The adopted threshold was empirically extrapolated from the analyses of pilot-balloon observations dislocated in several locations all over the United States. Another LLJ identification criterion has been proposed by Stull (1988). Stull (1988) resumed the criterion proposed by Blackadar (1957) lowering the absolute wind-speed threshold. Instead, Bonner (1968) decided to use a more restrictive criterion than the one proposed by Blackadar (1957) because Bonner (1968) analysed rawinsonde data in a particular site as the Great Plains, which is associated with large wind-speed maxima. Whiteman et al. (1997) extended the ranges of Bonner (1968) to include slower wind-speed maxima. Whiteman et al. (1997) also marked the end of the large scale investigations, when LLJs were searched up to 1500 m wind-speed profiles with radiosondes. Instead, the following studies have been conducted on flat terrain using "grounded" instrumentation mounted on ground stations, towers and tethered balloons, and focusing on the first 500 m of the wind-speed profiles. The first of these subsequent studies, was Andreas et al. (2000), which analysed tethered balloon soundings from the ice-covered western Weddel Sea during four months between the austral fall and the early winter, maintained the same absolute wind-speed threshold proposed by Stull (1988). Banta et al. (2002) lowered the absolute wind-speed threshold considering the better instrumental resolution of the

Nocturnal LLJ identification			
Authors	Criterion	Applied to	Used by
Blackadar (1957)	$U_{max} > 2.5$ ms^{-1} + U^a_{min}, Z range: 0 m - 1500 m	All LLJs	Hoecker (1963)
Bonner (1968)	$U_{max} \geq 12$ ms^{-1} and $U_{max} \geq 6$ ms^{-1} + U^a_{min}, $U_{max} \geq 16$ ms^{-1} and $U_{max} \geq 8$ ms^{-1} + U^a_{min}, $U_{max} \geq 20$ ms^{-1} and $U_{max} \geq 10$ ms^{-1} + U^a_{min}, Z range: 0 m - 1500 m	LLJs $U_{max} \geq 12$ ms^{-1}	Song et al. (2005), Hu et al. (2013), Vanderwende et al. (2015), Parish (2017),Carroll et al. (2019)
Whiteman et al. (1997)	$U_{max} \geq 10$ ms^{-1} and $U_{max} \geq 5$ ms^{-1} + U^a_{min} Z range: 0 m - 1500 m	LLJs $U_{max} \geq 10$ ms^{-1}	Lundquist and Mirocha (2008), Klein et al. (2014)
Stull (1988)	$U_{max} > 2$ ms^{-1} + U^a_{min}, Z range: 0 m - 1500 m	All LLJs	Kalverla et al. (2019)
Andreas et al. (2000)	$U_{max} \geq 2$ ms^{-1} + $U^{a,b}_{min}$, Z range: 0 m - 500 m	All LLJs	Delgado et al. (2015)
Banta et al. (2002)	$U_{max} \geq 1.5$ ms^{-1} + $U^{a,b}_{min}$ (threshold could be smaller according to instrumental precision) Z range: 0 m - 500 m	All LLJs	Kallistratova and Kouznetsov (2012) Banta et al. (2004), Pichugina et al. (2007), Banta (2008)
Baas et al. (2009)	A) $U_{max} \geq 2$ ms^{-1} + U^a_{min}, B) $U_{max} \geq 1.25 U^a_{min}$, Z range: 0 m - 500 m	A) LLJs, $U_{max} < 10$ ms^{-1} B) LLJs, $U_{max} \geq 10$ ms^{-1}	Tuononen et al. (2017)

Table 2.1: LLJ identification criteria from literature. Criteria are stored with the original application and the following studies that have adopted them. Studies where the criterion is used to identify multiple LLJ are highlighted in blue. Superscripts a and b indicate the wind-speed minimum computed respectively above or below the height of the wind-speed maximum.

equipment used in their study. Banta et al. (2002) analysed data from the Walnut River watershed (Kansas) measured with a profiler and a high-resolution doppler lidar during only one month of October. Finally, Baas et al. (2009) analysed data measured during seven years (taking measures in all the months) at Cabauw (Netherlands), a location characterised by meadows, fields and scattered villages. Baas et al. (2009) used propeller vanes and cup anemometers until 200 m above the surface and a profiler for the higher heights. Baas et al. (2009) considered the absolute wind-speed threshold proposed by Andreas et al. (2000) only for wind-speed maxima smaller than 10 ms^{-1} and introduced a wind-speed relative threshold for higher wind-speed maxima. The relative threshold has been introduced because the larger the wind-speed maximum is, the closer the absolute threshold to the measurement fluctuations will become. Despite the difference in sampling periods (different period of the year) and in measurement site (place and type of soil), these subsequent studies share the usual range of wind-speed maximum, which is between 6 ms^{-1} and 10 ms^{-1}, and the usual range of wind-speed maximum height, which is between 100 m and 200 m. Most importantly, these subsequent studies analysed LLJs caused by inertial oscillations (Blackadar 1957; Van de Wiel et al. 2010) on flat terrain. However, these criteria have been successfully applied to different measurement sites, sampling periods and LLJ formation mechanisms in other studies. For example, Delgado et al. (2015) analysed LLJs generated by baroclinicity on sloping terrain in Baltimore County (Maryland) applying the criterion formulated by Andreas et al. (2000).

2.7 Low-Level Jets and Stable Boundary Layer

The LLJ is a phenomenon typically associated with the formation of the upside-down boundary layer during the nights characterised by strong stratification (Sect. 2.1). However, the great shear due to the LLJ can supported the development of intermittent turbulence episodes. Many authors analysed the linkage between LLJ and stability, to understand both the best stability conditions for the LLJ formation and how the LLJ influence these conditions. Baas et al. (2009) classified the LLJs in terms of the geostrophic wind $\bar{U}_g = (\bar{u}_g, \bar{v}_g)$ (the bar indicates the mean components) and the radiative cooling (mainly determined by the cloudiness, type of soil and presence of vegetation), evaluated with parameters independent on the development of the stable boundary layer. The geostrophic wind is a good approximation of the wind in free atmosphere outside the tropics, its components are given by the balance between the Coriolis and the pressure gradient forces. The geostrophic equations are:

$$\bar{u}_g = -\frac{1}{f\rho}\frac{\partial \bar{P}}{\partial y} \tag{2.23}$$

$$\bar{v}_g = \frac{1}{f\rho}\frac{\partial \bar{P}}{\partial x}. \tag{2.24}$$

Using the radiative cooling and the geostrophic wind, Baas et al. (2009) obtained classes of stability valid during the nocturnal period and ranging from high geostrophic wind

and cloudy conditions (weakly-stable boundary layer) to clear sky and calm conditions (strongly stable boundary layer). In weakly-stable conditions the occurrence of LLJ is strongly lower than in strongly-stable conditions because for intense geostrophic forcing the turbulent mixing due to the shear preserves the coupling between the surface and the layer above. The LLJ occurrence rises with the increase of stability. However, the most stable class within the strongly-stable category (the class with the greatest radiative cooling and the lowest geostrophic wind) is characterised by a lowering of the LLJ occurrence because the wind-speed maximum occurs but it is too weak to be classify as a LLJ using the LLJ identification criteria (Sect. 2.6). Baas et al. (2009) supposed that in this case the ageostrophic wind components at the sunset are too small to produce significant inertial oscillations. This study also suggested that the supergeostrophic wind-speed maximum usually occurs in strongly-stable conditions. However, Banta (2008) highlighted the LLJs characterised by largest wind-speed maximum usually occur in weakly-stable conditions. Banta (2008) analysed data from the Great Plains and identified three regimes plotting the turbulence kinematic energy (TKE) in function of the bulk Richardson number. The TKE ($\mathrm{m^2 s^{-2}}$) is the mean kinetic energy per unit mass associated with the eddies in a turbulent flow and it is equal to

$$TKE = \frac{1}{2}\left(\overline{(u')^2} + \overline{(v')^2} + \overline{(w')^2}\right), \tag{2.25}$$

in which $\overline{u'}$, $\overline{v'}$, $\overline{w'}$ ($\mathrm{ms^{-1}}$) are the turbulent wind-speed components. The bulk Richardson number (R_B) is an approximation of the gradient Richardson number obtained evaluating the gradients through finite difference. It is evaluated to have information of stability and turbulence formation. Banta (2008) calculated the bulk Richardson number as follow:

$$R_B = \frac{gh}{\theta_m}\frac{\theta_h - \theta_0}{(U_h - U_0)^2}, \tag{2.26}$$

in which h (m) is the height of the stable boundary layer. The variables are evaluated at the top of the stable boundary layer (subscript h), at the ground (subscript 0), and at half height (subscript m). Fig. 2.5 shows the three regimes, which are the weakly-stable boundary layer (wSBL), the strongly-stable boundary layer (sSBL) and an intermediate one. As found by Baas et al. (2009) for the most strongly-stable class, during the strongly-stable regime the winds are less fast than 5 $\mathrm{ms^{-1}}$ in the first 200 m above the surface, therefore a jet structure occurs but the wind-speed maximum is too weak and the imposed LLJ identification criterion (Sect. 2.6) is not satisfied. Instead, the wind-speed maximum is typically in the range $(10 \div 15)$ $\mathrm{ms^{-1}}$ in the intermediate regime and other authors (as Van de Wiel et al. (2002)) have observed a cycle of stabilisation and acceleration-destabilisation that produces intermittent turbulence. Finally, the weak-stable regime is associated with LLJs characterised by wind-speed maximum larger than 15 $\mathrm{ms^{-1}}$ and turbulence due to the shear.

Another connection between LLJs and stratification analysed by different studies is the relation between the height of the stable boundary layer and of the LLJ wind-speed

maximum. Baas et al. (2009) concluded that the more stable the boundary layer is the closer to the surface the LLJ maximum will be. Baas et al. (2009) obtained that the LLJ is usually located at the top of the stable boundary layer, i.e. at the top of the nocturnal inversion. This relation between wind-speed maximum height and nocturnal inversion height was firstly obtained by Blackadar (1957). Figure 2.6 shows the retrieved linear relation analysing 88 cases detected at Drexel (Nebraska) using kite observations. However, other studies did not find the same result. Bonner (1968) and Whiteman et al. (1997) concluded that the LLJs classified as driven by inertial oscillations are usually above the inversion height, while they are within the stable boundary layer in Andreas et al. (2000). The same verification concerning the wind-speed maximum height will be proposed in Sect. 4.2. The stable boundary layer increases its depth during the night as the heat transfer to the ground cools the atmosphere increasing the stability. Blackadar (1957) suggested the LLJ tends to sustain the development of the nocturnal stable boundary-layer development if the LLJ wind-speed maximum is located at the same height of the stable boundary-layer top because this configuration prevents the generation of new intermittent turbulence which would destabilise the created equilibrium . Figure 2.7 shows the scheme (potential temperature versus height) used by Blackadar (1957) to verify this hypothesis. The solid line between A and B represents an idealised potential-temperature

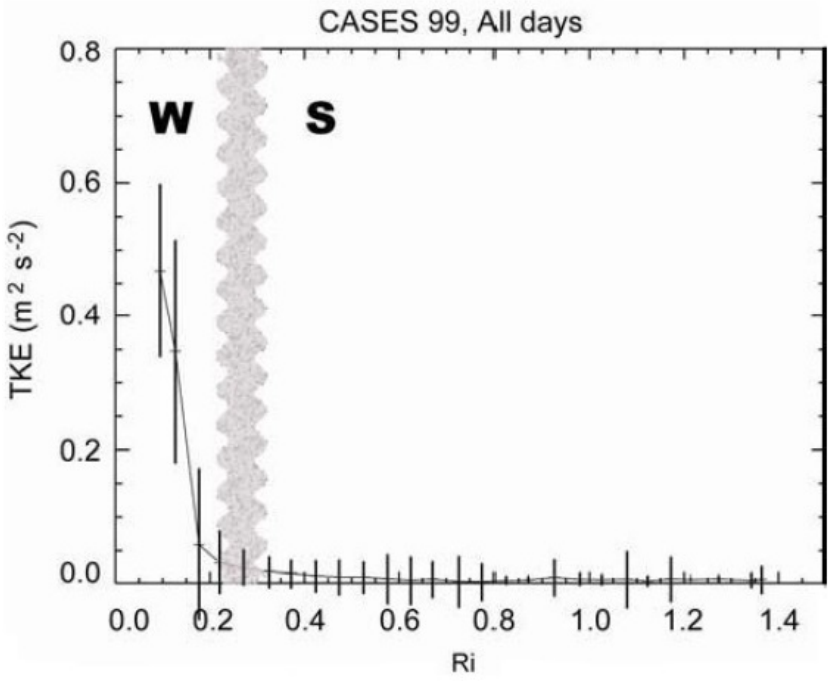

Figure 2.5: Plot of TKE versus R_B (Banta, 2008). R_B is evaluated by flux-tower data measured at 5 m and 55 m, while TKE using flux-tower data measured at 60 m and averaged for 0.05-wide bins of R_B using the technique describes in Banta et al. (2003). The vertical error bars indicates an error equal to the standard deviation in each bin. W indicates the weakly-stable regime, while S the strongly-stable regime.

profile and the dashed one between C and D the same profile after the action of a small amount of turbulent mixing. A stable boundary layer of thickness h is considered. In absence of external removal of heat, the action of a small amount of turbulent mixing causes the increasing of the surface potential temperature θ_0 of a quantity equal to $\mathrm{d}\theta_0$ and of the stable boundary layer height of a quantity equal to $\mathrm{d}h$. The height m, representing the height in which the potential temperature remains unchanged, is found equating the area AOC and DOB. When $\mathrm{d}h \ll h$ and $\frac{\mathrm{d}\theta}{\mathrm{d}z} \ll 1$ above the stable boundary layer, the following approximations are valid: $m = \frac{h}{2}$ and $\frac{\mathrm{d}\theta_0}{\mathrm{d}h} = \frac{\theta_h - \theta_0}{h}$, in which θ_h is the potential temperature at height h. The bulk Richardson number is evaluated through Eq. (2.26). In absence of other processes, the probability of further turbulence decreases if $\frac{\mathrm{d}R_B}{\mathrm{d}h} > 0$. Deriving Eq. (2.26) with respect to height, the following result is obtained:

$$\frac{\mathrm{d}R_B}{\mathrm{d}h} = \frac{gh}{\theta_m \left(U_h - U_0\right)^2} \left[\frac{\mathrm{d}\theta_h}{\mathrm{d}h} - 2 \frac{\theta_h - \theta_0}{\left(U_h - U_0\right)} \frac{\mathrm{d}U_h}{\mathrm{d}h} \right]. \tag{2.27}$$

Being positive the other quantities, the sign of Eq. (2.27) depends only on the signs of $\frac{\mathrm{d}\theta_h}{\mathrm{d}h}$ and $\frac{\mathrm{d}V_h}{\mathrm{d}h}$. Being $\mathrm{d}h \ll h$, the following approximation is enabled: $\frac{\mathrm{d}\theta_h}{\mathrm{d}h} = \frac{\theta_D - \theta_B}{\mathrm{d}h}$. This quan-

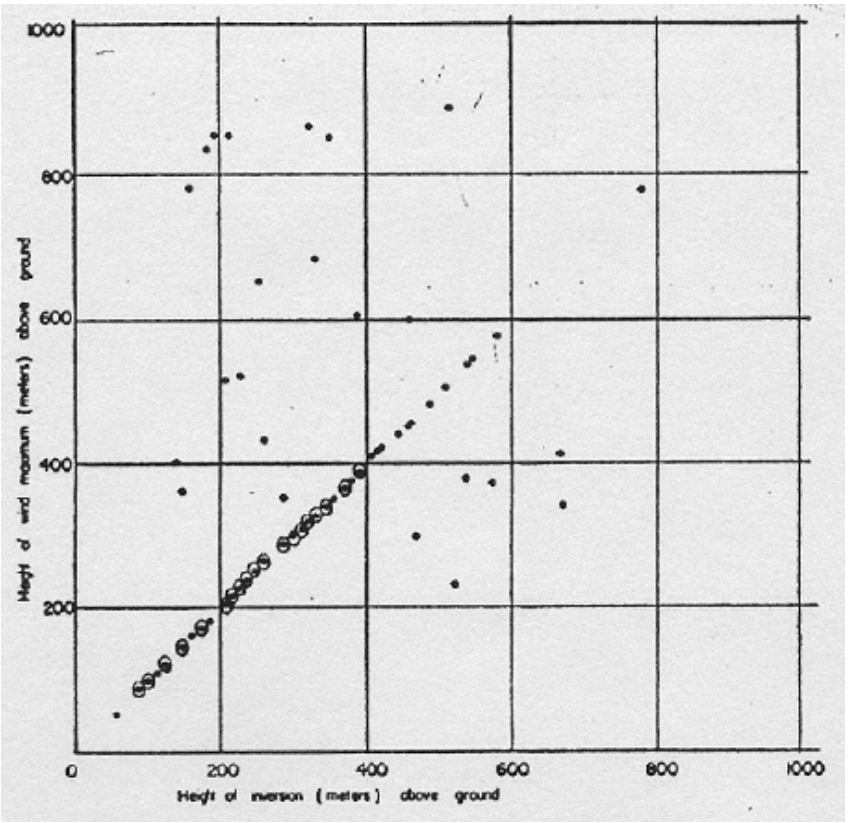

Figure 2.6: Comparison of the wind-speed maximum height and nocturnal inversion height using 88 cases of LLJs detected with kite observations at Drexel (nebraska) (Blackadar, 1957).

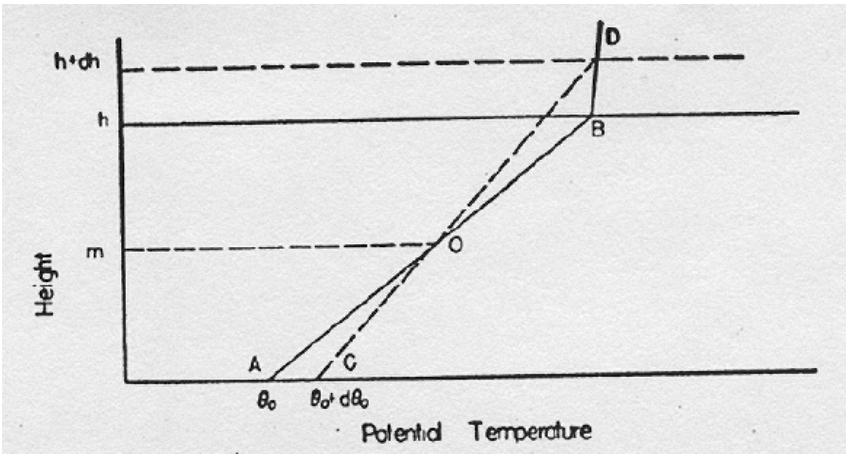

Figure 2.7: Potential temperature distribution in an idealised nocturnal inversion (solid line) and the corresponding distribution after a small amount of turbulent mixing (dashed line) (Blackadar, 1957).

tity is not likely significantly negative in the residual boundary layer, therefore to satisfy $\frac{dR_B}{dh} > 0$ is enough that the wind speed decreases with the height above the inversion, i.e. above the stable boundary layer. This condition is definitely verified when the wind-speed maximum is at the top of the stable boundary layer. Therefore, Blackadar (1957) verified that the intermittent turbulence is suppressed if the LLJ wind-speed maximum is located at the same height of the stable boundary layer top, while this suppression does not occur if the wind-speed maximum is above the stable boundary layer top.

2.8 The Blackadar's Theory

Blackadar (1957) proposed the theory of the inertial oscillations as driving mechanism for the LLJ formation. Blackadar (1957) suggested the LLJ starts to develop after the evening transition. During the evening transition, an abrupt annulment of the frictional terms occurs above the nocturnal boundary layer dismantling the diurnal force balance. The evening transition represents the passage from the convective regime, in which the winds are subgeostrophic, to a stable one characterised by the development of a stable boundary layer starting from the ground. As a consequence of the abrupt annulment of the turbulence, the Coriolis force induces undamped oscillations above the planetary boundary layer. These oscillations are addressed as inertial oscillations and they occurs around the geostrophic-wind vector, causing supergeostrophic winds during the night.
Blackadar (1957) started from the homogeneous momentum equations for the boundary

layer:

$$\frac{\partial \bar{u}}{\partial t} = -\frac{1}{\rho}\frac{\partial \bar{P}}{\partial x} + f\bar{v} - \frac{\partial \overline{u'w'}}{\partial z} \tag{2.28}$$

$$\frac{\partial \bar{v}}{\partial t} = -\frac{1}{\rho}\frac{\partial \bar{P}}{\partial y} - f\bar{u} - \frac{\partial \overline{v'w'}}{\partial z}, \tag{2.29}$$

where ρ is the air density (kgm^{-3}) and P (hPa) the air pressure. For simplicity, the geostrophic wind is chosen as $\bar{U}_g = (\bar{u}_g, \bar{v}_g = 0)$ and the viscous terms are rewritten as $\frac{\partial \overline{u'w'}}{\partial z} = fF_v$ and $\frac{\partial \overline{v'w'}}{\partial z} = fF_u$ where F_u and F_v are support variables with units of velocity. Constant pressure gradients are assumed and they are manipulated through the geostrophic equations Eqs. (2.23), (2.24) obtaining

$$\frac{\partial \bar{u}}{\partial t} = f\bar{v} - fF_u \tag{2.30}$$

$$\frac{\partial \bar{v}}{\partial t} = f\left(\bar{u}_g - \bar{u}\right) - fF_v. \tag{2.31}$$

The wind vector measured at the sunset, $\bar{U}_0 = (\bar{u}_0, \bar{v}_0)$, is used as initial condition to predict the nocturnal wind vector $\bar{U}_n = (\bar{u}_n, \bar{v}_n)$. Assuming a steady case during the day the following initial conditions are obtained:

$$\bar{u}_0 = \bar{u}_g - F_{v,0} \tag{2.32}$$

$$\bar{v}_0 = F_{u,0}. \tag{2.33}$$

Therefore, $F_{u,0}$ and $F_{v,0}$ represent the departure of the wind components from the geostrophic case. Blackadar (1957) assumed the annulment of the viscous terms above the boundary layer immediately after the sunset and they remain null all the night. However, to observe the evolution of the wind during the night, a steady case cannot be assumed. Imposing the assumptions and $\bar{U} = \bar{U}_n$ in the Eqs. (2.30), (2.31), the equations for the nocturnal wind components are:

$$\frac{\partial \bar{u}_n}{\partial t} = f\bar{v}_n \tag{2.34}$$

$$\frac{\partial \bar{v}_n}{\partial t} = f\left(\bar{u}_g - \bar{u}_n\right). \tag{2.35}$$

Deriving Eq. (2.34), substituting Eq. (2.35) into Eq. (2.34) and adding the null term $\frac{\partial^2 \bar{u}_g}{\partial t^2}$ to express the equation in terms of departure from the geostrophy, the following equation is obtained:

$$\frac{\partial^2\left(\bar{u}_n - \bar{u}_g\right)}{\partial t^2} = -f^2\left(\bar{u}_n - \bar{u}_g\right). \tag{2.36}$$

A solution can be chosen as:

$$\bar{u}_n - \bar{u}_g = Asin(ft) + Bcos(ft). \tag{2.37}$$

Substituting Eq. (2.37) into Eq. (2.35) and integrating, the solution for the meridional wind-speed component is:

$$\bar{v}_n = Acos(ft) - Bsen(ft). \tag{2.38}$$

Imposing the initial conditions, Eqs. (2.32),(2.33), the parameters are determined as $A = F_{u,0}$ and $B = -F_{v,0}$. The final solutions are

$$\bar{u}_n = \bar{u}_g + F_{u,0}sin(ft) - F_{v,0}cos(ft) \tag{2.39}$$
$$\bar{v}_n = F_{u,0}cos(ft) + F_{v,0}sen(ft). \tag{2.40}$$

The solutions suggest the wind can become supergeostrophic oscillating around the

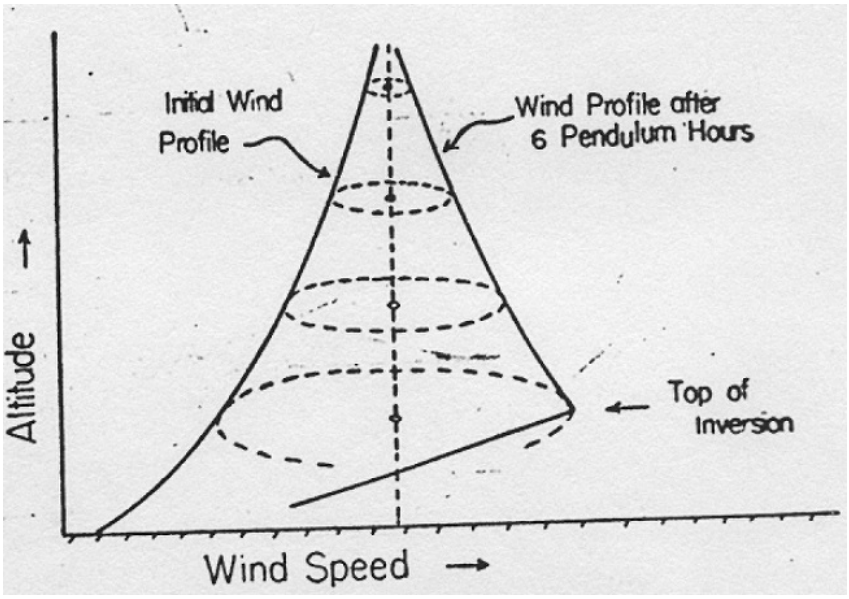

Figure 2.8: Schematic illustration explaining the formation of the LLJ applying the theory of Blackadar (1957).

geostrophic wind without collapsing into it. These oscillations are independent on the height and they are characterised by an amplitude equal to the ageostrophic wind at sunset. Being the period of inertial oscillations, named inertial period, equal to Eq. (2.22), it is about 17 h at the mid-latitudes and the wind-speed maximum is reached after a half period which usually occurs during the pre-down hours. Figure 2.8 shows the formation of the LLJ applying the theory proposed by Blackadar (1957) and the position of the wind-speed maximum at the top of the stable boundary layer. This theory cannot be applied inside the boundary layer because here the ageostrophic components are larger, therefore it would predict the wind-speed maximum at the ground not complying the no-slip condition.

2.9 The Van de Wiel's Model

Van de Wiel et al. (2010) improved the inertial-oscillations theory proposed by Blackadar (1957) introducing frictional effects within the nocturnal boundary layer. This model will be used in Chapter 6 to simulate the LLJs retrieved in the current thesis to prove that they follows the theory of the inertial oscillations.
As Blackadar (1957), the momentum equations in the boundary layer (Eqs. (2.28),(2.29)) are considered, assuming $\bar{U}_g = (\bar{u}_g, \bar{v}_g = 0)$ but defining $-\frac{\partial \overline{u'w'}}{\partial z} = F_x$ and $-\frac{\partial \overline{v'w'}}{\partial z} = F_y$, so:

$$\frac{\partial \bar{u}}{\partial t} = f\bar{v} + F_x \tag{2.41}$$

$$\frac{\partial \bar{v}}{\partial t} = f\left(\bar{u}_g - \bar{u}\right) + F_y. \tag{2.42}$$

Van de Wiel et al. (2010) assumes inertial oscillations can develop as a perturbation of a nocturnal equilibrium wind vector $\bar{U}_{eq} = (\bar{u}_{eq}, \bar{v}_{eq})$ defined imposing the steady solutions:

$$f\bar{u}_{eq} = f\bar{u}_g + F_{y,eq} \tag{2.43}$$

$$f\bar{v}_{eq} = -F_{x,eq}, \tag{2.44}$$

in which $F_{x,eq}$ and $F_{y,eq}$ are the viscous terms in the equilibrium nocturnal boundary layer. Furthermore, another change proposed by Van de Wiel et al. (2010) is the viscous terms are also constant at night, but they are not assumed null. They are equalled to the values assumed in the condition of equilibrium nocturnal boundary layer, so $F_x(z) = F_{x,eq}$ and $F_y(z) = F_{y,eq}$. Imposing the nocturnal wind vector $\bar{U}_n = (\bar{u}_n, \bar{v}_n)$ into Eqs. (2.41), (2.42) and adding respectively the null terms $-\frac{\partial \bar{U}_{eq}}{\partial t}$ and $-\frac{\partial \bar{V}_{eq}}{\partial t}$, the following equations are obtained:

$$\frac{\partial\left(\bar{u}_n - \bar{u}_{eq}\right)}{\partial t} = f\left(\bar{v}_n - \bar{v}_{eq}\right) \tag{2.45}$$

$$\frac{\partial\left(\bar{v}_n - \bar{v}_{eq}\right)}{\partial t} = -f\left(\bar{u}_n - \bar{u}_{eq}\right). \tag{2.46}$$

The solutions of Eqs. (2.45), (2.46) can be chosen as:

$$\bar{u}_n = \bar{u}_{eq} + Asin(ft) + Bcos(ft) \tag{2.47}$$

$$\bar{v}_n = \bar{v}_{eq} + Acos(ft) - Bsin(ft). \tag{2.48}$$

Imposing the initial condition $\bar{U}_0 = (\bar{u}_0, \bar{v}_0)$, the parameters are determined as $A = (\bar{v}_0 - \bar{v}_{eq})$ and $B = (\bar{u}_0 - \bar{u}_{eq})$. The solutions become:

$$\bar{u}_n = \bar{u}_{eq} + \left(\bar{v}_0 - \bar{v}_{eq}\right) sin(ft) + \left(\bar{u}_0 - \bar{u}_{eq}\right) cos(ft) \tag{2.49}$$

$$\bar{v}_n = \bar{v}_{eq} + \left(\bar{v}_0 - \bar{v}_{eq}\right) cos(ft) - \left(\bar{u}_0 - \bar{u}_{eq}\right) sin(ft). \tag{2.50}$$

The solution proposed by Blackadar (1957) is a particular solution with $\bar{u}_{eq} = \bar{u}_g$ and $\bar{v}_{eq} = 0$. The evolution of these inertial oscillations is characterised by the same period identified by Blackadar (1957) and these oscillations are also independent on the height. Moreover, these oscillations are undamped also considering non-null friction. Van de Wiel et al. (2010) explained this feature considering the friction is in phase with the Coriolis forces in this model.
In first approximation the Ekman solutions

$$\bar{u}_{Ek} = \bar{u}_g[1 - e^{-\gamma z} cos(\gamma z)] \tag{2.51}$$
$$\bar{v}_{Ek} = \bar{u}_g[e^{-\gamma z} sin(\gamma z)] \tag{2.52}$$

are chosen to represent both the equilibrium and the initial conditions. In these equations,

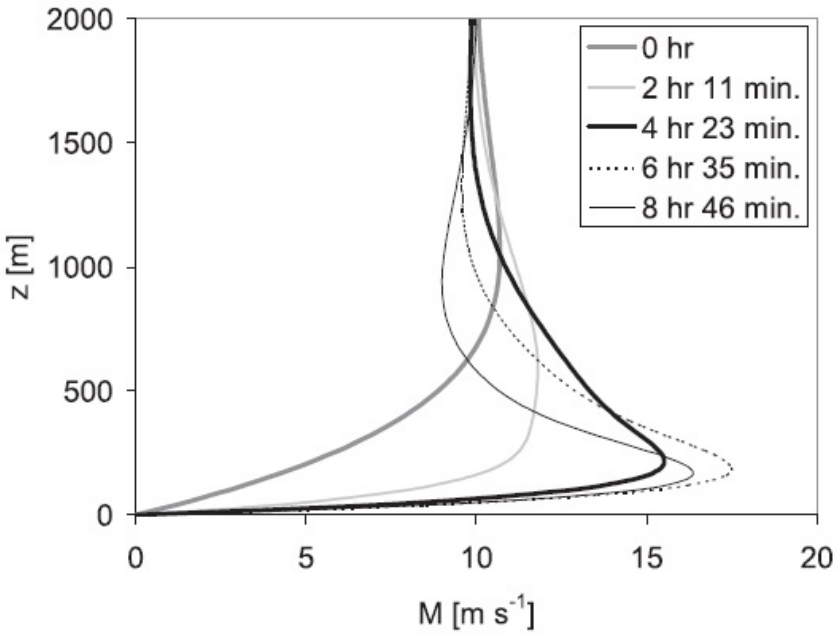

Figure 2.9: Evolution of the LLJ during the night obtained by the model of Van de Wiel et al. (2010) using the Ekman solutions as initial and nocturnal equilibrium conditions. The legend indicates the time after the sunset of each simulation.

γ is the scale depth of the boundary layer and it is defined as $\frac{1}{\gamma} = \sqrt{\frac{2K_m}{f}}$ in which K_m is the eddy viscosity, i.e. the turbulent diffusion coefficient for the momentum. To find the Ekman solutions (obtained in Appendix B), the viscous terms are parameterised assuming the turbulent momentum fluxes proportional to the mean wind-speed shear in analogy to the molecular diffusion. These flux-gradient relationship is an approximation in which the eddy diffusivity is assumed constant, however considering this constancy near the surface is a limitation of the model. The transition from the day to the night is parameterised by an abrupt change of the eddy viscosity. Van de Wiel et al. (2010) set $K_{m0} = 12.5$ $m^2 s^{-1}$ and $K_{mn} = 0.5$ $m^2 s^{-1}$. Using these values the ratio between the scale depth $\frac{\gamma_n}{\gamma_0} =$

5 is obtained. Using this first approximation, all the inertial oscillations are not driven only by the amplitude of the wind vector but also by the directional disequilibrium, indeed $\bar{u}_0 = \bar{u}_{eq}$ and $\bar{v}_0 = \bar{v}_{eq}$ is not verified at any height. Van de Wiel et al. (2010) obtained that, during the LLJ intensification, the layer interested by the LLJ becomes narrower and the wind-speed maximum descends at a lower height (Fig. 2.9). The larger wind-speed maximum is reached approximately 1 hr after the half inertial oscillation period. These features are also commonly observed in LLJs due to inertial oscillations

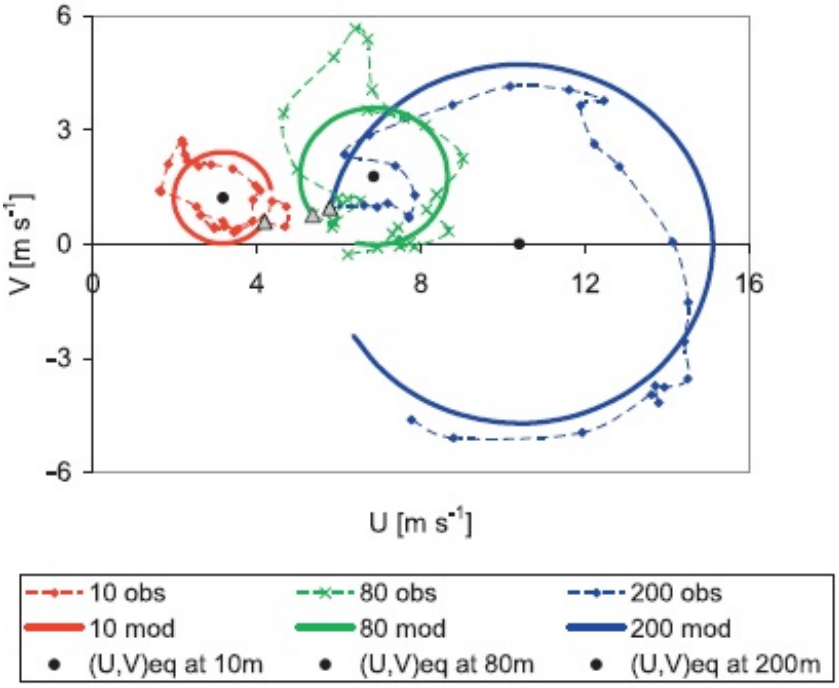

Figure 2.10: Hodographs for three different levels observed at the KNMI Cabauw Observatory (Netherlands) (dashed lines) on 15-16 July 2006 and simulated by the model of Van de Wiel et al. (2010) (solid lines) using an initial condition derived by observational data and the Ekman solutions as nocturnal equilibrium condition. The grey triangles indicate the initial velocity vectors (1630 UTC).

(Van Ulden and Wieringa, 1996). However, Chimonas (2005) proposed that the observed inertial period is shorter than the theoretical one because of the influence of secondary circulations as the exchange of air between the boundary layer and the free atmosphere. Then, Van de Wiel et al. (2010) improved their model considering a different initial profile derived by observational data measured at the KNMI Cabauw Observatory (Netherlands) because the wind is more uniform in amplitude and direction in the afternoon compared to as imposed using the Ekman solutions one. These solutions are still considered for the nocturnal equilibrium profile. This choice is in agreement with analytical studies based on the Ekman solutions that gives reasonable estimation of the nocturnal boundary layer height and of wind profiles (Zilitinkevich 1972; Nieuwstadt 1985). Van de Wiel et al.

(2010) adopted $\gamma^{-1} \approx 80$ m, $\bar{u}_g = -7 + \frac{6z}{2000}$ and $\bar{v}_g = 5 - \frac{5z}{2000}$ retrieved by wind-profiler data, where z is the vertical coordinate. Considering this new simulation, an initial decrease of the wind speed after the sunset is predicted near the surface (in the first few tens metres above the surface in which $\bar{u}_0 - \bar{u}_{eq} < 0$ and $\bar{v}_0 - \bar{v}_{eq} < 0$). This phenomenon is named backward inertial oscillations and it is an important mechanism to weaken the low-level winds right after the sunset. The changes of the wind vector can be well visualised on the hodograph, i.e. a diagram in the plane of the horizontal wind-speed components (u,v). Figure 2.10 shows the hodographs obtained by Van de Wiel et al. (2010) simulating the ones observed at the KNMI Cabauw Observatory (Netherlands) on 15-16 July 2006 with the improved initial condition. These hodographs are measured and simulated both for a low level (10 m) and for higher levels (80 m and 200 m). Van de Wiel et al. (2010) obtained circular hodographs that change gradually with height and rotate clockwise at each level (in North Hemisphere). However, the clockwise rotation implies a wind-speed decrease at the low level in the first half period, i.e. the backward inertial oscillations. Van de Wiel et al. (2010) suggested that these opposite tendencies in the wind speed between the low and the high levels tends to the occurrence of an inflection point in the wind-speed profile, implying a local maximum of the shear and supporting the generation of turbulence. Therefore, the backward inertial oscillations can contribute to the occurrence of intermittent turbulence, also modifying the hodographs. The simulation is in agreement with the observed hodographs, which are approximately circular. The larger discrepancies are observed at the sunset which is when the inertial oscillations start. These larger discrepancies can be due to the abrupt change of the eddy viscosity imposed at sunset. This change can be slightly more gradually. Other differences between the simulation and the observation could derived by the imposition of constant eddy viscosity with the height and the stationary of them and the geostrophic wind during the night. Van de Wiel et al. (2010) specified that many physical effects can dominate over inertial oscillations easily causing the deviation of the hodographs from their idealistic shape.

2.10 The Shapiro and Fedorovich's Model

Shapiro and Fedorovich (2009) extended the Blackadar's theory of inertial oscillations (Sect. 2.8) not considering a flat terrain but a gently planar slope. This model will be used in Chapter 6 to simulate the LLJs retrieved in the current thesis and understand if they follows the inertial-oscillations dynamics. Considering a gently planar slope, the effect of the buoyancy force on the motion in stable stratification is included. The buoyancy force is given by

$$b = g\frac{\theta - \theta_e}{\theta_r}, \tag{2.53}$$

in which θ_e is the environmental potential temperature and θ_r a constant reference one. Therefore, Shapiro and Fedorovich (2009) studied the case of inertial-gravity oscillations. The objective of this study was to investigate some features of LLJs not explainable by

Blackadar (1957) as why some LLJs doubled the geostrophic wind speed and the geographic preference of the LLJs to be formed on a particular area of the western sloping terrain part of the Great Plains compared to the eastern flat part. This latter phenomenon was investigated by other authors as Wexler (1961) and Holton (1967). Wexler (1961) connected this phenomenon to the large-scale dynamical processes describing the LLJs in the Great Plains as northward inertial flows associated with the blocking of the easterly trade winds by the Rocky Mountains, in analogy to the westward intensification of oceanic boundary current proposed by Stommel (1948). Instead, Holton (1967) proposed that a diurnal wind oscillation can be induced in a sloping boundary layer by the periodic radiative forcing. Despite these theories showed that the western sloping terrain in the Great Plains are favourite compared to the flat eastern one, neither of them can explain the pronounced westward decrease of the nocturnal LLJ frequency from 100° to 105° of latitude within the western sloping terrain (Bonner 1968; Mitchell et al. 1995; Walters et al. 2008).
Shapiro and Fedorovich (2009) proposed a 2D model in which the edge effects are neglected considering a planar slope of infinite extent and slope angle α. To reproduce the Great-Plains features, the planar slope is oriented from west to east and a constant pressure gradient on the synoptic scale towards west is considered. Considering this pressure gradient the geostrophic wind is chosen as $\bar{U}_g = (\bar{u}_g = 0, \bar{v}_g > 0)$ by Eqs. (2.23), (2.24). As the Blackadar's theory the viscous terms are assumed null immediately after the sunset. Therefore, the equations for the nocturnal conditions are:

$$\frac{\partial \bar{u}_n}{\partial t} = -b_n sin(\alpha) + f\bar{v}_n - f\bar{v}_g \tag{2.54}$$

$$\frac{\partial \bar{v}_n}{\partial t} = -f\bar{u}_n \tag{2.55}$$

$$\frac{\partial b_n}{\partial t} = \bar{u}_n N^2 sin(\alpha), \tag{2.56}$$

in which the Brunt-Väisälä frequency N is evaluated as

$$N = \sqrt{\frac{g}{\theta_r}\frac{\mathrm{d}\theta_e}{\mathrm{d}z}}. \tag{2.57}$$

In Eq. (2.56) the derivative of the buoyancy respect to time is equal to the along-slope advection of environmental potential temperature. As discussed by Holton (1967), this advection term generates positive/negative buoyancy in the presence of downslope/upslope flow, but this generation tends to oppose at this flow (Eq. (2.54)). Multiplying Eqs. (2.54), (2.55), (2.56) respectively by $\bar{u}_n$, $\bar{v}_n - \bar{v}_g$ and $\frac{b_n}{N^2}$, adding the resultant equations and integrating, the energy of the motion is obtained:

$$\bar{u}_n^2 + (\bar{v}_n - \bar{v}_g)^2 + \frac{b_n^2}{N^2} = const. \tag{2.58}$$

The energy of the motion is the sum of the kinetic energy due to the ageostrophic components and the potential energy associated with the buoyancy. Substituting Eq. (2.55)

into Eq. (2.56) and integrating, the following equation is obtained:

$$\bar{v}_n N^2 sin(\alpha) + b_n f = const. \tag{2.59}$$

Substituting b_n into Eq. (2.58) through the Eq. (2.59), Eq. (2.58) becomes:

$$\bar{u}_n^2 + \bar{v}_n^2 \left(1 + \frac{N^2}{f^2} sin^2(\alpha)\right) + m\bar{v}_n = n, \tag{2.60}$$

in which m and n are constants. Eq. (2.60) is the equation of an ellipse with major axis along u within the hodograph plane. Translating the ellipse in the hodograph plane to obtain one in the standard form $\frac{u^2}{a_e^2} + \frac{v^2}{b_e^2} = 1$, the ratio between the major axis $2a_e$ and the minor one $2b_e$ is equal to $\sqrt{1+Bu}$, in which $Bu = \frac{N^2}{f^2} sin^2(\alpha)$ is the Burger number. The eccentricity is obtained as

$$\epsilon = \sqrt{\frac{Bu}{1+Bu}}. \tag{2.61}$$

The eccentricity is independent on the geostrophic wind and the initial condition, but it is directly proportional to the slope angle and the stratification. This hodograph shape with major axis along u is in agreement with the observations over the Great Plains (Mitchell et al. 1995; Whiteman et al. 1997; Song et al. 2005).
Deriving with respect the time Eq. (2.54) and eliminating $\bar{v}_n$ and b_n respectively through Eqs. (2.55), (2.56), the following equation is obtained:

$$\frac{\partial^2 \bar{u}_n}{\partial t^2} = -\omega^2 \bar{u}_n, \tag{2.62}$$

where

$$\omega = f\sqrt{1+Bu} \tag{2.63}$$

is the inertial-gravity frequency. The larger Bu is the frequency will increase. The inertial-gravity period T is obtained as

$$T = 2\pi\omega^{-1}. \tag{2.64}$$

The general solution can be chosen as

$$\bar{u}_n = Acos(\omega t) + Bsin(\omega t). \tag{2.65}$$

Substituting Eq. (2.65) into Eq. (2.55) and integrating, the general solution for the other wind-speed component $\bar{v}_n$ is obtained:

$$\bar{v}_n = -\frac{f}{\omega}\left(Asin(\omega t) - Bcos(\omega t)\right) + C. \tag{2.66}$$

Substituting Eqs. (2.65), (2.66) into Eq. (2.54), the general solution for the nocturnal buoyancy b_n is found:

$$b_n = \frac{N^2 sin(\alpha)}{\omega}\left(Asin(\omega t) - Bcos(\omega t)\right) + \frac{f}{sin(\alpha)}\left(C - \bar{v}_g\right) \tag{2.67}$$

The initial conditions $b\,(0) = b_0$, $\bar{u}_n\,(0) = \bar{u}_0$ and $\bar{v}_n\,(0) = \bar{v}_0$ are imposed obtaining: $A = \bar{u}_0$, $B = \frac{1}{\omega}\left[-b_0 sin(\alpha) + f\,(\bar{v}_0 - \bar{v}_g)\right]$, $C = \frac{N^2}{\omega^2} sin^2\,[\alpha]\,\bar{v}_0 + \frac{f}{\omega^2}\,(b_0 \sin\,(\alpha) + f\bar{v}_g]$. Increasing the slope angle and the stratification, the component $\bar{v}_n$ decreases more than $\bar{u}_n$ and the amplitude of the hodograph is reduced. The solution proposed by Blackadar (1957), imposing the geostrophic wind component $\bar{U}_g = (\bar{u}_g = 0, \bar{v}_g)$, is a particular case with $Bu = 0$.
The solutions are non-dimensionalised by the following non-dimensional variables: $\bar{u}_n^* = \frac{\bar{u}_n}{\bar{v}_g}$, $\bar{v}_n^* = \frac{\bar{v}_n}{\bar{v}_g}$, $b_n^* = \frac{b_n sin\alpha}{f\bar{v}_g}$, $\Omega = \frac{\omega}{f} = \sqrt{1 + Bu}$, $\bar{u}_0^* = \frac{\bar{u}_0}{\bar{v}_g}$, $\bar{v}_0^* = \frac{\bar{v}_0}{\bar{v}_g}$, $b_0^* = \frac{b_0 sin\alpha}{f\bar{v}_g}$, $T = ft$.
Thus the solutions becomes:

$$\bar{u}_n^* - \bar{u}_0^* = \bar{u}_0^*\,(cos(\Omega T) - 1) + \frac{1}{\Omega}\,(-b_0^* + \bar{v}_0^* - 1)\,sin(\Omega T) \tag{2.68}$$

$$\bar{v}_n^* - \bar{v}_0^* = -\frac{\bar{u}_0^*}{\Omega} sin(\Omega T) + \frac{1}{\Omega^2}\,(-b_0^* + \bar{v}_0^* - 1)\,(cos(\Omega T) - 1) \tag{2.69}$$

$$b_n^* - b_0^* = \frac{\Omega^2 - 1}{\Omega}\bar{u}_0^* sin(\Omega T) - \frac{\Omega^2 - 1}{\Omega^2}\,(-b_0^* + \bar{v}_0^* - 1)\,(cos(\Omega T) - 1)\,. \tag{2.70}$$

Shapiro and Fedorovich (2009) also explored the dependence of the LLJ wind-speed maximum on the thermal structure of the boundary layer. Shapiro and Fedorovich (2009) considered the thermal structure of the residual layer to be unchanged from the well-mixed day state therefore the potential temperature is nearly constant with the height until a capping inversion layer at approximately $1 \div 2$ km above the surface that separates the residual layer from the free atmosphere. In the analysed case, the residual layer develops over a slightly-sloping terrain and Shapiro and Fedorovich (2009) defined a tilted residual layer (TRL) characterised by local neutral stratification and non-zero buoyancy. Fig. 2.11 shows the vertical cross-section through the TRL. The concept of the TRL is useful to understand the initial buoyancy of an air mass at any location J within it. The initial potential temperature θ_0 is assumed as constant in the residual layer until the base of the capping inversion layer. Then θ_0 increases by $\Delta\theta$ inside the inversion layer, so that the initial potential temperature at the top of the inversion (position K in Fig. 2.11) is $\theta_{0K} = \theta_0 + \Delta\theta$. Being the positions K and L at the same height and L in the free atmosphere, the initial potential temperature in L is also $\theta_{0L} = \theta_0 + \Delta\theta$. Moving an air mass from the point L to M (under L and at the same height of J but located in free atmosphere), the potential temperature decreases by an amount equal to the environmental potential temperature gradient times the altitude difference δ between L and M. Thus the potential temperature at M is $\theta_{0M} = \theta_0 + \Delta\theta - \delta\frac{\mathrm{d}\theta_e}{\mathrm{d}z}$. Considering $b_0 = g\frac{\theta_0 - \theta_e}{\theta_r}$ and the local neutral stratification in J, the initial buoyancy for the air mass located in J is $b_0 = -\frac{g\Delta\theta}{\theta_r} + N^2\delta$. The corresponding non-dimensional initial buoyancy is

$$b_0^* = \frac{N^2 sin\alpha}{f\bar{v}_g}\delta - \frac{sin\alpha}{f\bar{v}_g}\frac{g\Delta\theta}{\theta_r}. \tag{2.71}$$

Since δ increases downwards, the first term in Eq. (2.71) dominates if the air masses is lo-

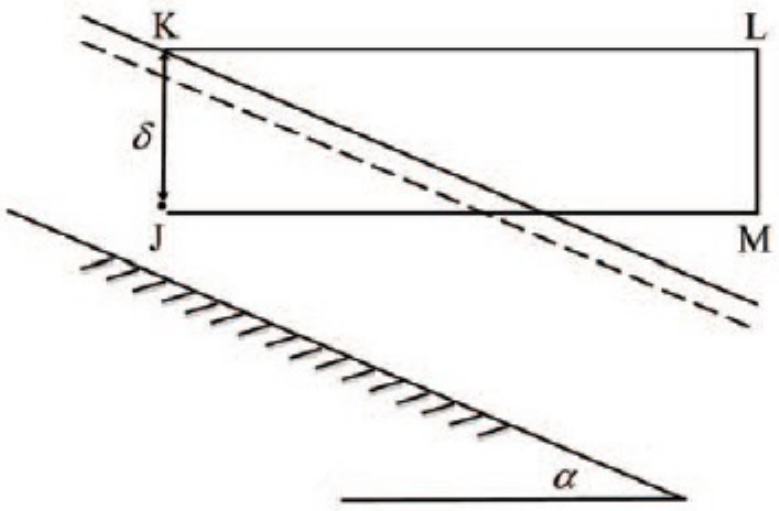

Figure 2.11: Vertical cross-section through a TRL over a gently slope terrain (Shapiro and Fedorovich, 2009).

cated at a sufficiently low level and if the initial buoyancy is positive, while the second term prevails at higher levels and the TRL is characterised by a downward-directed buoyancy gradient. Substituting Eq. (2.71) into Eqs. (2.68), (2.69) considering $\bar{U}_0^* = (\bar{u}_0^* = 0, \bar{v}_0^*)$ and half of the inertial-gravity oscillation period ($T = \frac{\pi}{\Omega}$) because the wind-speed maximum occurs after this time, the following equation for the wind-speed maximum is obtained:

$$\bar{v}_{max}^* = \bar{v}_0^* \left(1 - \frac{2f^2}{f^2 + N^2 sin^2(\alpha)}\right) + \frac{2f^2}{f^2 + N^2 sin^2(\alpha)} \left(\frac{N^2 sin(\alpha)}{f\bar{v}_g}\delta - \frac{sin(\alpha)}{f\bar{v}_g}\frac{g\Delta\theta}{\theta_r} + 1\right). \tag{2.72}$$

Shapiro and Fedorovich (2009) used typical values for the Great Plains to find the critical angle α^* which maximises the wind-speed maximum $\bar{v}_{max}^*$. These typical values are: 0.4 $\leq \bar{v}_0^* \leq 0.8$, $f = 8.3 \times 10^{-5}$ s^{-1}, 0.01 s^{-1} $\leq N \leq$ 0.015 s^{-1}, $\bar{v}_g = 15$ ms^{-1}, $\delta = 1000$ m, 0 K $\leq \Delta\theta \leq$ 4 K, $\theta_r = 300$ K. Assuming these values in Eq. (2.72) and increasing the slope angle α starting from the flat terrain condition (α=0°), the wind-speed maximum increases until a critical angle $\alpha^* \approx 0.15°$ is reached and then it decreases. This behaviour is accentuated increasing the stratification causing the wind-speed maximum to double or more the intensity of the geostrophic wind. Assuming the small-angle approximation $\sin(\alpha) \simeq \alpha$ and imposing $\frac{d\bar{v}_{max}^*}{d\alpha}|_{\alpha=\alpha^*} = 0$, an equation for the critical angle α^* is obtained:

$$\alpha^* = -\frac{f\bar{v}_g(1 - \bar{v}_0^*)}{N^2\delta - \frac{g\Delta\theta}{\theta_r}} + \sqrt{\left(\frac{f\bar{v}_g(1 - \bar{v}_0^*)}{N^2\delta - \frac{g\Delta\theta}{\theta_r}}\right)^2 + \frac{f^2}{N^2}}. \tag{2.73}$$

Maximising the wind-speed maximum, jet-like structures are more easily classified as LLJs by the identification criteria (Sect. 2.6). Therefore, the occurrence of LLJs where the Great Plains are characterised by the critical slope angle could be larger than the other parts. The critical angle is observed in the central Great Plains in the longitude range $(100 \div 102)^{\circ} W$, in which the climatological studies identify a maximum frequency of LLJ (Bonner 1968; Mitchell et al. 1995; Walters et al. 2008).

Summary

In conclusion, the dynamics within the stable boundary layer is characterised by the interaction between the intermittent turbulence and the sub-mesoscale motions, as the inertial-gravity waves. A phenomenon which is usually observed within the stable boundary layer is the LLJ, which is relevant because it could have impact on many human activities and implication on the human safety. The LLJ is a thin stream of air in fast motion, addressed as multiple LLJ when it is characterised by the simultaneous occurrence of more thin streams. As a consequence of the LLJ definition, the LLJ identification criteria proposed in literature are based on thresholds applied on the wind-speed maximum. If the wind-speed maximum is located at the same height of the stable boundary layer top, the occurrence of the LLJ prevents the generation of intermittent turbulence. This suppression does not occur when the maximum is located above the boundary layer top. In stable conditions, the LLJ formation is usually driven by inertial oscillations, which are undamped oscillations caused by the Coriolis force after the abrupt change of the frictional terms during the evening transitions. The theory of these oscillations has been firstly theorised as driving mechanism by Blackadar (1957) and improved by Van de Wiel et al. (2010) and Shapiro and Fedorovich (2009), which respectively proposed a flat-terrain model and a gently sloped-terrain one.

Chapter 3

Data Description

This chapter describes the field campaigns and the measurement site, along with the synoptic conditions suitable for analysing the local circulation, the equipment and the data processing used for this investigation. The measurement site for the current thesis is the Dugway Valley (Utah), a gently sloping terrain surrounded by mountains, within the MATERHORN Program. Only the data measured during quiescent intensive observing periods (IOPs) are analysed because the local scale dynamics is dominated by the thermal circulation in the valley. Section 3.1 reports the main information on the MATERHORN Program. Section 3.2 describes the measurement site and the phenomena that can occur in this site during the night and under quiescent conditions. Section 3.3 reports the synoptic conditions retrieved in the Western United States during the quiescent IOPs. Section 3.4 describes the equipment used in the Dugway Valley during the field campaigns. Section 3.5 reports all the preliminary operations to process the data which will be analysed in Chapters 4, 5, 6.

3.1 The MATERHORN Program

The Mountain Terrain Atmospheric Modeling and Observations (MATERHORN) Program was born in 2011 thanks to the U.S. Department of Defense (DoD). The principal participants were: University of Notre Dame (UND), University of California - Berkeley (UCB), Naval Postgraduate School (NPS), University of Utah (UU) and University of Virginia (UVA). The objective was to improve the weather prediction on mountainous terrain analysing the wide variability of the space and time scales in mountain weather that contributes to many phenomena hindering the predictability (Fernando et al., 2015). Understanding these phenomena is essential because about 70% of Earth's land surface is covered by complex terrain as slopes, valleys, canyons, escarpments, gullies and buttes. Most of the urban areas are also on complex terrain for the presence of water resources. Studying the mountain weather has practical applications in many field of study as urban air pollution and its dispersion (Ellis et al. 2000; Allwine et al. 2002; Fernando and Weil 2010), wind-energy production (Banta et al., 2013), aviation (Politovich et al., 2011),

alpine warfare (Winters et al., 2001) and firefighting (Albini et al., 1982). More specifically, the objectives of the MATERHORN Program were to improve:

- the predictability of the wind and temperature profiles near the surface;
- the surface-layer predictions improving the knowledge of soil moisture and soil properties;
- the mesoscale models;
- the short-range forecast through a better assimilation of the observations near the surface;
- the knowledge of phenomena from mesoscales to dissipation scales;
- the turbulence closure models and boundary-layer parametrisations;
- the simulations with ultra-high resolution (i.e. less than 50 m of horizontal resolution).

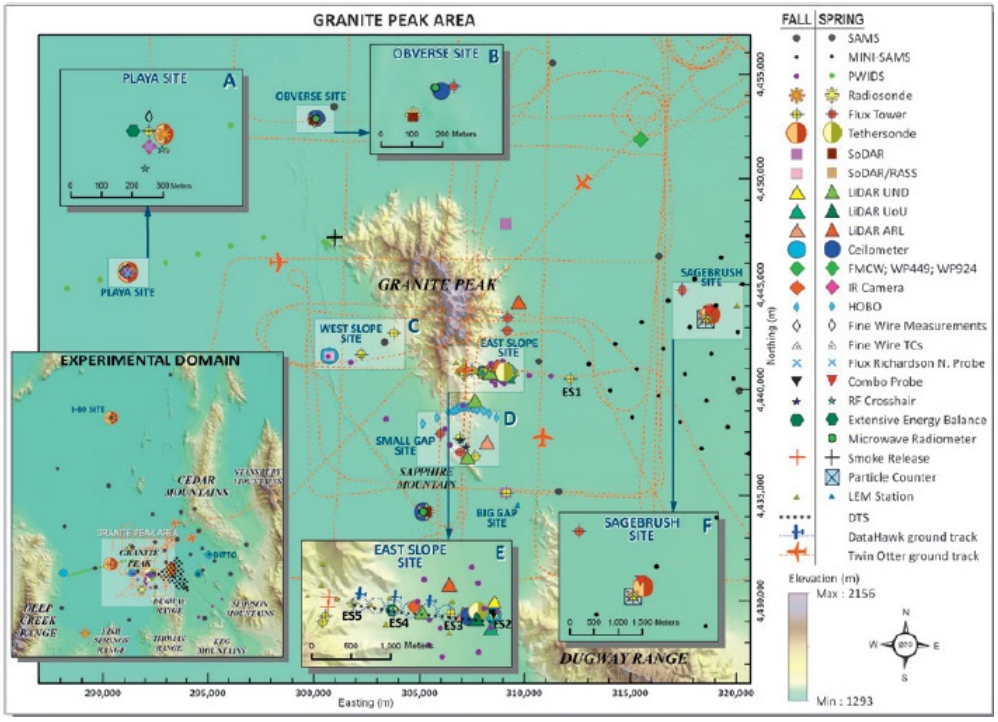

Figure 3.1: The Measurement site and the equipment of the MATERHORN Program during the two major field campaigns.

MATERHORN consists of four components working symbiotically to reach these objectives: the modelling component (MATERHORN-M), the experimental component

		Quiescent IOPs Operative period	Sunset	Sunrise
Fall 2012	IOP0	2000 UTC 25/09 – 2000 UTC 26/09	0117 UTC	1320 UTC
	IOP1	2000 UTC 28/09 – 2000 UTC 29/09	0112 UTC	1323 UTC
	IOP2	2000 UTC 01/10 – 2000 UTC 02/10	0107 UTC	1326 UTC
	IOP6	0800 UTC 14/10 – 0800 UTC 15/10	0048 UTC	1339 UTC
	IOP8	1100 UTC 18/10 – 1800 UTC 19/10	0040 UTC	1344 UTC
Spring 2013	IOP4	2000 UTC 11/05 – 2000 UTC 12/05	0233 UTC	1214 UTC
	IOP7	2315 UTC 20/05 – 2000 UTC 21/05	0241 UTC	1206 UTC

Table 3.1: The analysed quiescent IOPs and respective operative periods. The reported sunset and sunrise hours are referred to the night between the two days characterising each operative period, except for the IOP6 in which the reported ones are relative to the night between 13-14 October because of the different operative period.

(MATERHORN-X), the technology-development component (MATERHORN-T) and the parametrisation component (MATERHORN-P). Two major field campaigns were conducted in MATERHORN-X with high-resolution measurements focusing on arid/semiarid regions at spatial scales smaller than the mesoscale, in order to avoid the occurrence of orographic precipitations and marine pushes. The measurement site was the Granite Mountain Atmospheric Science Testbed (GMAST), which is a part of the United State Army Dugway Proving Ground (U.S. Army DPG) located 137 km southwest of Salt Lake City (Utah). Fig. 3.1 shows the measurement site and the equipment used (Fernando et al., 2015) during the two major field campaigns. The measurement site consisted of 3700 km^2 of land in complex terrain with playa and desert shrub as two dominant land-use types. An isolated topographic mountain named Granite Mountain (GM) is located within the site and it is characterised by a length of 11800 m, a width of 6100 m and a peak elevation of 840 m above the valley floor placed 1300 m a.s.l. The region is dry and characterised by an annual precipitation equal to 197 $mmyr^{-1}$ (Western Regional Climate Center, 2014). This site was chosen for numerous advantages: the large spatial extent, the richness in mountain weather phenomena, the interesting climatological regimes, the distinct land-use types, the already existing instrumentation network and the logistical support given by the U.S. Army DPG. The investigated days in this thesis are part of the campaigns performed during fall 2012 (25 September - 31 October 2012) and spring 2013 (1 May - 31 May 2013). The first was characterised by quiescent, dry, fair weather in which the thermal circulation dominated, while the second had more days subject to synoptic forcing. In fact, intermountain cyclones and cold fronts occur more frequently during the spring in which surface-pressure troughs can more easily extend northeastward from Sierra Nevada to the investigated region causing the formation of cyclogeneses and frontogeneses, resulting in abrupt changes in the weather conditions.

A cold front is an instability condition occurring when a cold air mass moves closer to another warmer one forcing this latter to moves upwards. Each campaign included 10 intensive observing periods (IOPs) in which all the instruments operated in coordination. The IOP days were chosen considering the forecast by MATERHORN meteorologists and the logistical and manpower constraints. They were classified depending on the 700 hPa wind speed U in: quiescent if $U < 5$ ms^{-1}, moderate if 5 ms^{-1} $< U <$ 10 ms^{-1} and transitional if the wind speed showed rapid temporal variation, with intensity even larger than 10 ms^{-1} during frontal passages. In the current thesis, only the quiescent IOPs are analysed. Table 3.1 summarises the analysed IOPs in terms of operative periods, sunset and sunrise hours. The reported time are expressed in UTC, which is 6 hours more than the local time MDT (MDT = UTC - 6 h).

3.2 The Measurement Site

The MATERHORN Program provided a large dataset used to investigate different phenomena on complex terrain as evening transition (Jensen et al., 2016), evaporation and fog dynamics (Hang et al. 2016; Zhang and Pu 2019), turbulence structures in katabatic flows (Grachev et al., 2016) and stable-stratified flow over topography (Leo et al., 2016).

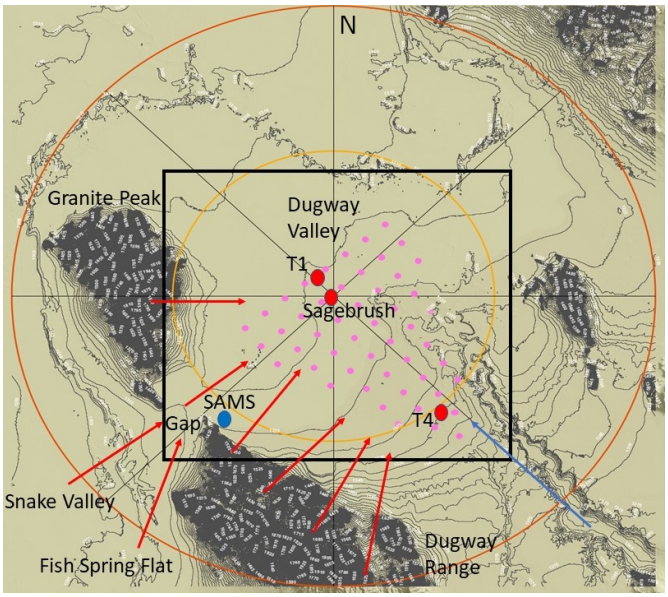

Figure 3.2: Measurement site of the current thesis. The black rectangle indicates the Dugway Valley, the red dots the flux towers, the pink dots the MINISAMS, the blue dot the SAMS close to the Gap, the blue arrow the downvalley-flow direction, the red arrows the secondary flows that can perturb the downvalley flow. The circumferences show the distances from Sagebrush (10 km yellow, 20 km orange) while the grey lines the cardinal points (N indicates the north).

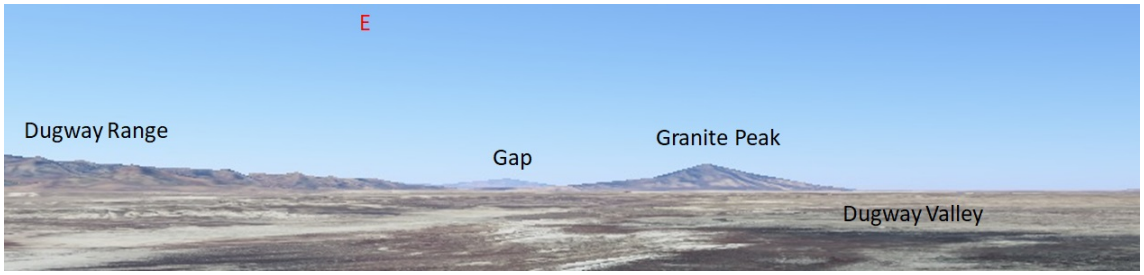

Figure 3.3: Measurement site of the current thesis observed from the southern side of the Dugway Valley. The letter E indicates the east direction.

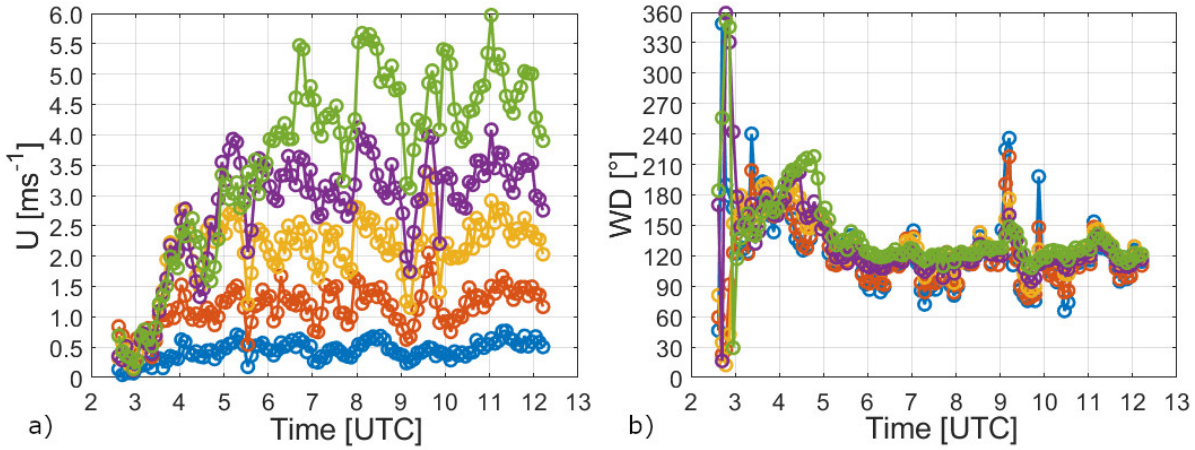

Figure 3.4: Time series averaged over 5 minutes of the wind speeds (a) and directions (b) measured by sonic anemometers in Sagebrush during a quiescent night. The dot-marked lines show measurements at elevation of 0.5 m (blue), 2 m (orange), 5 m (yellow), 10 m (purple) and 20 m (green). The sunset occurred at 0233 UTC and the sunrise at 1214 UTC, marking respectively the beginning and the end of the time series.

Measurements for the current analysis were collected from the Dugway Valley (40.121360, -113.129070), Utah (black rectangle, Fig. 3.2), a gently sloping terrain at 1300 m a.s.l, oriented from south-east to north-west, located on the eastern side of the Granite Peak and characterised by arid soil and desert shrub vegetation. Fig. 3.3 shows the measurement site observed from the southern side of the Dugway Valley. The Dugway Valley is southerly bounded by the Dugway Range, a mountain chain separated from the Granite Peak by a Gap, where channelling flows can cause intrusions of air masses from and to the Snake Valley and the Fish Springs Flat on the western side of the Granite Peak and the Dugway Range (Fig. 3.2). In the current thesis, the dynamics of LLJs and Multiple LLJs that occurs during the night in quiescent IOPs is analysed. Many mountain-valley flow processes can characterise these nights. Being dominates by the thermal circulation, the downvalley flow is the main circulation (blue arrows, Fig. 3.2) within the Dugway Valley. The Downvalley flow is not usually pure because it interacts with secondary downslope

flows (named also katabatic flows) as the ones from the Dugway Range and the Granite Peak (red arrows, Fig. 3.2) or with smaller topographic features generating intermittent turbulence. Furthermore, the downvalley flow can duct through gaps and canyons (Mayr et al., 2007) and split from the slopes as intrusions (Lu and Turco, 1994). The colder air that drains down from the slopes during the night can accumulate in the valley forming a stable cold pool characterised by intermittent turbulence. This turbulence is due to the downslope flows that can have pulsations at critical internal-wave frequency (Princevac and Fernando, 2008) causing the alternation of intrusions from different slopes (Fernando et al., 2013). Other intrusions that can contribute at the weakly turbulent conditions are channelling currents (red arrows, Fig. 3.2) from the gaps, as the one with separated the Dugway Range from the Granite Peak. As example, Fig. 3.4 shows the time series of wind speeds and directions measured at five different heights within the centre of the Dugway Valley (Sagebrush site) during a quiescent night. Starting at 0500 UTC, the wind constantly flows from south-east, i.e. the downvalley direction according to the Dugway Valley orientation. However, temporary disturbances can cause tilts of the wind direction (Fig. 3.4b) and damps of wind speed (Fig. 3.4a) as observed at 0911 UTC and 0953 UTC.

3.3 Synoptic conditions

This thesis is focused on the IOPs classified as quiescent because the thermal circulations dominate during the weak synoptic forcings. They are characterised by the presence of high pressure and the absence of front passages or large pressure gradients as synoptic conditions. Since the measurement site is located in Utah, the following analysis considered only the Western United States. Fig. 3.5 shows the synoptic conditions at 0000 UTC during the spring quiescent IOPs, while Fig. 3.6 shows the ones during the fall quiescent IOPs. Despite the synoptic systems can intensify or weaken during the night, the maps at

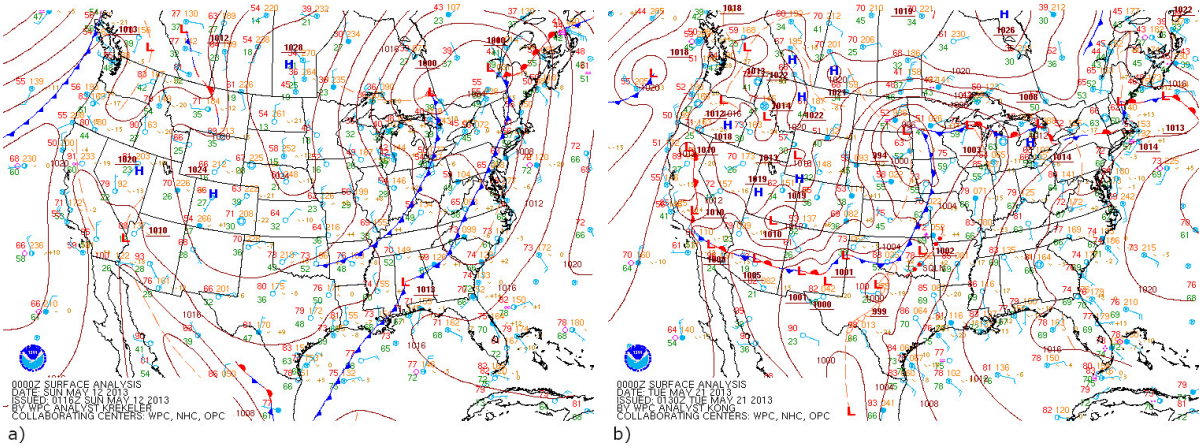

Figure 3.5: Synoptic conditions at 0000 UTC in United States during the quiescent spring-IOPs: (a) IOP4, (b) IOP7. This surface analyses were produced by the National Oceanic and Atmospheric Administration (NOAA).

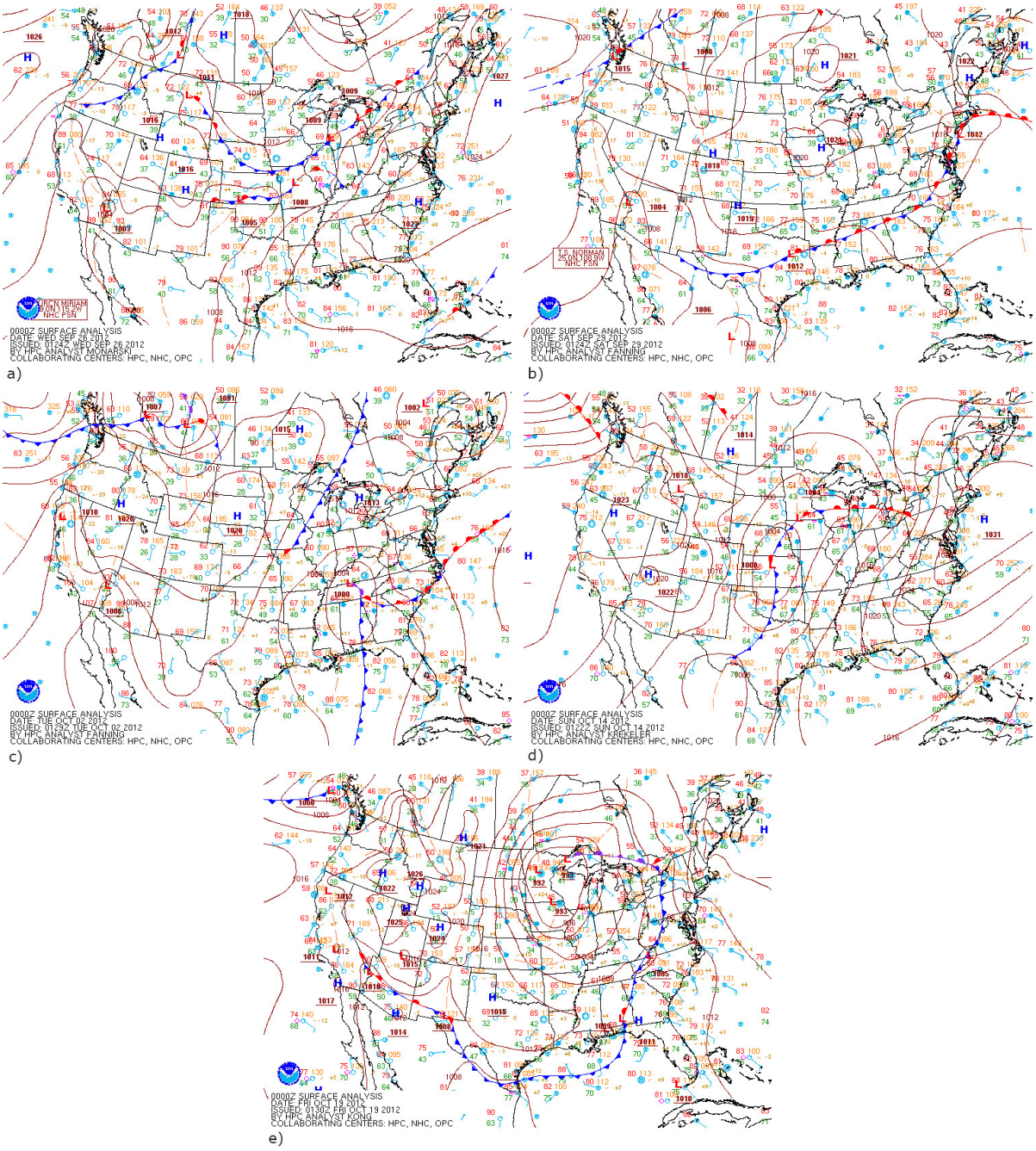

Figure 3.6: Synoptic conditions at 0000 UTC in United States during the quiescent fall-IOPs: (a) IOP0, (b) IOP1, (c) IOP2, (d) IOP6, (e) IOP8. This surface analyses were produced by the National Oceanic and Atmospheric Administration (NOAA).

0000 UTC were chosen because the high-pressure conditions tend to last for several days, which is a long-lasted period compered than the single analysed nights. The spring-IOPs are 2, i.e. the IOP4 and IOP7. The IOP4 is characterised by high pressure (up to 1020

hPa) in all the Western United States except for the southern side (down to 1010 hPa) (Fig. 3.5a). The IOP7 is the most perturbed IOP at the synoptic scale, in which low pressure (down to 1000 hPa) occurs in all the analysed region except in the central part (high pressure up to 1019 hPa) (Fig. 3.5b). A stationary front is located in the southern part. The fall-IOPs are 5, i.e. the IOP0, IOP1, IOP2, IOP6, IOP8. The IOP0 is characterised by high pressure (up to 1016 hPa) except in the southern part of the Western United States (low pressure down to 1003 hPa) (Fig. 3.6a) and in the northern part of the West Coast (down to 1008 hPa) in which a cold front is located. During the IOP1 the high pressure (up to 1018 hPa) is placed in all the investigated area except for the southern side (down to 1004 hPa) (Fig. 3.6b). A cold front occurs in the northern part of the West Coast. The synoptic conditions during the IOP2 are not so different from the IOP1 ones. The IOP2 is characterised by high pressure (up to 1020 hPa) except for the southern part of the analysed area (low pressure down to 1006 hPa) (Fig. 3.6c). The IOP6 is the investigated IOP with the most calm synoptic conditions, with high pressure (up to 1023 hPa) characterising all the Western United States (Fig. 3.6d). The IOP8 is generally characterised by calm conditions too, with high pressure (up to 1026 hPa) in all the considered region except for the southern side (low pressure down to 1010 hPa) in which a stationary front occurs (Fig. 3.6e). In conclusion, during quiescent IOPs, the Western United States are generally characterised by high pressure in the central part and low pressure in the southern one, in which a stationary front is sometimes located. The northern part is sometimes characterised by a cold front coming from north.

3.4 The Equipment

Measurements were retrieved from 3 flux towers, located respectively at Sagebrush, T1 and T4 (Fig. 3.2). Taking the Sagebrush flux tower as reference, T4 and T1 were located 1.8 km to the north-west and 10.3 km to the south-east respectively. Table 3.2 shows the coordinates and the elevation of the 3 towers, located on a gentle slope characterised by slopes angles between coupled towers $\alpha_{T4-Sagebrush} = 0.023°$ and $\alpha_{Sagebrush-T1} = 0.064°$. Despite the whole investigation will cover both fall and spring IOPs, measurements from the T1 and T4 flux towers are available only for the spring campaign. The flux tower at Sagebrush was 20 m tall and equipped with sonic anemometers (CSAT3, Campbell Scientific, Logan, U.S.) coupled with temperature and relative-humidity probes (HMP45C-L, Campbell Scientific, Logan, U.S.) and barometers (CS106, Campbell Scientific, Logan, U.S.) displaced at 5 levels (0.5 m, 2 m, 5 m, 10 m and 20 m). T1 and T4 are similarly equipped with sonic anemometers (81000, Young Company, Traverse City, U.S.) coupled with temperature and relative-humidity probes (HMP45C-L, Campbell Scientific, Logan, U.S.) and barometers (CS106, Campbell Scientific, Logan, U.S.) mounted on 5 levels (2 m, 4 m, 8 m, 16 m and 28 m) of 28-m towers. The temperature and relative-humidity probes sampled at 1 Hz, while the sonic anemometers sampled at 20 Hz. At Sagebrush, upper-air (radiosonde) soundings (DFM-09, Graw Radiosondes, Nuremberg, Germany) and tethered-balloon soundings (TTS111, Vaisala, Laskutus, Finland) were also opera-

	Flux Towers		
	Latitude [°]	Longitude [°]	Elevation [m]
Sagebrush	40.12136	-113.12907	1316.35
T1	40.13338	-113.14263	1315.63
T4	40.05107	-113.05085	1328.92

Table 3.2: Flux towers' location.

tive during the IOPs. Furthermore, a Surface Atmospheric Measurement Stations Mini Network (MINISAMS) was arranged in the Dugway Valley to enable the horizontal extrapolation of temperature and wind-speed fields. This network contains 51 10-m towers equipped with vane anemometers (05103, Young Company, Traverse City, U.S.) and temperature and relative-humidity probes (HMP45C-L, Campbell Scientific, Logan, U.S.) at 2 vertical levels (2 m and 10 m). Data from MINISAMS were stored at 1-minute average. A station of the 31 ones constituted the Surface Atmospheric Measurement Stations Network (SAMS) is located close to the Gap to monitor possible circulation between the Dugway Valley, the Snake Valley and the Fish Springs Flat through the Gap. This SAMS measured the wind speed and direction, temperature and relative humidity at 2-m height using the same instrumentation of the MINISAMS and stored the 5-minutes average. The instrumental specifications are reported in Appendix C.

3.5 The Data Processing

The analysed data were collected during the two major field campaigns in the Dugway Valley. These data were retrieved by: tethered balloon (Fernando, 2017), radiosondes (De Wekker, 2017), flux towers (Pace, 2017), MINISAMS (Pace, 2016a) and SAMS (Pace, 2016b). They are analysed using Matlab programs after some preliminary operation. The programs allow to compute of the main quantities as the wind speed and direction, potential temperature, kinematic heat and momentum fluxes, turbulence kinetic energy (TKE), Brunt-Väisälä frequency and Richardson numbers.

3.5.1 Checking and Despiking Procedure

The tethered-balloon soundings and the flux-towers dataset are preliminary checked to detect and remove non-physical data or instrumental fails. The flux-towers data are also despiked. The despiking procedure is useful to filter unwanted spikes, i.e. a single or a very small group of data characterised by a magnitude too different compared to the data distribution. The despiking ensures that the averaging procedure will not be affected by these spikes. The presence of spikes in the measured variables can also increase the error of the derived quantities. The despiking procedure is similar to the method proposed by

Hejstrup (1993), applied once every 5-minutes data interval (Vickers and Mahrt, 1997). This method assumes that each interval within the dataset follows a Gaussian distribution of independent data characterised by mean ($\bar{x}$) and standard deviation (σ). Values above a certain threshold $C\sigma$, where $C = 3.5$ is a discriminant factor in agreement with Vickers and Mahrt (1997) and Schmid et al. (2000), are marked as spikes and replaced by the mean value of the interval calculated not considering the spikes. 5-minutes intervals are chosen because they ensure to gather most of the variance without loosing the Gaussian assumption.

3.5.2 The Rotation

The despiked wind-speed components averaged over 5 minutes, $\bar{U}_1 = (\bar{u}_1, \bar{v}_1, \bar{w}_1)$, are rotated to align the wind vector to the mean streamline direction (McMillen, 1988). The 5-minutes average is used for rotation as it will be the averaging interval for the measured variables (Sect. 3.5.4). Choosing a spherical system, the horizontal wind speed $\bar{s}$ (ms^{-1}), the azimuthal angle θ and the elevation angle ϕ are obtained as follows: $\bar{s} = \sqrt{\bar{u}^2 + \bar{v}^2}$, $\theta = \arctan\left(\frac{\bar{v}}{\bar{u}}\right)$, $\phi = \arctan\left(\frac{\bar{w}}{\bar{s}}\right)$. The rotation in the new wind vector $\bar{U}_2 = \left(\bar{u}_2 \approx \bar{U}_1, \bar{v}_2 \approx 0, \bar{w}_2 \approx 0\right)$ is given by

$$\bar{U}_2 = R_{m,n} \times \bar{U}_1, \tag{3.1}$$

in which

$$R_{m,n} = \begin{bmatrix} \cos(\phi)\cos(\theta) & \cos(\phi)\sin(\theta) & \sin(\phi) \\ -\sin(\theta) & \cos(\theta) & 0 \\ -\sin(\phi)\cos(\theta) & -\sin(\phi)\sin(\theta) & \cos(\phi) \end{bmatrix}$$

is the rotation matrix.

3.5.3 The Turbulent-Components Computation

For each measured variable or derived quantity a, the turbulent component a' can be obtained as

$$a' = a - \bar{a}, \tag{3.2}$$

in which $\bar{a}$ is the averaged part. This is the application of the Reynolds hypothesis, which stands that every data within a time interval can be decomposed in an averaged part and a turbulent one characterised by null average, if the statistic properties of the flow are preserved during the considered time interval. This hypothesis is usually verified with time interval less than 1 hr, which is named characteristic time of turbulence.

3.5.4 Averaging

The wind-speed profiles retrieved by tethered-balloon soundings are not averaged, except for the data collected at the same height. This choice derives by a preliminary visual inspection of the dataset in which many LLJs are too narrow to be captured if the data

are averaged. The wind rose is subdivided in 16 22.5° wide intervals, each associated with a different wind direction. Since the punctual knowledge of the wind-direction profile is not required in the analysis of the LLJs and Multiple LLJs because only the wind direction that characterises each layer within a nose is evaluated, the same precision considered in the wind-speed profiles is not necessary for the wind-direction ones and the 5-m mode is chosen for them.
The sampling rate of the sonic anemometers allowed to collect data at 20 Hz. This feature is fundamental to observe the turbulent patterns. However, the time series at 20 Hz are affected by the signal noise, which is filtered averaging the flux-towers data over 5 minutes intervals. This choice enable to obtain a robust result without loosing the information concerning the turbulence brought by the fluctuations. The data are occasionally averaged on smaller intervals, as 10 seconds, when the analysis needs to observe specific phenomena at a finer time resolution. These choices are in agreement with other studies focused on turbulent phenomena (for example Hunt (1985)).
MINISAMS data are also averaged on 5-minutes intervals to match the time step of the flux-towers ones.

3.5.5 The Comparison between flux-tower and tethered-balloon data

As described in Sect. 3.4, Sagebrush is equipped both by a flux tower and a tethered balloon allowing to compare the data retrieved by the two different instrumentation.

		Starting height in tethered-balloon profiles	
		Minimum height [m]	Maximum height [m]
2012 Fall	IOP0	-4	0
	IOP1	-4	3
	IOP2	-3	-2
	IOP6	-11	-4
	IOP8	-4	6
2013 Spring	IOP4	-11	-5
	IOP7	-7	2

Table 3.3: Minima and maxima starting heights for the nocturnal profiles measured by tethered balloon in Sagebrush.

These instrumentation can be used to check the accuracy of the tethered balloon in the first metres above the surface where the data can be affected by a larger measurement error due to the presence of the terrain. Furthermore, the sonic anemometers equipped on the flux tower are characterised by a better resolution and accuracy compared to the tethered balloon, therefore the anemometers data are a good reference to perform this

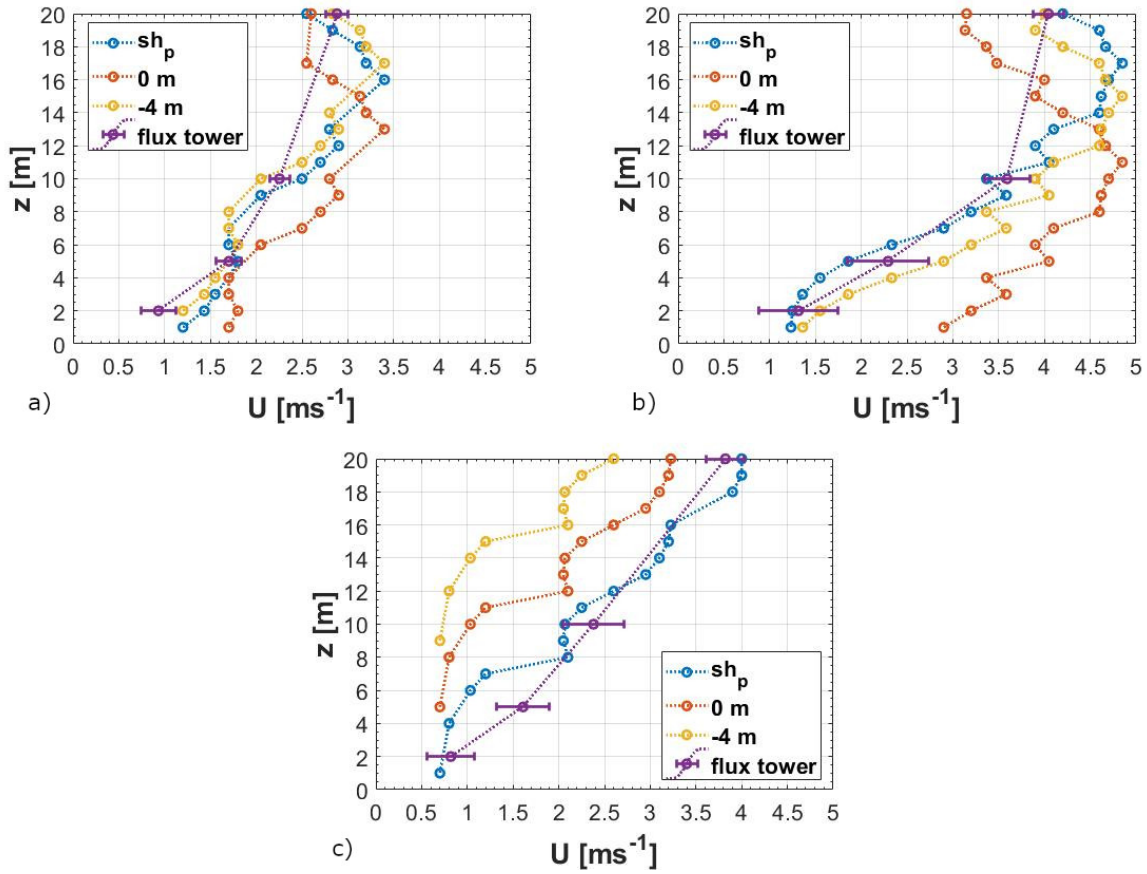

Figure 3.7: Examples of comparison between flux-tower and tethered-balloon data at 0734 UTC during the IOP0 (a), at 0625 UTC during the IOP4 (b), at 1012 UTC during the IOP8 (c). Three different offsets are applied to each profile: $o = 0$ m (orange line), $o = sh_p$ (blue line) and $o = -4$ m (yellow line). These profiles are compared to the flux-tower ones (purple line). The horizontal error bars in the flux-tower profiles are equal to the standard deviations.

check (Appendix C). This procedure allows to reveal the presence of possible vertical offsets in the tethered-balloon measurements. Table 3.3 shows the minima and maxima starting heights reported in the nocturnal profiles measured by the tethered balloon. For some measurement problems, the IOP2 have only of two available nocturnal profiles. As reported in Table 3.3, the tethered-balloon datasets report unusual measurements in many nocturnal profiles because some data are collected at negative heights, i.e. they should be measured underground. Therefore, these data could be a symptom of a vertical offset in the tethered-balloon soundings. Three offsets o were defined and compared. The first offset $o = sh_p$ (m) is variable for each profile because it is assumed equal to the the starting height that characterises each profile (blue line, Fig. 3.7). Using this offset, each profile starts from the height $z = 1$ m, i.e. there are not measurements collected at

the ground or underground. The second offset is the null one $o = 0$ m (orange line, Fig. 3.7) and the third offset is o = -4 m (yellow line, Fig. 3.7) which is the most common minimum starting height reported in Table 3.3. The comparison is made considering all the nocturnal wind-speed profiles during the IOP0 (Fig. 3.7a), IOP8 (Fig. 3.7b) and IOP4 (Fig. 3.7c). They were chosen because they are characterised by different starting heights (Table 3.3). They are compared with the 5-minutes averaged wind-speed profiles built averaging evaluated from the flux-tower. The horizontal error bars within the flux-tower profiles reports the standard deviation calculated considering all the wind speed averaged in each 5-minutes interval (Fig. 3.7). The comparison was evaluated by visual inspection. During the IOP0, the better comparison is obtained using the offset o = -4 m, however the difference with $o = sh_p$ is very small because -4 m $< sh_p <$ -2 m except for one profile in which $sh_p = 0$ m. During the IOP8, the offset o = -4 m and $o = sh_p$ gives different results because sh_p is usually above -1 m. The better comparison is obtained through $o = sh_p$, while o = -4 m gives accentuated differences in some profiles. During the IOP4, sh_p is usually in the range -8 m $< sh_p <$ -6 m, therefore it is slightly less than the other offset o = -4 m. In this case, the result is not so clear because the two offsets are respectively better in half of the profiles. However, the offset o = -4 m is worse than $o = 0$ m in few profiles. Considering all the analysed quiescent IOPs, the null offset $o = 0$ m is the worst in each one, while o = -4 m and $o = sh_p$ gives good and quite consistent results. The offset $o = sh_p$ was chosen in the current thesis because it gives slightly better results and avoids to have negative heights in the tethered-balloon profile.

Summary

In conclusion, the data used in this thesis were collected within the Dugway Valley (Utah) during the MATERHORN Program, which is focused on the improving of the weather prediction on mountainous terrain. This site is characterised by complex terrain with playa and desert shrub as two dominant land-use types. The analysed data were measured during quiescent IOPs, in which the high pressure characterised the central part of the Western United States, while the low pressures were located in the southern one, when present. In this latter part a stationary front sometimes occurs, while the northern one is sometimes characterised by a cold front. The synoptic forcings are weak in these conditions, therefore the circulation within the valley was thermal. The analyses in the current thesis were conducted through the data retrieved by 3 flux towers, a tethered balloon, a radiosonde and two networks of surface atmospheric measurement stations (MINISAMS and SAMS). Some preliminary operation were conducted to remove non-physical measurements or instrumental fails. The sonic-anemometers data were also despiked to remove outliers that could have affected the derived and averaged quantities. Then, the despiked wind-speed components averaged over 5-minutes intervals are rotated. The aim of the rotation is to align the wind vector to the mean streamline direction. Successively, the turbulent components were obtained assuming the Reynolds hypothesis (Eq. (3.2)). The wind-speed profiles collected by tethered balloon were not averaged except for the

data collected at the same height, because many LLJs retrieved in the analysed data was too narrow to be captured if the data would have been averaged. The 5-m mode was considered for the wind-direction profiles because the punctual knowledge of this profile is not required and only the wind direction that characterises each layer within a nose was evaluated in the analysis of the LLJs and Multiple LLJs. To filter the signal noise without loosing the information concerning the turbulence, the flux-towers data was averaged over 5 minutes. However, the data was occasionally averaged on smaller intervals to understand specific phenomena characterised by smaller time steps. MINISAMS data were also averaged on 5-minutes intervals in agreement with the flux-towers ones. An offset was applied to the vertical position reported in tethered-balloon soundings after a comparison between the wind speed retrieved by tethered balloon and the flux tower in Sagebrush. This offset is variable for each sounding and it is equal to the starting height detected in each of them.

Chapter 4

Low-Level Jets Identification and Classification

The objectives of this chapter are to define new criteria to identify LLJs and Multiple LLJs retrieved in the analysed data and to understand the mechanisms that drive the formation of the detected double-nose LLJs. Section 4.1 reports the newly-proposed identification criteria based on the detection of the wind-speed minima and maxima along the analysed profiles and formulated considering the ones already existing in literature. Section 4.2 describes the nocturnal evolution of the main variables (wind speed and direction, potential temperature and relative humidity) during some quiescent IOPs (IOP4 and IOP8). Section 4.3 reports the newly-proposed driving mechanism for the double-nose LLJ formation. Section 4.4 reports the identified double-nose LLJs in each quiescent IOPs using the identification criteria proposed in Sect. 4.1 and their classification based on the driving mechanisms proposed in Sect. 4.3.

4.1 Criteria for Low-Level Jet and multiple Low-Level Jet identification

As reported in Sect. 2.6, several criteria have been proposed in literature to identify LLJs and multiple LLJs. Similarly to the current thesis, the criteria suggested in the last two decades (Andreas et al. 2000; Banta et al. 2002; Baas et al. 2009) have been derived from observations of LLJs driven by inertial oscillations, located in the first 500 m of the wind-speed profile. Measurements for these analyses were retrieved using "grounded" instrumentation mounted on ground stations, towers and tethered balloons. The LLJs currently analysed were observed by tethered-balloon soundings and they are characterised by some similar features compered to the previous studies as the same wind-speed maximum range during the spring quiescent IOPs (between 6 ms^{-1} and 10 ms^{-1}). Conversely this range is less during the fall ones (3 ms^{-1} and 6 ms^{-1}) because the growth of the LLJ is more perturbed by intrusions. Another difference is the retrieved LLJ wind-speed maximum is located at a lower height compered to the previous studies

(Sect. 2.6) because it is retrieved between 10 m and 75 m above the surface. Analogies and differences are retrieved also for the double-nose LLJs. The first double-nose LLJ maximum is usually located in the same range, while the second one is located higher and derives by a perturbation of the already established LLJ.
Starting from the criteria proposed in the recent past, an objective of this thesis is to define a new criterion to identify the LLJs and multiple LLJs observed within the investigated nocturnal flow and also applicable in other contexts. For the sake of simplicity, the noses of a multiple LLJ are referred to as primary if corresponding to the long-lasting nose due to inertial oscillations close to the terrain, and as secondary if temporarily caused by a modification of the LLJ structure. The newly-proposed LLJ identification criterion combines the absolute threshold of Banta et al. (2002) to assess small wind speeds as the large instrumental resolution allows to minimise the errors and to refine the threshold value, with a newly-introduced relative threshold to account for large wind speeds, as done by Baas et al. (2009). The criterion proposed by Banta et al. (2002) and applicable at all the LLJs is

$$U_{max} \geq 1.5\, ms^{-1} + U^{a,b}_{min}, \tag{4.1}$$

in which U_{max} indicates the wind-speed maximum, U_{min} the wind-speed minimum below (superscript b) and above (superscript a) it. The threshold of 1.5 ms^{-1} can be reduced according to the instrumental precision. The considered criterion proposed by Baas et al. (2009) for the LLJs in which $U_{max} \geq 10$ ms^{-1} is

$$U_{max} \geq 1.25 U^{a,b}_{min}. \tag{4.2}$$

The newly-proposed LLJ identification criterion reads is:

$$U_{max} \geq \begin{cases} 1.5\, ms^{-1} + U^{a,b}_{min} & \text{for } U_{max} < 7.5 \text{ ms}^{-1} \\ 1.25 U^{a,b}_{min} & \text{for } U_{max} \geq 7.5 \text{ ms}^{-1}. \end{cases} \tag{4.3}$$

Since the measurements near the terrain can be affected by a larger measurement error due to the interference of the terrain, if a wind-speed maximum is found below the height of 20 m the new LLJ identification criterion (Eq. (4.3)) is evaluated using the wind speed measured at 20 m. Eq. (4.3) can also be used to identify multiple LLJs, as done by several authors with previous LLJ identification criteria (underlined in blue, Table 2.1). Equally important to characterise the multiple LLJs is the identification of the wind-speed minima to better detail the complex shape of the profile and delimit each nose vertical extension. The criterion to identify the wind-speed minima are not often well defined in literature. The most complete criterion is suggested by Baas et al. (2009), which proposed that a wind speed is a minimum if the wind speed increases of 1 ms^{-1} or more both above and below its height. This criterion is maintained to identify the largest minima ($U_{min} > 4$ ms^{-1}) in the current thesis. However, it is considered too restrictive for the smallest minima ($U_{min} < 2$ ms^{-1}) since it requires the wind speed to increase at least of the 50% of their values both above and below them. A new absolute threshold

is proposed for the smallest minima and it is linked to the Baas et al. (2009) one used for the largest minima, by an extrapolated linear trend in the range 2 $\text{ms}^{-1} < U_{min} <$ 4 ms^{-1}. This difference in the wind-speed minima evaluation depends on the vertical resolution, and this dependency is stronger in the current thesis than what was for Baas et al. (2009) because it used measurements detected at elevation of 10 m, 20 m, 40 m, 80 m and approximately every 60 m above, while the vertical resolution is 1 m in the current thesis. The newly-proposed criterion to identify the wind-speed minima is defined as follows:

$$U_{min} \geq \begin{cases} U^{a,b} - 0.5\, ms^{-1} & \text{for } U_{min} < 2 \text{ ms}^{-1} \\ 0.8U^{a,b} & \text{for } 2 \text{ ms}^{-1} \leq U_{min} \leq 4 \text{ ms}^{-1} \\ U^{a,b} - 1.0\, ms^{-1} & \text{for } U_{min} > 4 \text{ ms}^{-1} \end{cases} \tag{4.4}$$

where U indicates the wind speed below (superscript b) and above (superscript a) the investigated minimum. If Eq. (4.4) fails to determine a wind-speed minimum for a multiple LLJ profile characterised by a number N of noses, this minimum is assigned as:

$$U_{min} = \begin{cases} 0 & \text{for } U_{min}^{1b} \\ c_{min}^{i} & \text{for } U_{min}^{1a,\ldots,Nb} \\ c_{min}^{a} & \text{for } U_{min}^{Na} \end{cases} \tag{4.5}$$

in which c_{min}^{i} is the smallest wind speed measured between the noses and c_{min}^{a} the smallest wind speed above the higher nose. The superscripts $1b$ and $1a$ indicate respectively the minimum below and above the primary nose, while Nb and Na indicate the ones below and above the secondary noses. However, when the wind-speed vertical variation ΔU is less than 0.5 ms^{-1} for an atmospheric layer Δz larger than 100 m above or below a wind-speed maximum, the wind-speed minimum is forced to be inside that layer (blue profile, Fig. 4.1). This choice allows to discharge the atmospheric depths characterised by constant wind speed. Being the wind-speed profiles not averaged, the 12.5% of the wind-speed minima identified were discarded and subjectively reevaluated considering the absolute minima to avoid local disturbances or measurement errors (orange profile, Fig. 4.1). The orange profile in Fig. 4.1 is classified as a double-nose LLJs, while the blue profile is classified as a LLJ because only the primary nose verifies the LLJ identification criterion (Eq. (4.3)).

A new variable, named nose width n_w, is defined to better characterise the double-nose LLJ shape. The nose width is computed for each nose considering two half-normal distributions both peaked on the wind-speed maximum. The standard deviations associated with each half-normal distributions are calculated considering all the measurements between the maximum and the minimum below for the lower half-normal distribution, and

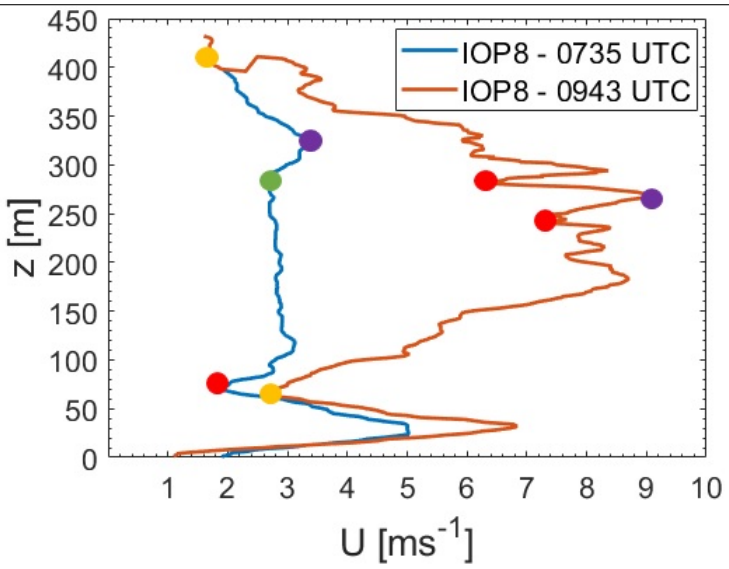

Figure 4.1: Example of wind-speed minima discharged and reevaluated. The purple dots indicates the considered wind-speed maximum, the red dots the discharged minima, the green dot the considered minima after the reevaluation in the blue profile, the yellow dots the considered minima after the reevaluation in the orange profile.

between the maximum and the minimum above for the upper one. The standard deviation of the lower half-normal distribution allows to determine a lower height h_l, defined as the height where the wind speed is equal to the difference between the wind-speed maximum and the lower standard deviation. Similarly, an upper height h_u can be identified considering the standard deviation of the upper half-normal distribution. The nose width n_w is given by:

$$n_w = h_u - h_l. \tag{4.6}$$

To evaluate the symmetry of the noses, the symmetry ratio ν is defined. The symmetry ratio is computed for each noses as follow:

$$\nu = \frac{h_l + h_u}{2h_{max}}, \tag{4.7}$$

where h_{max} is the height of the wind-speed maximum. This ratio is equal to 1 if the nose is symmetrical. In this case the maximum is located in the centre of the layer that includes the nose. The noses are evaluated as symmetrical if the symmetry ratio is included in the range (1.0 ± 0.1). Finally, the noses of each multiple LLJ profile are associated with different air masses if the modes of the wind directions inside each layer containing a nose differ more than the threshold of 22.5°.

4.2 Quiescent IOPs Observations

The general features observed during the night of the spring and fall quiescent IOPs are described in this section. This analysis is based on the tethered-balloon soundings data. Fig. 4.2a,b show respectively the evolution of the wind-speed and wind-direction profiles during the IOP4, as example of the one observed during the spring quiescent IOPs. The wind-speed profile is homogeneous right after the sunset occurred at 0233 UTC due to the evening transition, until the growth of a local wind-speed maximum located at 13 m and classified as a LLJ at 0520 UTC. Being the inertial oscillations the main driving mechanism for the LLJs detected in stable nocturnal conditions, this LLJ is probably driven by inertial oscillations. The LLJ grows in depth and magnitude during the night. The wind-speed maximum tends to be located at higher elevations while it increases, reaching a magnitude of 9.3 ms^{-1} at elevation of 51 m at 1216 UTC, which is close to the sunrise (1214 UTC). The wind direction becomes south-east in the first tens metres above the surface at 0520 UTC, which is the same hours in which the LLJ formation occurs. This phenomenon is expected because south-east is the direction of the downvalley flow considering the orientation of the valley. The wind usually rotates with respect to the height towards south as predicted by the Ekman solutions for the Northern Hemisphere (Sect. 2.9). The part of the wind profile in which the direction is south-east is characterised by the LLJ. However, some perturbations can occur in the higher levels, as during 2 of the 3 double-nose LLJs observed during the IOP4. In these profiles, the direction of the secondary nose is south-west. The wind-speed maximum is observed in the range 130 m $< z <$ 190 m, which is above the primary nose. After the sunrise, the LLJ decreases in depth and magnitude until it is completely replaced by the diurnal homogeneous flow after few hours. This phenomenon is caused by the mixing due to the thermals developed in the convective boundary layer. Therefore, the inertial period (18 hours and 34 minutes, Eq. (2.22)) is not completed; the inertial oscillations dynamics is broken by the morning transition and the following re-establishing of the convective boundary layer. Fig. 4.2c,d show respectively the evolution of the potential-temperature and relative-humidity profiles during the IOP4 as example of the spring quiescent IOPs. The potential temperature inversion, i.e. the formation of a stable boundary layer, starts from the surface at 0203 UTC, which is 30 minutes before the sunset. The inversion grows until the sunrise. The surface cooling is more accentuated during the IOP4 in which the potential temperature increases with respect to the height within the inversion up to 17 K during the pre-down hours. A large inversion usually occurs from 0 m to 50 m $< z <$ 100 m, then the inversion continues to grow until 300 m $< z <$ 400 m, but with a smaller gradient. The wind-speed maximum of the primary nose is usually located slightly before the height of the large inversion, as found by Andreas et al. (2000) (Sect. 2.7). The more the inversion height is, the higher the LLJ maximum will be, explaining why the the wind-speed maximum height increases during the night. The relative humidity RH has an opposite behaviour to the potential temperature, decreasing by approximately 30% from 0 m to 50 m $< z <$ 100 m and remaining approximately constant above in the range 12% $\leq$ RH $\leq$ 17%. This behaviour is expected because the quantity of water vapour

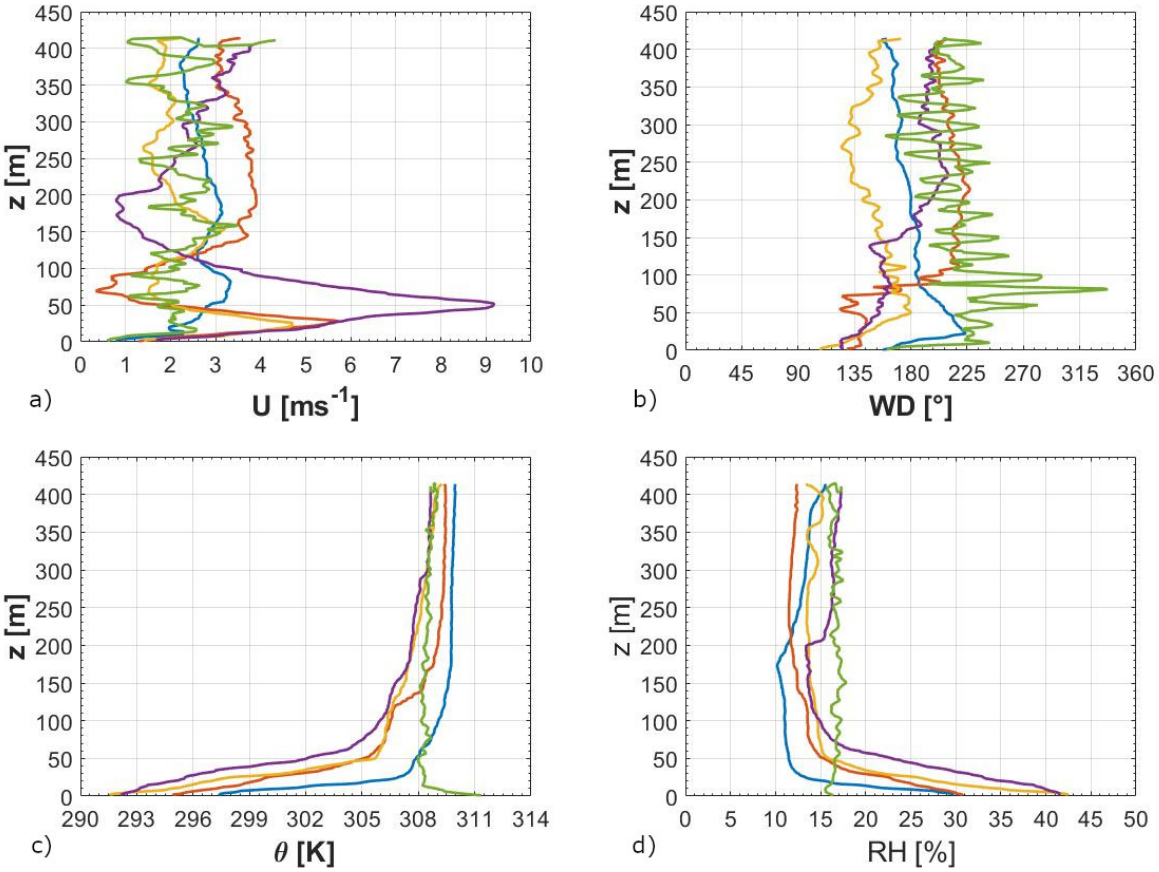

Figure 4.2: Evolution during the spring quiescent IOP4 by tethered-balloon soundings. (a) shows the wind-speed, (b) the wind direction, (c) the potential temperature, (d) the relative humidity. The blue line shows the conditions few hours after the sunset (at 0447 UTC), the red line when the downvalley LLJ is generated (at 0650 UTC), the yellow line when a double-nose LLJ occurs (at 0931 UTC), the purple line right before the sunrise (at 1142 UTC), the green line some hours after the sunrise (at 1647 UTC).

necessary to saturate an air mass increases as the temperature increases. The relative humidity decreases because it is defined as:

$$RH = \frac{w}{w_s}, \tag{4.8}$$

in which w is the mass mixing ratio of water vapour (i.e. the ratio between the water-vapour mass and the dry-air mass) and w_s the saturation mixing ratio (i.e. the same ratio but at saturation). The saturation is the macroscopic equilibrium condition in which the evaporation and the condensation rates are equal, therefore the quantity of water-vapour molecules remains unvaried when this condition is reached. Fig. 4.3a,b show respectively the evolution of the wind-speed and wind-direction profiles during the IOP8 as example of the one observed during the fall quiescent IOPs. Right after the sunset which occurs

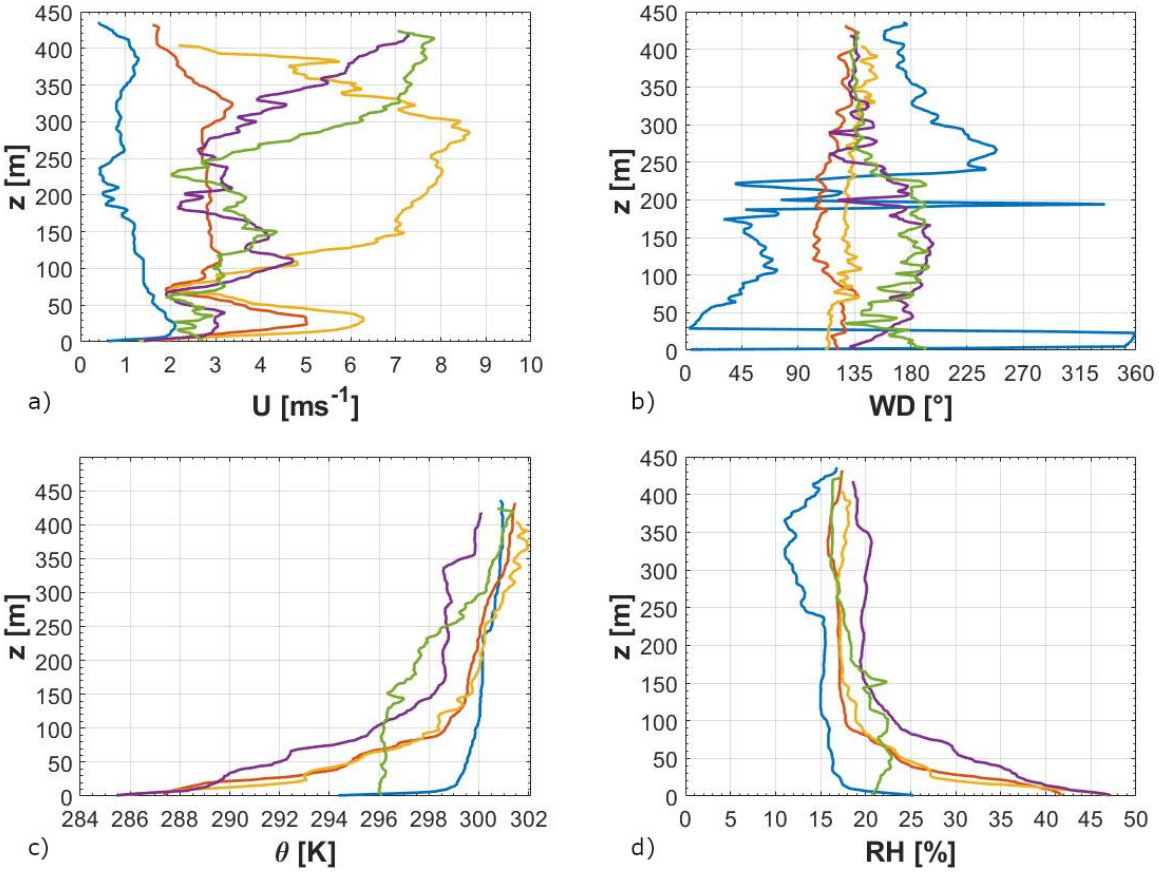

Figure 4.3: Evolution during the fall quiescent IOP8 by tethered-balloon soundings. (a) shows the wind-speed, (b) the wind direction, (c) the potential temperature, (d) the relative humidity. The blue line shows the conditions right after the sunset (at 0147 UTC), the red line when the downvalley LLJ is generated (at 0735 UTC), the yellow line when a double-nose LLJ occurs (at 0909 UTC), the purple line right before the sunrise (at 1251 UTC), the green line some hours after the sunrise (at 1621 UTC).

at approximately 0040 UTC, the wind-speed profile is characterised by a wide jet-like structure with maximum of 2 $\text{ms}^{-1} < U < 3$ ms^{-1}. This structure is not connected with the downvalley flow, since the wind direction is north. This direction could be associated with a more long-lasting period in which the diurnal upslope flow occurs. The direction becomes south-east at 0403 UTC. A wind-speed maximum is immediately generated and classified as a LLJ in the following profile measured at 0446 UTC. It grows over time showing similar features compared to the spring IOPs. However, its growth is more perturbed by intrusions from other directions. The wind direction is south or south-west at the low levels in some profiles. The intrusions interferes with the growth of the LLJ, which can also be temporarily destroyed. The wind-speed maximum does not exceed 7.0 ms^{-1} at elevation of 32 m at 0943 UTC. Any perturbation is detected at the higher

levels when 4 double-nose LLJs are detected during the IOP8. The secondary wind-speed maximum is located at a variable height in the range 130 m $< z <$ 340 m. After the sunrise the LLJ decreases in depth and magnitude until to be completely replaced by the diurnal homogeneous flow within few hours, therefore the inertial period is not completed. Fig. 4.3c,d show respectively the evolution of the potential-temperature and relative-humidity profiles during the IOP8 as example of the fall quiescent IOPs. The potential temperature inversion starts at 0041 UTC, which is approximately the time of the sunset. The inversion grows until the sunrise. The trend of the potential temperature with respect to the height is similar to the spring IOPs, therefore a large inversion occurs from 0 m to 50 m $< z <$ 100 m. The potential temperature increases with respect to the height up to 16 K. As expected, the relative-humidity profiles show a decrease with respect to the height by approximately 25% from 0 m to 50 m $< z <$ 100 m and remaining approximately constant above in the range 15% $\leq$ RH $\leq$ 21%.

4.3 The Double-nose Low-Level Jet Driving Mechanism

The formation of a LLJ structure due to inertial oscillations is typical of the examined quiescent IOPs. This LLJ dynamics starts developing after sunset and lasts until the sunrise, when the solar radiation breaks the nocturnal equilibrium. The observed LLJs are confined in a shallow 75-m atmospheric layer close to the terrain. However, external forcings can temporarily modified the LLJ structure generating a double-nose LLJ. Two

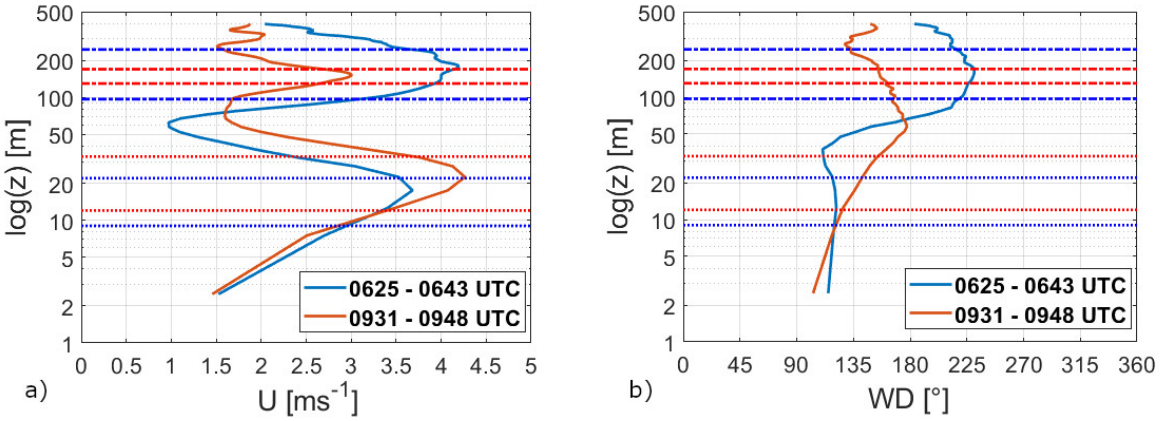

Figure 4.4: Example of double-nose LLJs retrieved during the IOP4 deriving by the two identified driving mechanisms. (a) shows the wind-speed and (b) the wind-direction profiles. The blue profile is an example of wind-driven double-nose LLJ, while the orange one of wave-driven double-nose LLJ. The horizontal lines indicate the width of the noses in the profiles represented by the same colour (dotted lines for the primary nose, dash-dot for the secondary one).

mechanisms are identified as responsible for this modification. The wind-driven mechanism describes noses associated with different air masses that flow on the Dugway Valley from different directions and at two different heights above the surface. A double-nose

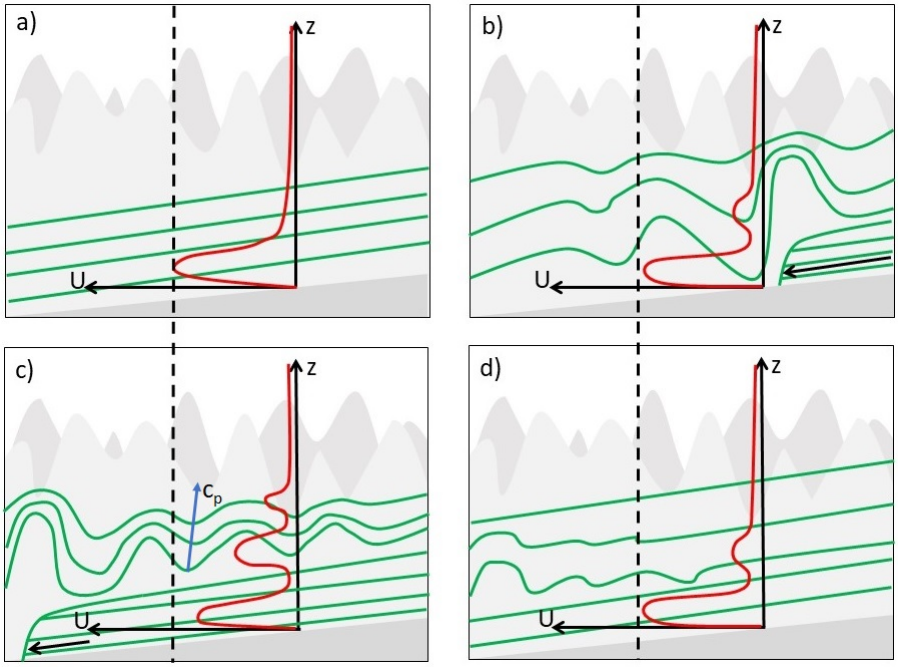

Figure 4.5: Wave-driven mechanism, namely (a) shows the LLJ formation, (b) the inertial-gravity wave generation, (c) the double-nose LLJ formation, (d) the dissipation. The green lines represent the wind-speed field. The black dashed lines report the initial LLJ wind-speed maximum to highlight the weakening of the primary nose. U is the wind speed, c_p is the phase velocity of the inertial-gravity wave.

LLJ is classified as wind-driven if the criteria defined in Sect. 4.1 are satisfied and the wind direction is different between the two air masses of at least 22.5°. Conversely, the secondary nose in the wave-driven mechanism is driven by the vertical momentum transport associated with an inertial-gravity wave caused by a horizontal flow perturbation. A double-nose LLJ is classified as wave-driven if the criteria defined in Sect. 4.1 are satisfied and the wind-direction difference between the two air masses is smaller than 22.5°. Fig. 4.4a shows two double-nose LLJs retrieved during the IOP4, driven by the two identified mechanisms, while Fig. 4.4b shows the correspondent wind-direction profiles. This thesis will focus on the wave-driven mechanism, with the aim to prove its reliability through specific double-nose LLJs analysis. The wave-driven mechanism consists of four phases, namely LLJ formation, inertial-gravity wave generation, double-nose LLJ formation and dissipation. Each phase is illustrated in Fig. 4.5. As the LLJ develops through the night of quiescent IOPs (LLJ formation, Fig. 4.5a) lateral and vertically confined intrusions of secondary downslope flows can come from the numerous slopes of the mountain chain surrounding the Dugway Valley. These secondary flows suddenly break the LLJ dynam-

ics, driving an oscillatory motion identified as an inertial-gravity wave (inertial-gravity wave generation, Fig. 4.5b). The vertical momentum transport associated with the wave subtracts inertia from the primary nose, transferring it to higher elevations where a secondary nose appears (double-nose LLJ formation, Fig. 4.5c). As the inertial-gravity wave dissipates, the LLJ restores its conventional single-nose shape (dissipation, Fig. 4.5d). The inertial-gravity wave was preferred to a pure 2D gravity wave because, although pure gravity waves have been found in stable nocturnal layers over gentle (Monti et al. 2002; Princevac et al. 2005) and steep (Chemel et al., 2009) slopes, the larger spatial domain of the valley introduces a cross-wave component giving a 3D shape to the wave. Eq. (2.17) allows to compute the momentum lost by the primary nose and gained by the secondary one as result of the wave momentum transport. The loss and gain values and their percentage ratio are then compared with a bulk estimation directly calculated from the tethered-balloon wind-speed profiles. These values are computed as the difference between the wind-speed profile where the double-nose LLJ is observed and the closest antecedent one, finding the wind-speed loss and gain in the time interval between the two profiles as a function of the height. An estimation of the momentum loss and gain M_o ($\mathrm{kgm^{-2}s^{-1}}$) from the observed profile can be obtained as the integral of the weighted wind-speed difference on each layer $z_t - z_b$ (m) normalised by the whole atmospheric depth Z (m) involved in the momentum exchange:

$$M_o = \frac{\rho}{Z} \int_{z_b}^{z_t} U_2(z) - U_1(z) dz, \tag{4.9}$$

in which U_2 is the wind speed in the profile with the double-nose LLJ and U_1 the one in the profile before.

4.4 The Double-nose Low-Level Jet Classification

18 nocturnal double-nose LLJs profiles are identified by tethered-balloon data using the criteria defined in Sect. 4.1. Some of these profiles were consecutively measured. The characterisation of them in terms of sampling period is reported in Table 4.1.
The primary and secondary noses are associated with different wind directions in 13 profiles, therefore they are accustomed to the wind-driven mechanism. The direction is usually south-east at the primary nose and south-west at the secondary one. The remaining 5 profiles are linked to the wave-driven mechanism, 2 of whom (underlined in green, Table 4.1) are analysed more in detail in Sects. 5.1, 5.2 to verify the wave-driven mechanism. Table 4.2 reports the main characteristics of primary and secondary noses retrieved for these two wave-driven double-nose LLJs. One of them is detected during the IOP4 and it is named IOP4$_a$, while the other one is detected during the IOP8 and it is named IOP8$_a$. Figure 4.6a,b shows the evolution of the wind speed from before the double-nose LLJs (preIOP4$_a$ and preIOP8$_a$) to their destruction (postIOP4$_a$ and postIOP8$_a$). The postIOP4$_a$ and postIOP8$_a$ preserve the double-nose shape but neither the primary or the secondary nose verify the LLJ identification criterion (Eq.

(4.3)), because the secondary nose is reduced and the primary one intensifies again. This phenomenon is an evidence of the secondary nose dissipation and the consequent restoring

	Double-nose LLJ profiles		
	Date	Sampling period	No. of profiles
2012 Fall	IOP0 26/09	0912 UTC – 1242 UTC	7
	IOP1 29/09	1044 UTC – 1136 UTC	2
	IOP1 29/09	1218 UTC – 1237 UTC	1
	IOP2 02/10	1231 UTC – 1255 UTC	1
	IOP8 19/10	0515 UTC – 0539 UTC	1
	IOP8 19/10	0909 UTC – 1033 UTC	3
2013 Spring	IOP4 12/05	0551 UTC – 0643 UTC	2
	IOP4 12/05	0931 UTC – 0948 UTC	1

Table 4.1: Double-nose LLJ profiles identified in MATERHORN data. Underlined in green specify the wave-driven double-nose LLJs, while underlined in blue the "uncertain" wave-driven ones.

	Wave-driven double-nose LLJs characterisation		
		0931 - 0948 UTC (IOP4$_a$)	0515 - 0539 UTC (IOP8$_a$)
Primary nose	U_{max} [ms^{-1}]	4.9	4.2
	h_{max} [m]	25	20
	WD [°]	147	104
	n_w [m]	21	6
	ν	0.90	0.95
Secondary nose	U_{max} [ms^{-1}]	3.3	4.5
	h_{max} [m]	153	132
	WD [°]	159	96
	n_w [m]	40	32
	ν	0.98	0.97
	$\lvert\Delta WD\rvert$ [°]	12	8

Table 4.2: Wave-driven double-nose LLJs characterisation by the estimation of wind-speed maximum U_{max}, height of wind-speed maximum h_{max}, wind direction WD, nose width n_w and symmetry ratio ν at both the nose. The last row reports the wind-direction difference $\Delta\, WD$ between the noses. The reported time is the sampling period in which each profile is detected by tethered balloon in Sagebrush.

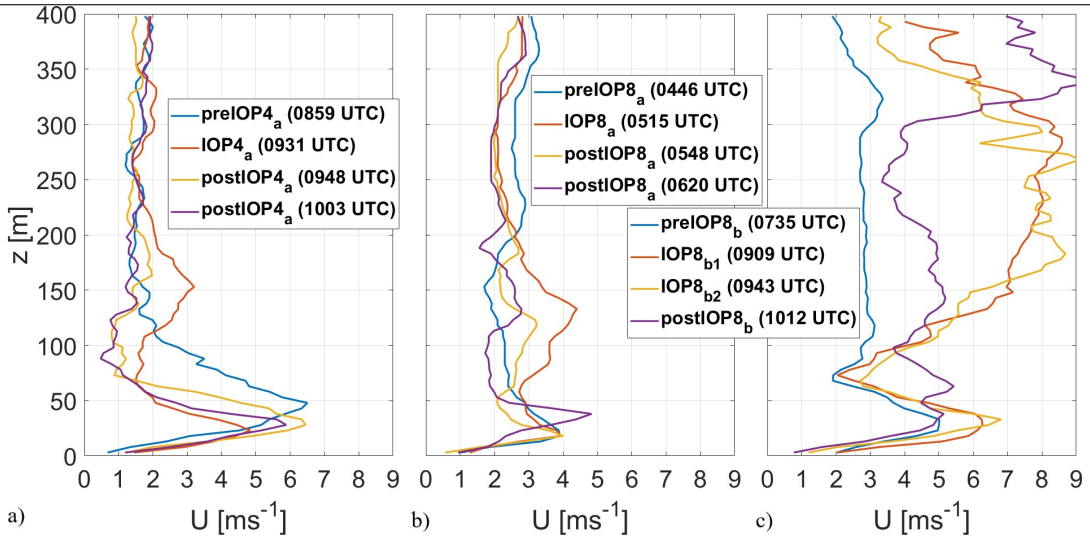

Figure 4.6: Evolution of the wind-speed profile during and after the formation of the wave-driven double-nose LLJs, IOP4$_a$ (a) and IOP8$_a$ (b), and consecutive "uncertain" wave-driven ones, IOP8$_b$ (c).

"Uncertain" wave-driven double-nose LLJs characterisation				
		0909-0928 UTC (IOP8$_b$)	0943-1002 UTC (IOP8$_b$)	1012-1033 UTC (postIOP8$_b$)
Primary nose	U_{max} [ms^{-1}]	6.4	7.0	5.2
	h_{max} [m]	30	32	146
	WD [°]	114	113	148
	n_w [m]	33	21	77
	ν	0.95	0.92	1.14
Secondary nose	U_{max} [ms^{-1}]	8.7	9.3	9.7
	h_{max} [m]	284	270	337
	WD [°]	128	127	139
	n_w [m]	177	137	23
	ν	0.83	0.85	0.99
	$\lvert\Delta WD\rvert$ [°]	14	14	8

Table 4.3: "Uncertain" wave-driven double-nose LLJs characterisation by the estimation of wind-speed maximum U_{max}, height of wind-speed maximum h_{max}, wind direction WD, nose width n_w and symmetry ratio ν at both the nose. The last row reports the wind-direction difference $\Delta\, WD$ between the noses. The reported time is the sampling period in which each profile are detected by tethered balloon in Sagebrush.

of the unperturbed condition, as expected during the fourth phase of the wave-driven mechanism described in Sect. 4.3. The driving mechanism of the other 3 profiles classified as wave-driven (underlined in blue, Table 4.1) remains uncertain because the analysis of these profiles in Sects. 5.1, 5.2 is conditioned by a lack of tethered-balloon measurements at higher elevations than the secondary nose. Table 4.3 reports the main characteristics of primary and secondary noses retrieved for these three "uncertain" wave-driven double-nose LLJs. The first two, named IOP8$_b$ in the following analysis, share similar features and probably describe the same event which lasts longer than the IOP4$_a$ and IOP8$_a$ ones. Differently from the other wave-driven profiles, the wind-speed maximum of the secondary nose is the 36% larger than the primary one. Figure 4.6c shows the evolution of the wind speed from before the double-nose LLJs (preIOP8$_b$) to their destruction (postIOP8$_b$). The postIOP8$_b$ is the third "uncertain" wave-driven profile. It has a particular shape since the two noses are located more than 100 m above the surface, and therefore neither of them is the primary one. These odd behaviours can also suggest a different formation mechanism, either driven by wave momentum transport but from the large scale flow and not the surface. This last behaviour is the explanation of why the IOP8$_b$ is not further analysed.
Considering all the double-nose LLJs, the symmetry ratio ν (Eq. (4.7)) is equal to 1.0 $\pm$ 0.10 in the 62.5% of the observed noses, describing symmetrical noses in the large majority of the identified events. The secondary nose is wider than the corresponding primary one in all the detected double-nose LLJ. The nose width (Eq. (4.6)) for the primary nose is in the range 6 m $\leq n_w \leq$ 33 m, while for the secondary one, it is ranging from 26 m $\leq n_w \leq$ 177 m.

Summary

A new criterion to identify the LLJs and the Multiple LLJs was proposed. This criterion consists of absolute and relative thresholds on the wind-speed maximum and it was formulated adapting the previous criteria of Banta et al. (2002) and Baas et al. (2009) to account for the complexity of the analysed domain and the high instrumental resolution. A new criterion to identify the wind-speed minima were also proposed to better define multiple noses within a single profile, adapting the previous criterion suggested by Baas et al. (2009). Furthermore, the nose width and the symmetry ratio were defined to characterise the nose shape in terms of width and symmetry. The newly-defined criteria and variables were used to analyse the quiescent IOPs. During them, the typical wind direction is south-east which is the direction of the downvalley flow considering the orientation of the valley. A local wind-speed maximum near the surface connected to the downvalley flow was classified as a LLJ 3 or 4 hours after the sunset. This LLJ grown in depth and magnitude until the sunrise, however some intrusions were detected. This intrusions perturbed the downvalley LLJ conditioning its growth as retrieved during the fall IOPs or driving the formation of a double-nose LLJ. A large inversion of potential temperature was detected from 0 m to 50 m $< z <$ 100 m above the surface. The pri-

mary nose was usually located few tens metres before the inversion height, as retrieved by Andreas et al. (2000). Using the newly-defined LLJ identification criterion, 18 nocturnal double-nose LLJs profiles were identified and classified considering the mechanism that drove their formation. They were classified as wind-driven when the noses are associated with different air masses, while wave-driven when the formation of the secondary nose is caused by the vertical momentum transport associated with an inertial-gravity wave due to a horizontal flow perturbation occurred at the surface. Considering all the double nose LLJ, 62.5% of the noses were classified as symmetrical. The secondary nose was larger than the primary one in all the analysed cases.

Chapter 5

Double-nose Low-Level Jets Driving Mechanism Analysis

The wave-driven driving mechanism proposed in Sect. 4.3 is verified in this chapter. In Sect. 5.1 the perturbation that causes the generation of the inertial-gravity wave is investigated for the IOP4$_a$ and the IOP8$_a$ cases observing the temperature and the wind fields retrieved by MINISAMS data and the wind speed and direction detected by the flux towers. In Sect. 5.2 the inertial-gravity waves observed before the IOP4$_a$, IOP8$_a$ and IOP8$_b$ are characterised analysing their main features. Furthermore, the wave momentum transport supposed to generate the secondary nose in the wave-driven mechanism is verified by two different methods calculated from the tethered-balloon wind-speed profiles. These two methods consists in calculating the momentum lose by the primary nose and gained by the secondary one with Eq. (2.17) proposed by Kim and Mahrt (1992) and with a bulk estimation Eq. (4.9).

5.1 The Wave-Driven Mechanism: Downvalley Low-Level Jet Perturbation

Two different mechanisms were suggested in Sect. 4.3 to drive the double-nose LLJ formation. Despite the wind-driven double-nose LLJs were found to be the most commonly observed in this thesis (Sect. 4.4), their genesis is simply associated with different air masses flowing one on top of the other. On the contrary, the theory behind the wave-driven mechanism must be proven analysing the single cases of the IOP4$_a$ and IOP8$_a$ obtained from the classification in Sect. 4.4. As a first step of this wave-driven mechanism investigation, the nature of the wave formation is tackled. A perturbation of the downvalley LLJ is found to drive the inertial-gravity wave formation. This perturbation is identified as a katabatic front intruding the valley from the Dugway Range (IOP4$_a$ event) or the Granite Peak (IOP8$_a$ event) and perturbing the downvalley flow, which is the main circulation within the Dugway Valley during the night of quiescent IOPs (IOP4$_a$ case in Fig. 5.1a, IOP8$_a$ case in Fig. 5.2a). The katabatic-front hypothesis is confirmed

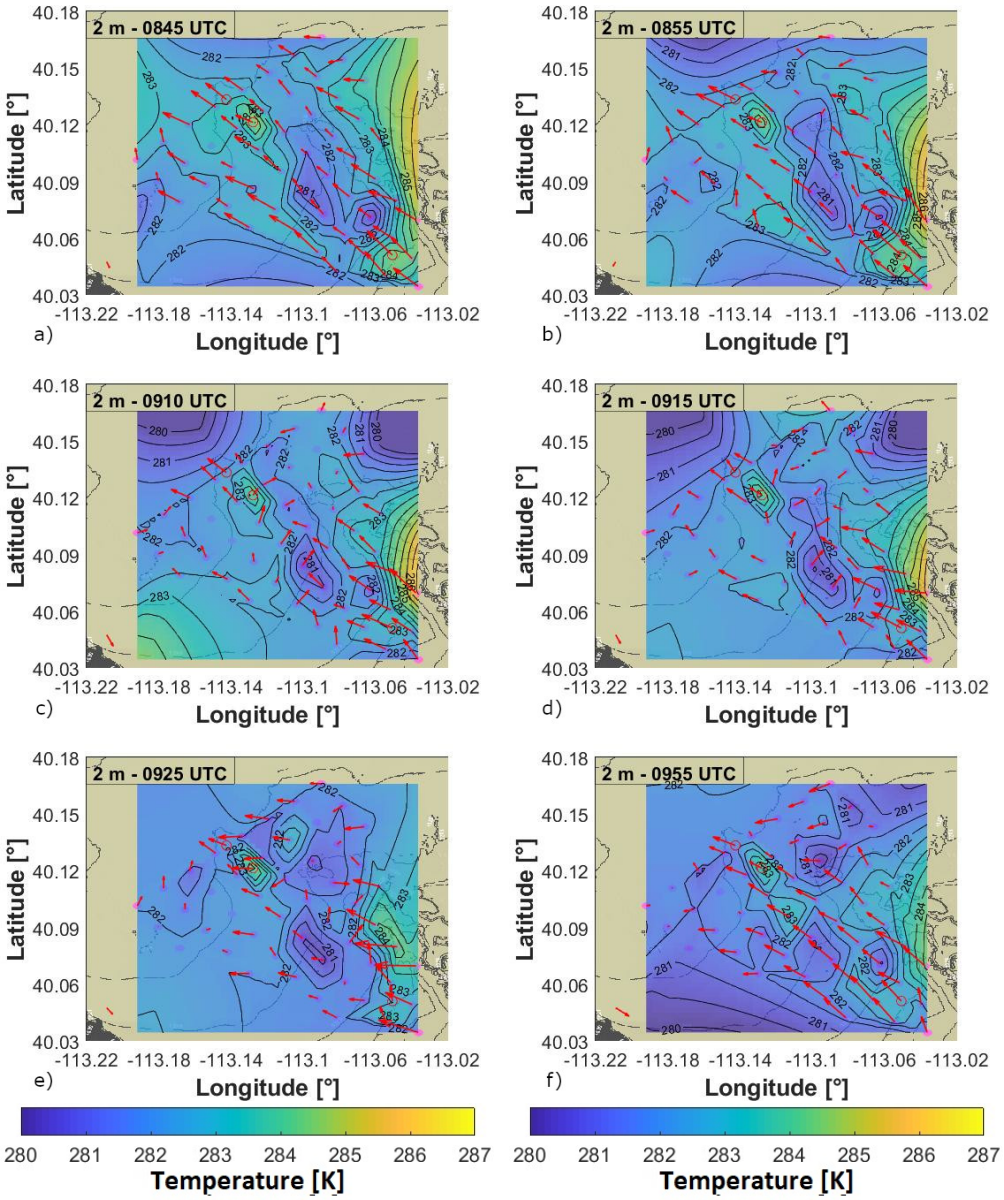

Figure 5.1: Evolution of the temperature and wind-speed fields at 2 m in Dugway Valley during the perturbation before the IOP4$_a$, identified as a katabatic front. (a) shows the downvalley flow before the katabatic front. Then, the katabatic front intrudes the valley from south-west (b), reaches Sagebrush (c), bends to north-east (d) and reaches T1 (e). (f) shows the restoring of the downvalley flow after the katabatic front. The fields are retrieved from MINISAMS and flux-towers data averaged over 5 minutes. The red dots indicate the position of the flux towers in T1, Sagebrush and T4. Temperature gradients at the edge of the colourmap are due to the numerical interpolation.

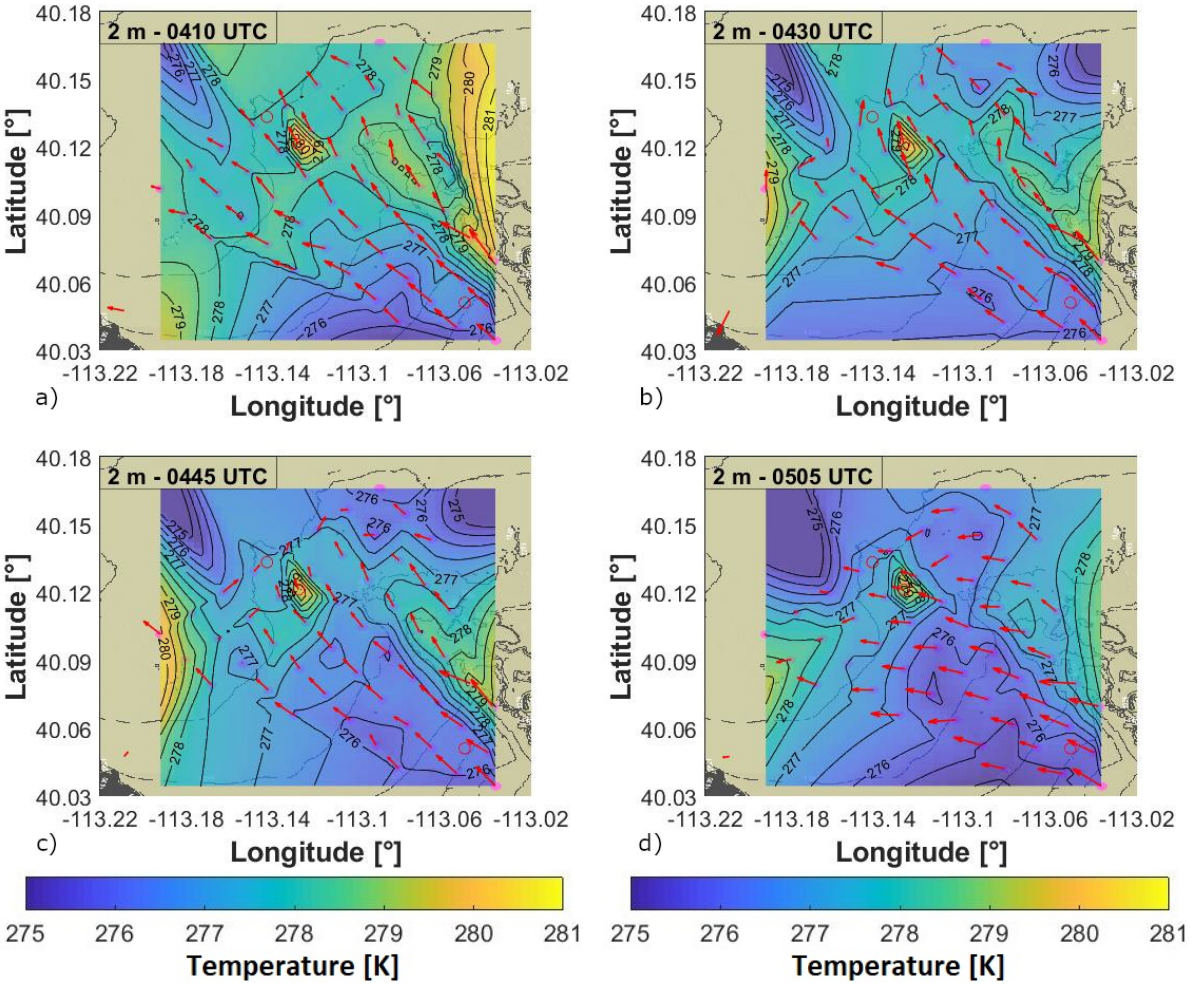

Figure 5.2: Evolution of the temperature and wind fields at 2 m in Dugway Valley during the perturbation before the IOP8$_a$, identified as a katabatic front. (a) shows the downvalley flow before the katabatic front. The katabatic front intrudes the valley from south-west (b) and propagates towards north-east (c). (d) shows the restoring of the downvalley flow after the katabatic front. The fields are retrieved from MINISAMS and flux-towers data averaged over 5 minutes. The red dots indicate the position of the flux towers in T1, Sagebrush and T4. Temperature gradients at the edge of the colourmap are due to the numerical interpolation.

by the wind vectors retrieved from the MINISAMS that show a progressive bending of direction as a flow confined at the surface intrudes the valley. The perturbation occurs from 0855 UTC to 0955 UTC during the IOP4$_a$ and from 0415 UTC to 0505 UTC during the IOP8$_a$. A possible alternative hypothesis suggests the perturbation to be driven by a channelling flow through the Gap. However, this hypothesis is rejected because the SAMS located at the entrance of the Gap does not detect wind directions oriented toward the

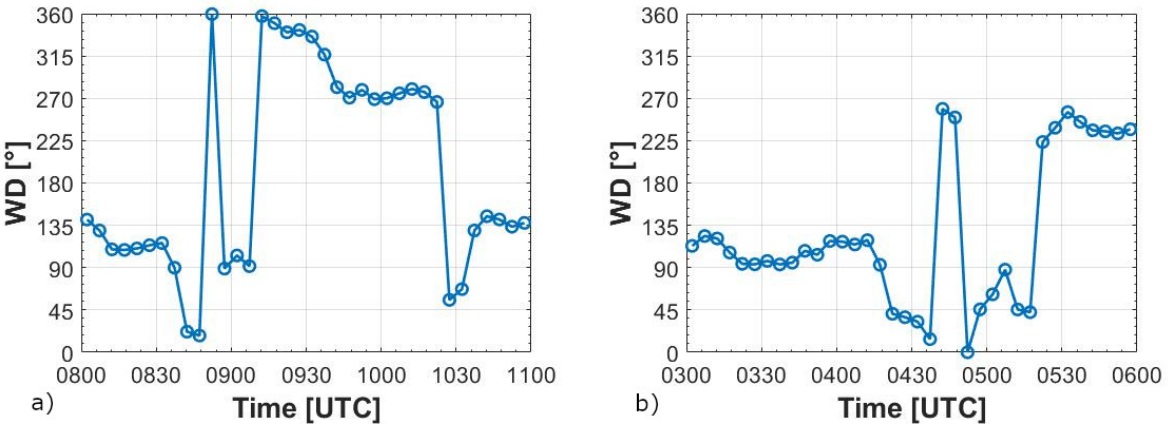

Figure 5.3: Time series of the wind direction retrieved by the SAMS located at the entrance of the GAP before and after the IOP4$_a$ (a) and the IOP8$_a$ (b) cases.

Dugway Valley during or just before the perturbation in the IOP4$_a$ event and only when the perturbation had been already started in the IOP8$_a$ one (between 0440 UTC and 0450 UTC). Figure 5.3 shows the wind-direction time series retrieved by the considered SAMS before and after the IOP4$_a$ and the IOP8$_a$ cases.
During the perturbation before the IOP4$_a$, the wind-direction bending from south-east to south-west starts at 0855 UTC from the closest MINISAMS to the northern side of the Dugway Range (Fig. 5.1b). The perturbation initially propagates northward involving Sagebrush between 0905 UTC and 0915 UTC (Fig. 5.1c) and then it propagates north-eastward (Fig. 5.1d) avoiding T4. Successively, the southern side of the valley, included T1, is affected by the perturbation between 0920 UTC and 0930 UTC (Fig. 5.1e). This delay on the perturbation arrival time could be due to different slopes characterising the complex terrain of the valley. Finally, the perturbation ends at 0955 UTC, after 60 minutes from its beginning, and the unperturbed downvalley flow is restored (Fig. 5.1f). The temperature field does not significantly change during the propagation of the perturbation. However, a lowering of approximately 0.5 K is measured by the MINISAMS, suggesting similar temperatures for the downvalley flow and the katabatic front. The effect of the perturbation is detailed through the flux towers located in Sagebrush and T1. The arrival of the perturbation coincides with the tilt of the wind direction (dot-marked lines, Fig. 5.4b,d) and the damp of the wind speed (dot-marked lines, Fig. 5.4a,c) caused by the collision between the two air masses. This wind-speed damp occurs at 0911 UTC at Sagebrush and at 0928 UTC at T1. Simultaneously, a wave-like motion associated with an inertial-gravity wave is detected in the surface layer at both Sagebrush and T1 (dot-marked lines in Fig. 5.4a,c). The perturbation is confined in the first 10 m above the surface supporting the hypothesis of the katabatic front. The constraint of the perturbation near the surface is also confirmed by the tethered-balloon soundings measured at Sagebrush (cross-marked lines in Fig. 5.4a,b) that showed a different dynamics with respect to the MINISAMS and the flux-tower data. Figure 5.4a also shows an increase of

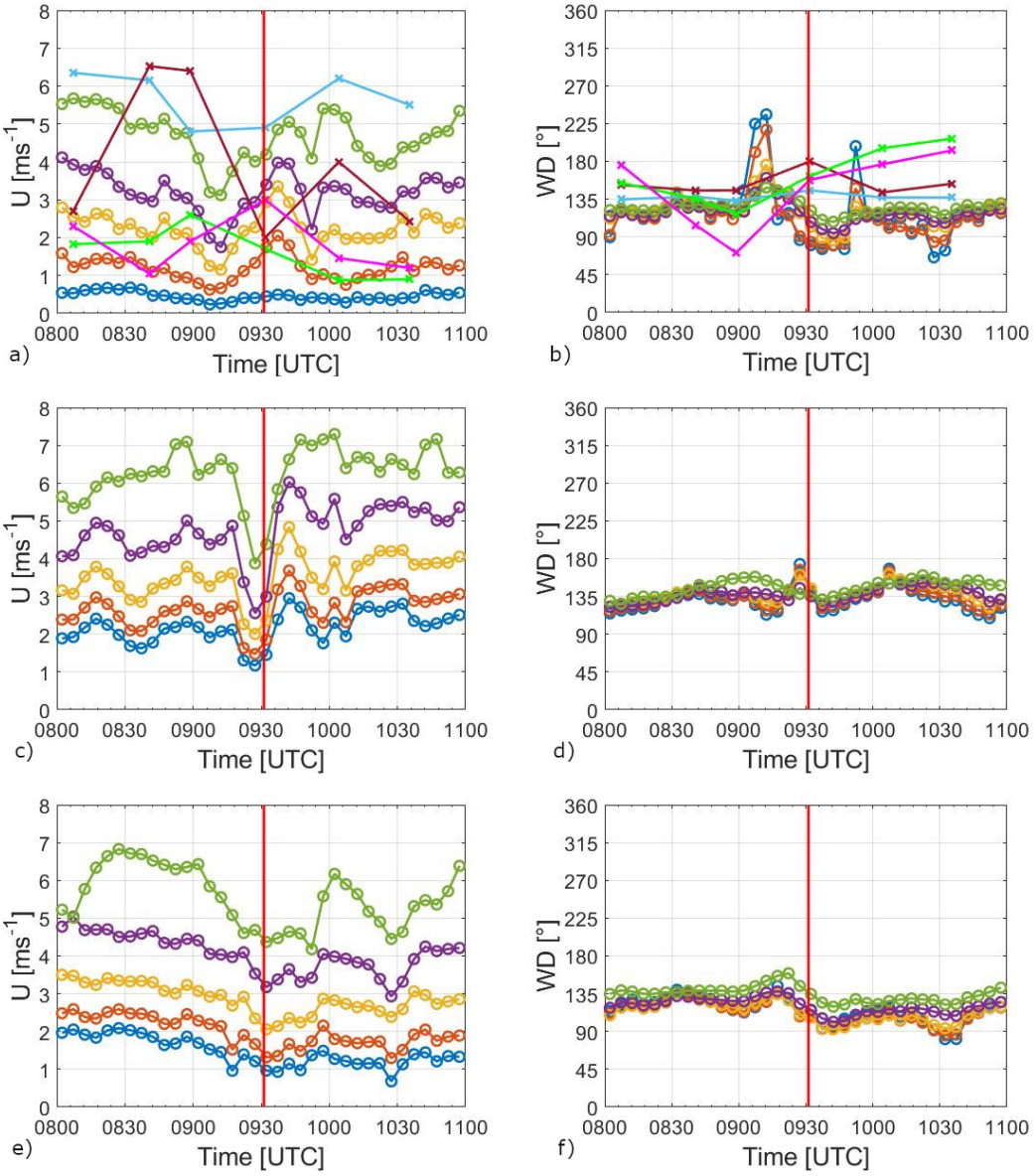

Figure 5.4: Time series averaged over 5 minutes of the wind speed at Sagebrush (a), T1 (c) and T4 (e) and of the wind direction at Sagebrush (b), T1 (d) and T4 (f) before and after the IOP4$_a$ case. The dot-marked lines show measurements by sonic anemometers at elevation of 0.5 m (blue), 2 m (orange), 5 m (yellow), 10 m (purple), 20 m (light green) at Sagebrush and at 2 m (blue), 4 m (orange), 8 m (yellow), 16 m (purple), 28 m (light green) at T1 and T4. The cross-marked lines in (a) and (b) show measurements by tethered balloon at 25 m (light blue), 50 m (dark red), 100 m (green), 150 m (pink) at Sagebrush. The red line indicates the time in which the tethered balloon starts to measure the IOP4$_a$ at Sagebrush.

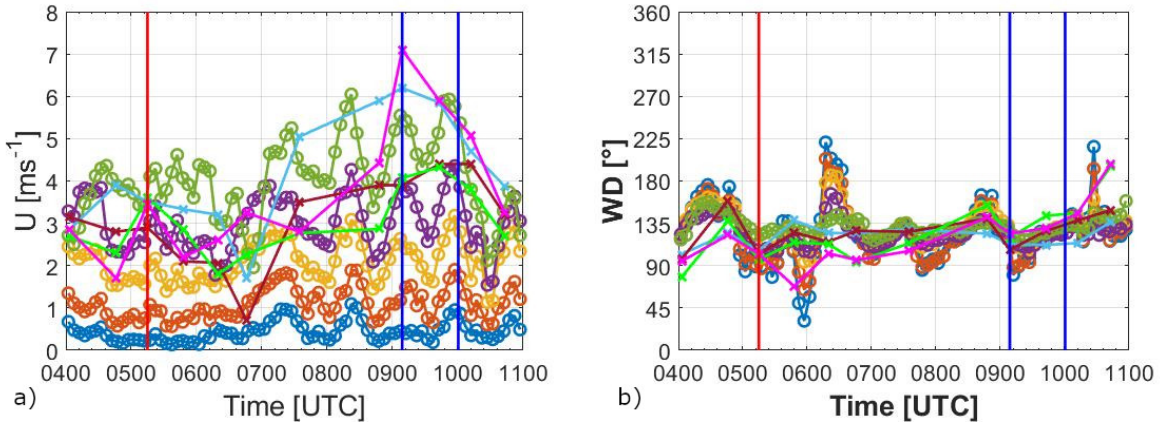

Figure 5.5: Time series averaged over 5 minutes of the wind-speed (a) and of the wind direction (b) at Sagebrush before and after the IOP8$_a$ and IOP8$_b$ cases. The dot-marked lines show measurements by sonic anemometers at elevation of 0.5 m (blue), 2 m (orange), 5 m (yellow), 10 m (purple), 20 m (light green), while the cross-marked lines show measurements by tethered balloon at 25 m (light blue), 50 m (dark red), 100 m (green), 150 m (pink). The red line indicates the time in which the tethered balloon starts to measure the IOP8$_a$, the blue lines the sampling period in which the IOP8$_b$ is measured.

wind speed at 150 m, height involved in the secondary-nose generation after the surface perturbation.

The IOP8$_a$ shows a similar evolution. Before the IOP8$_a$, a bending of the wind vectors is retrieved by the MINISAMS starting at 0415 UTC. The perturbation starts from the nearest MINISAMS to the southern side of the Granite Peak (Fig. 5.2b) and propagates towards north-east (Fig. 5.2c) involving the northern area of the Dugway Valley and Sagebrush. Finally, the perturbation ends at 0505 UTC, after 50 minutes from its beginning, and the unperturbed downvalley flow is restored (Fig. 5.2d). During the IOP8$_a$ case, the air temperature decrease is more pronounced than during the IOP4$_a$ event. However it does not affect only the MINISAMS involved by the katabatic front but also the entire Dugway Valley, and it can not be directly connected to the perturbation. The effect of this perturbation retrieved at the Sagebrush flux tower, is similar to the IOP4$_a$ case, showing a tilt of the wind direction (dot-marked lines, Fig. 5.5b) and a damp of the wind speed (dot-marked lines, Fig. 5.5a) in the first 10 m above the surface. Figure 5.5a also shows the generation of an inertial-gravity wave at 0502 UTC, 30 minutes after the beginning of the wind-speed damp that occurs on a longer time than the IOP4$_a$ case starting at 0432 UTC and continuing until 0502 UTC. Likewise to the IOP4$_a$, the different dynamics showed by tethered-balloon soundings confirms the constraint of the perturbation near the surface (cross-marked lines in Fig. 5.5a,b). Fig. 5.5a shows the increase of wind speed at higher heights (100 m and 150 m), between which a secondary nose is generated after the perturbation.

5.2 The Wave-Driven Mechanism: Wave Momentum Transport

The katabatic front perturbation described in Sect. 5.1 temporarily modifies the mean flow field in an atmospheric depth close to the ground. The modification of the mean flow field consists in a tilt of the wind directions and in a damp of the wind speeds producing a momentum drop. As a consequence a wave-like motion is triggered. By hypothesis in Sect. 4.3, the wave-like motion is associated with an inertial-gravity wave. Despite a wave is also detected at T1 before the IOP4$_a$, from now on only the waves detected at Sagebrush are considered to better compare the IOP4$_a$ and the IOP8$_a$ events and to directly associate the sonic-anemometers measurements with the tethered-balloon ones. During the IOP4$_a$ event, the wind-speed damp occurs at 0911 UTC, simultaneously to the generation of an inertial-gravity wave and 26 minutes before the observation of a double-nose LLJ profile (Fig. 5.6a). Instead, during the IOP8$_a$ event the wind-speed damp occurs on a longer time, since it starts at 0432 UTC and continues until 0502 UTC, when a inertial-gravity wave is generated (Fig. 5.6b). The generation of the wave occurs 20 minutes before the observation of a double-nose LLJ profile. The inertial-gravity waves characterisation of both these events is reported in Table 5.1. The waves periods T_w and the vertical phase

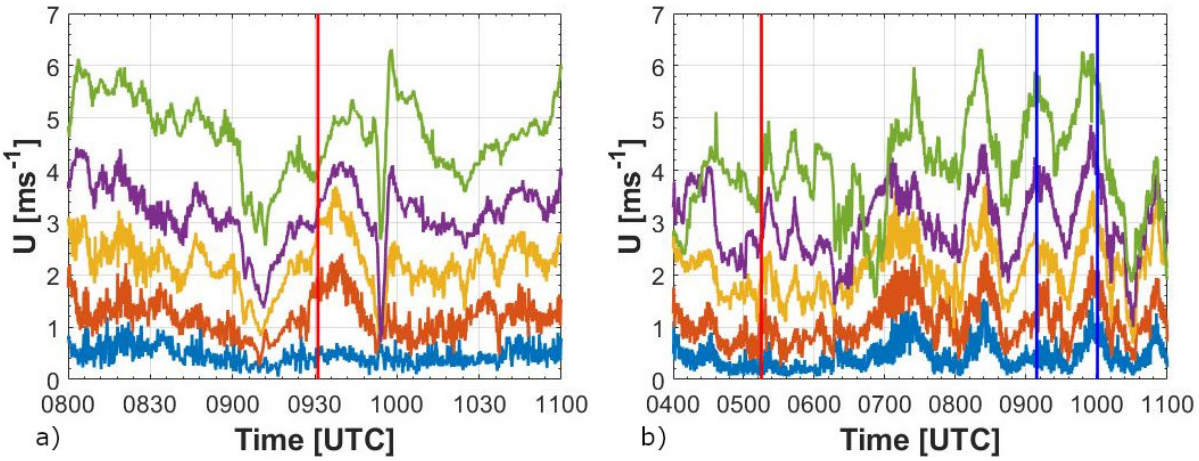

Figure 5.6: Time series averaged over 10 seconds of the Brunt-Väisälä frequency squared N^2 before and after the IOP4$_a$ (a), the IOP8$_a$ and IOP8$_b$ (b). The measurements are retrieved by sonic anemometers at elevation of 0.5 m (light-blue), 2 m (orange), 5 m (yellow), 10 m (purple), 20 m (green). The red line indicates the time in which the tethered balloon starts to measure the IOP4$_a$ in (a) and the IOP8$_a$ in (b), the blue lines the sampling period in which the IOP8$_b$ is measured.

velocity c_{pz} are computed with the 10-s average to detail the time lapse between wave crests or troughs at different flux-tower levels. The data used to characterised the wave in each analysed case were detected at the elevation of 5 m, 10 m and 20 m. The data retrieved at 0.5 m are not considered because they could conditioned by the presence of

	Inertial-gravity waves characterisation		
	$IOP4_a$	$IOP8_a$	$IOP8_b$
N^2 [s^{-2}]	$(7 \pm 1) \times 10^{-3}$	$(13 \pm 1) \times 10^{-3}$	$(6 \pm 1) \times 10^{-3}$
T_w [s]	1000 ± 100	1300 ± 400	2700 ± 300
ω [$rads^{-1}$]	$(6.0 \pm 0.6) \times 10^{-3}$	$(5 \pm 2) \times 10^{-3}$	$(2.3 \pm 0.3) \times 10^{-3}$
c_{pz} [ms^{-1}]	$(2.5 \pm 0.6) \times 10^{-1}$	$(1.7 \pm 0.6) \times 10^{-1}$	$(-2.0 \pm 0.4) \times 10^{-1}$
ϕ [°]	85.88 ± 0.01	87.51 ± 0.02	88.29 ± 0.01

Table 5.1: Inertial-gravity waves characterisation by the estimation of the Brunt-Väisälä frequency squared N^2 during the wave formation, period T_w, intrinsic frequency ω, vertical phase velocity c_{pz} and propagation angle ϕ.

the terrain. The data retrieved at 2 m are not also considered because the wave signal is less regular than at the higher elevations. The period is calculated as twice the averaged time between two subsequent crests or troughs observed at each elevation. The error is the standard deviation of each period at each elevation. The phase velocity is computed as the difference between two consecutive flux-tower levels heights s divided by the time lapse between the observed troughs at the same heights t. Only the first observed trough of the time series is considered because it corresponds to the minimum wind-speed retrieved during the damp and to the wave formation and upwards propagation begin. The error associated with the phase velocity is derived by the error-propagation theory considering $\delta t = 10$ s as the error of the time lapse. The general equation to propagate the error associated to a generic variable $x\,(a, b)$ is

$$\delta x = \left|\frac{\partial x}{\partial a}\right| \delta a + \left|\frac{\partial x}{\partial b}\right| \delta b. \tag{5.1}$$

The inertial-gravity waves related to $IOP4_a$ and $IOP8_a$ have similar period T_w and vertical phase velocity c_{pz}. Accordingly, they also have similar intrinsic frequency ω calculated from Eq. (2.16). The Brunt-Väisälä frequency squared N^2 that characterised each case is computed from the flux-tower data averaged over 5 minutes considering the values right before, at and right after the wave formation, i.e. when the wind-speed damp occurs. Figure 5.7 shows the time series of N^2 before and after each analysed case at elevation of 10 m and 20 m. This time series are obtained by

$$N^2 = \frac{g}{\theta_r}\frac{\partial \theta}{\partial z}, \tag{5.2}$$

in which ρ_r is a reference potential temperature assumed equal to the one measured at 0.5 m averaged over 5 minutes intervals. The associated error δN^2 is obtained calculating

the standard deviation as error of the temperature T and pressure P used to calculate the potential temperature θ at each level by Eq. (2.5) and propagating the error by Eq. (5.1). N^2 is larger in the IOP8$_a$ case than the IOP4$_a$ one. This difference in stability between the two cases could explain why the perturbation is more long-lasting during the IOP8$_a$ case than the IOP4$_a$ one because the more stability implicates that the considered atmosphere is more elastic. The hypothesis of an almost vertical propagation proposed in Sect. 4.3 is confirmed by the estimation of the propagation angle ϕ (Eq. (2.15)). As reported on Table 5.1, $\phi \approx 90°$ describes an almost vertical phase propagation for the IOP4$_a$ and the IOP8$_a$ cases. The time that the inertial-gravity wave takes to reach the elevation of the secondary nose is $\Delta t_4 = 9$ minutes during the IOP4$_a$ case and $\Delta t_{8a} = 12$ minutes during the IOP8$_a$ one, which is almost T/2 in both cases. Since the delay time between the wind-speed damp at the surface (0911 UTC before the IOP4$_a$ and 0502 UTC before the IOP8$_a$) and the observation of the double-nose LLJ (0937 UTC in the IOP4$_a$ and 0522 UTC in the IOP8$_a$) is respectively 26 minutes and 20 minutes, the inertial-gravity wave has enough time to bring momentum from the surface to the atmospheric layer where the secondary wind-speed maximum is detected (100 m $< z <$ 200 m).

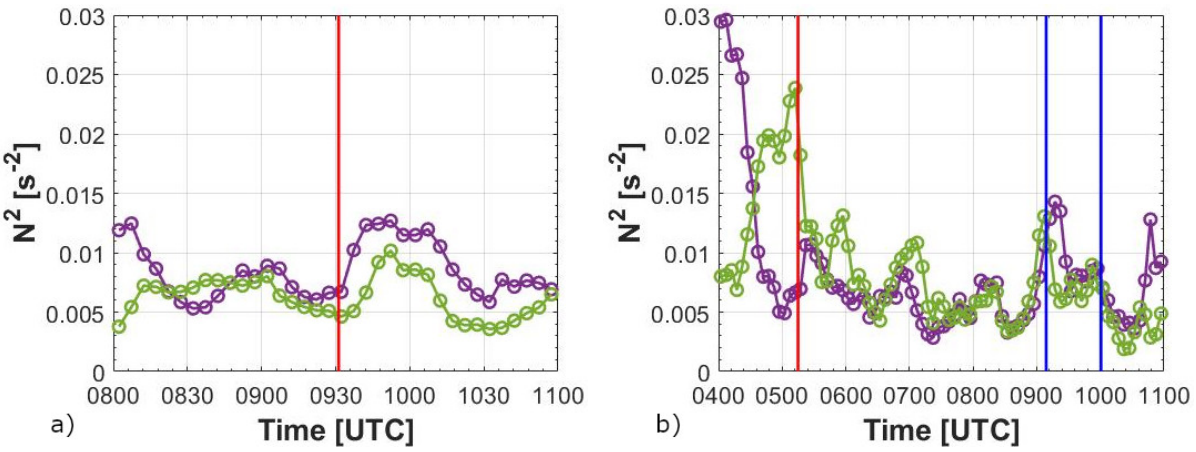

Figure 5.7: Time series averaged over 5 minutes of the Brunt-Väisälä frequency squared N^2 before and after the IOP4$_a$ (a), the IOP8$_a$ and IOP8$_b$ (b). The dot-marked lines show measurements by sonic anemometers at elevation of 10 m (purple), 20 m (green). The red line indicates the time in which the tethered balloon starts to measure the IOP4$_a$ in (a) and the IOP8$_a$ in (b), the blue lines the sampling period in which the IOP8$_b$ is measured.

The fundamental hypothesis at the basis of the wave-driven mechanism states that the wave generated by a LLJ perturbation is the carrier of the momentum loss by the primary nose at the surface, transported upward and gained by the secondary nose. The estimations of momentum loss and gain proposed in Sect. 4.3 to verify this hypothesis is applied for the IOP4$_a$ and IOP8$_a$ cases. Eq. (2.17) is used to compute the momentum profiles (IOP4$_a$ case, Fig. 5.8a, IOP8$_a$ case, Fig. 5.9a) associated with the inertial-gravity waves. The momentum profile computed for the IOP4$_a$ case shows two well-defined layers in the first 250 m, respectively characterised by a momentum loss between 0 m and 100

m and a momentum gain between 100 m and 250 m. These momentum loss and gain are quantified from Eq. (2.17):

$$M_w^{loss} \approx -12.0 \text{ ms}^{-1} \text{ from } z_i = 0 \text{ m to } z_f = 100 \text{ m}$$
$$M_w^{gain} \approx 8.89 \text{ ms}^{-1} \text{ from } z_i = 100 \text{ m to } z_f = 250 \text{ m},$$

corresponding to a momentum gain to loss ratio of approximately the 74%. The retrieved percentage can be interpreted as the amount of momentum transported from the surface to the layer above, carried by the inertial-gravity wave. The remaining 26% is either transported above the secondary wind-speed maximum depth or dissipated by the wave, straightening the condition to have a dispersive wave as momentum carrier. Computing

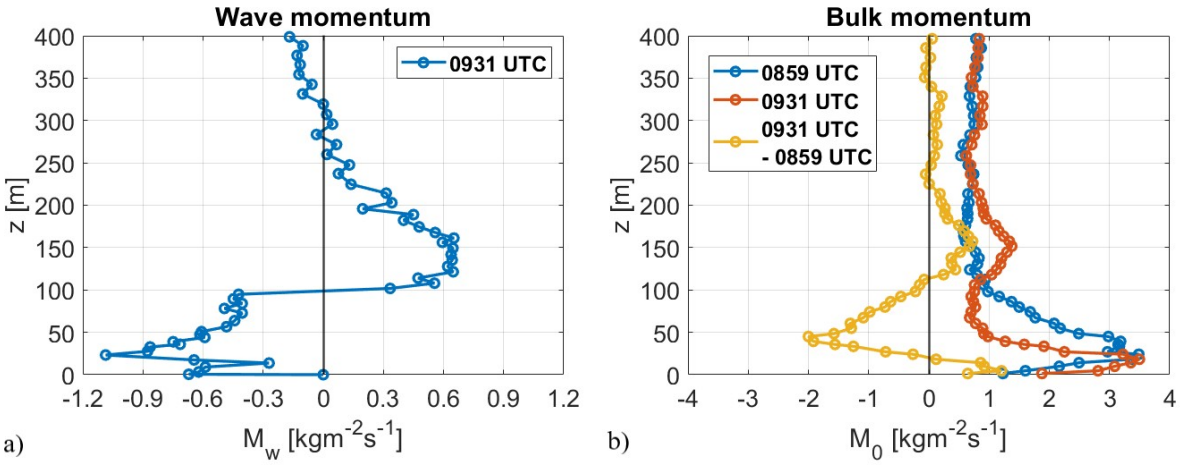

Figure 5.8: Evaluated wave momentum (a) from Eq. (2.17) and observed wind-speed profiles (b) at 0859 UTC (preIOP4$_a$) in blue, 0931 UTC (IOP4$_a$) in orange and the difference U(0931 UTC) - U(0859 UTC) between them in yellow.

the difference between the IOP4$_a$ wind-speed profile (0931 UTC) and the preIOP4$_a$ one (0859 UTC), the wind-speed loss and gain between the two profiles is obtained as a function of the height (Fig. 5.8b). This is a bulk estimation because the perfect profile to compare the double-nose LLJ with would have been at 0911 UTC corresponding to the wave generation, but the preIOP4$_a$ encircles the best time resolution possible. Following the same procedure adopted for the wave momentum gain and loss estimations, Eq. (4.9) is used to compute the bulk momentum loss between 0 m and 100 m and gain between 100 m and 250 m. The computation gives the following results:

$$M_o^{loss} \approx -16.0 \text{ ms}^{-1} \text{ from } z_i = 0 \text{ m to } z_f = 100 \text{ m}$$
$$M_o^{gain} \approx 11.2 \text{ ms}^{-1} \text{ from } z_i = 100 \text{ m to } z_f = 250 \text{ m},$$

corresponding to a momentum gain to loss ratio of approximately the 70%. Both momentum gain and loss absolute values and percentage exchanges find a very good agreement

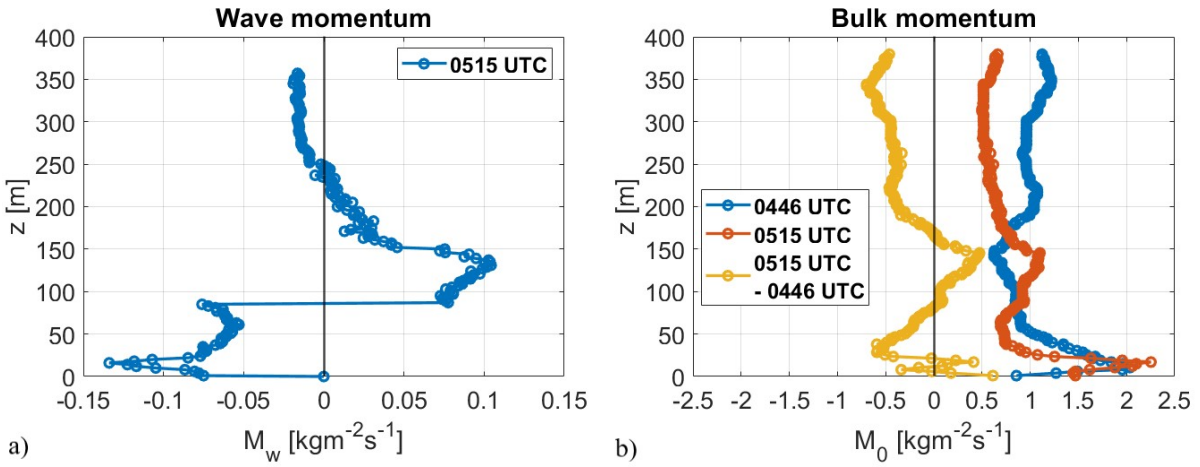

Figure 5.9: Evaluated wave momentum (a) from Eq. (2.17) and observed wind-speed profiles (b) at 0446 UTC (preIOP8$_a$) in blue, 0515 UTC (IOP8$_a$) in orange and the difference U(0515 UTC) - U(0446 UTC) between them in yellow.

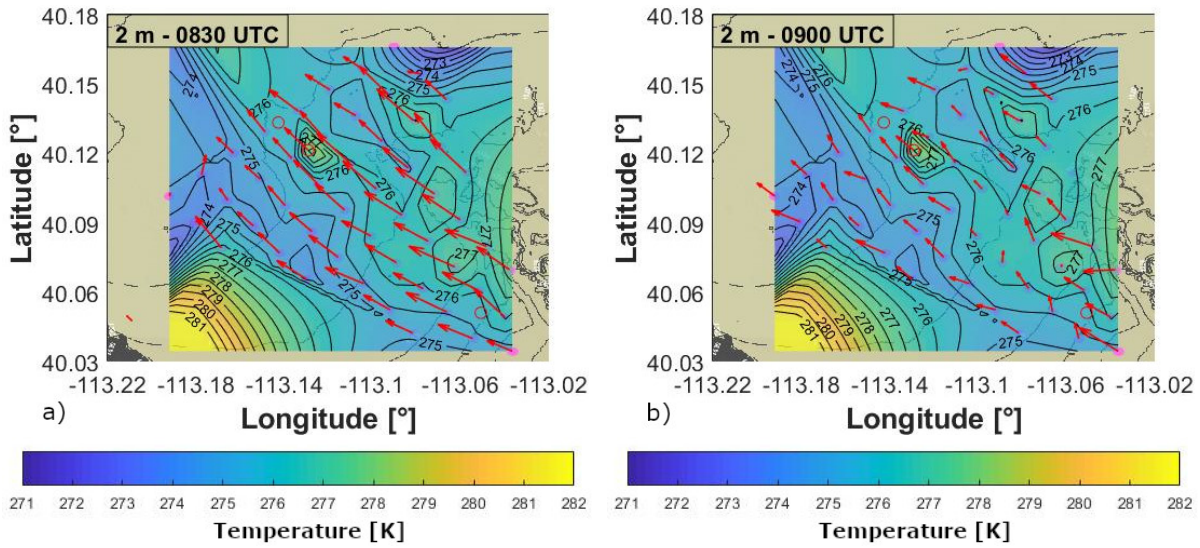

Figure 5.10: Evolution of the temperature and wind fields at 2 m in Dugway Valley before and at the beginning of the IOP8$_a$. The fields are retrieved from MINISAMS and flux-towers data averaged over 5 minutes. The red dots indicate the position of the flux towers in T1, Sagebrush and T4. Temperature gradients at the edge of the colourmap are due to the numerical interpolation.

between the two evaluation methods, despite a certain overestimation of the absolute values computed with the bulk calculation. This agreement corroborate the initial hypothesis, confirming the double-nose LLJ observed in Fig. 5.8b is generated by the momentum transport of an inertial-gravity wave from the surface ($z < 100$ m) to the above layer (100 m $< z <$ 250 m). A supplementary confirmation is also provided by the IOP8$_a$ among

which the same comparison is performed with similar results (Fig. 5.9). Evaluating the wave momentum gain and loss as done for the IOP4$_a$, a ratio of the 89% is obtained from

$$M_w^{loss} \approx -6.02 \text{ ms}^{-1} \text{ from } z_i = 0 \text{ m to } z_f = 85 \text{ m}$$
$$M_w^{gain} \approx 5.36 \text{ ms}^{-1} \text{ from } z_i = 85 \text{ m to } z_f = 170 \text{ m}.$$

Analogously, the bulk momentum gain to loss ratio retrieved directly from the IOP8$_a$ wind-speed profile (0515 UTC) minus the preIOP8$_a$ one (0446 UTC) gives a 84%, obtained from

$$M_o^{loss} \approx -9.03 \text{ ms}^{-1} \text{ from } z_i = 0 \text{ m to } z_f = 85 \text{ m}$$
$$M_o^{gain} \approx 7.58 \text{ ms}^{-1} \text{ from } z_i = 85 \text{ m to } z_f = 170 \text{ m}.$$

Compared to the IOP4$_a$, the momentum transported is smaller as smaller is the secondary-nose momentum as retrieved from Fig. 5.9. The efficacy of the momentum transport is although larger in IOP8$_a$ probably due to the smaller atmospheric depth where the double-nose LLJ has developed.
In addition to the IOP4$_a$ and IOP8$_a$ cases, another case addressed as IOP8$_b$ was classified as wave-driven in Sect. 4.4. Despite the absence of a surface perturbation involving Sagebrush before or at the beginning of the IOP8$_b$ (Fig. 5.10), a wave motion is detected from the sonic-anemometers data (Fig. 5.6b). As reported in Table 5.1, this wave is characterised by a larger period and a negative vertical phase velocity, accounting for downward momentum propagation. It could be originated by a perturbation at a higher level than the range 0 m $< z \leq$ 400 m in which the tethered balloon collected the data not allowing to verify this hypothesis. To be thorough, this case was reported as a possible wave-driven double-nose LLJ, but it was not detailed due to the limited available measurements.

Summary

The objective of the current chapter was to verify the hypothesis of the wave-driven mechanism for the double-nose LLJ events, IOP4$_a$ and IOP8$_a$. The results of the analyses show that lateral and vertically confined intrusions of secondary downslope flows in the form of a katabatic front can perturb the LLJ nocturnal evolution by breaking the LLJ dynamics and inducing a damp in the surface-layer wind speed and a tilt of the wind direction. This perturbation was found to generate an oscillatory motion identified as an inertial-gravity wave characterised by similar period and vertical phase velocity during the IOP4$_a$ and IOP8$_a$. The inertial-gravity wave vertically transports momentum from the primary nose to a higher elevation where a secondary nose appears. The wave momentum transport was successfully verified calculating the momentum loss by the primary nose and gain by the secondary one. The results obtained by the equation of the inertial-gravity momentum transport proposed by Kim and Mahrt (1992) (Eq. (2.17)) and by the bulk estimation (Eq. (4.9)) are in agreement. Despite an inertial-gravity wave is also detected during the IOP8$_b$, the generation of this wave is not preceded by a surface perturbation.

Since the vertical phase velocity retrieved for this case is negative, the generation of this wave could be due to a perturbation that occurs at a higher height than the maximum one at which the tethered balloon measured data. This lack of data does not allow to verify this hypothesis.

Chapter 6

Low-Level Jets Simulation

At this point in this thesis, the analysis will be completed by presenting two analytical models for the prediction of the standard LLJs. Specifically, the IOP4 and the IOP7 are selected to be simulated through the flat-terrain model proposed by Van de Wiel et al. (2010) (Sect. 2.9) and the sloped-terrain one proposed by Shapiro and Fedorovich (2009) (Sect. 2.10) to verify if the evolution of the LLJs retrieved in the MATERHORN dataset is in agreement with the theory of the inertial oscillations. Section 6.1 describes the simulation of the tethered-balloon profiles using the Van de Wiel's model, while Sect. 6.2 describes the simulation of them using the Shapiro and Fedorovich's model, which is extended to the three-dimensional case and adapted considering the orientation of the Dugway Valley. Section 6.3 reports the simulation of the hodographs using both the models.

6.1 Van de Wiel's Model

6.1.1 IOP4 Simulation

Following the identification criteria in Sect. 4.1, the first LLJ observed during the IOP4 occurred at 0520 UTC, therefore few hours after the sunset which occurs at 0233 UTC. The wind-speed maximum is observed at 13 m with a magnitude of 4.3 ms^{-1}. This LLJ grows in magnitude and depth during the night, reaching the maximum speed of 9.3 ms^{-1} (51 m) at 1142 UTC, in proximity of the sunrise (1214 UTC).
The model proposed by Van de Wiel et al. (2010) is used to verified if the evolution of this LLJ is driven by the inertial-oscillations, following the hypothesis in Sect. 4.2. From now on this model is referred to as VdW. Eqs. (2.49), (2.50) are solved in a Matlab program to retrieved the nocturnal evolution of the wind-speed profile. This profile is simulated in the range 0 m $< z \leq$ 400 m (measurement range of the tethered-balloon) with vertical spatial step of 5 m. Despite the sunset occurs at 0233 UTC, the initial conditions U_{in} are chosen in agreement to the speed U and direction WD profiles measured at 0447 UTC (Fig. 6.1) because it is the first profile antecedent to the LLJ formation in which a

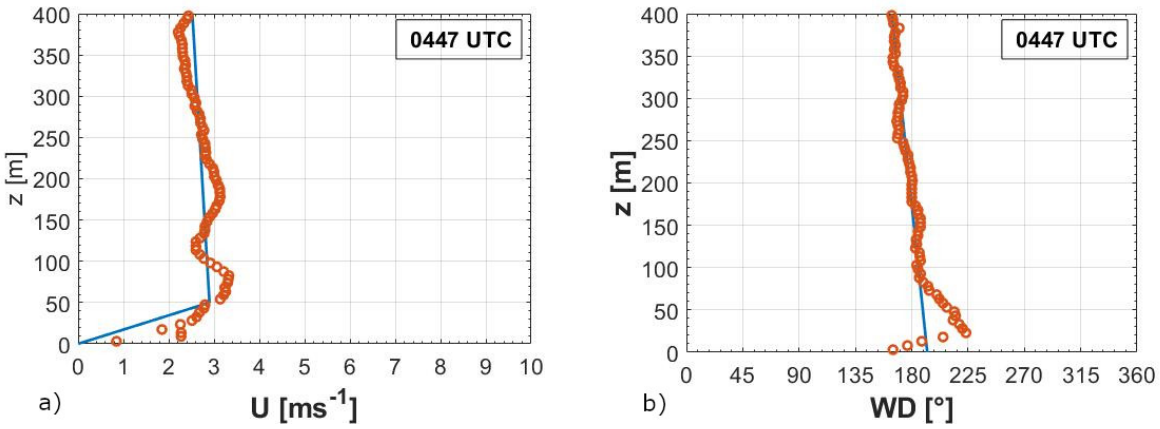

Figure 6.1: Comparison between the initial conditions used in the simulation of the IOP4 (solid blue line) and the measured tethered-balloon profile used to extrapolate it (dot-marked orange line). (a) shows the wind speed and (b) the wind direction.

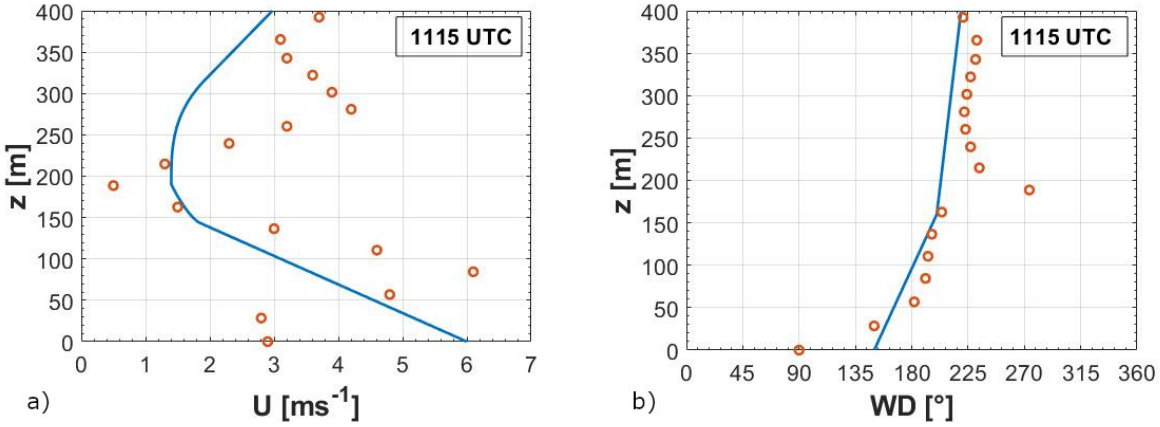

Figure 6.2: Comparison between the geostrophic wind used in the simulation of the IOP4 (solid blue line) and the measured radiosonde profile used to extrapolate it (dot-marked orange line). (a) shows the wind speed and (b) the wind direction.

wind-speed maximum is observed near the surface, but not yet classified as a LLJ. This profile represents the beginning of the LLJ dynamics. The model requires a geostrophic profile U_g (Fig. 6.2) to calculate the nocturnal equilibrium profile (dash orange line, Fig. 6.3) by means of the Ekman solutions (Eqs. (2.51), (2.52)). The geostrophic profile is evaluated considering the radiosonde launched at 1115 UTC, extrapolating the wind-speed maximum at the surface as suggested by Van de Wiel et al. (2010) and the trend of the wind-speed profile is smoothed to avoid abrupt variations. U_{in} and U_g are chosen considering coarse approximation of the real profiles because the objective of the current

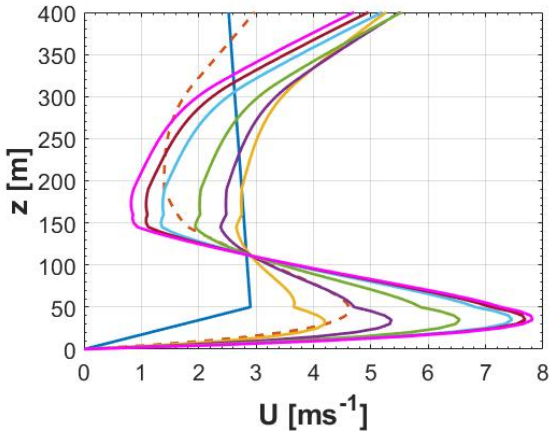

Figure 6.3: Simulation of the IOP4 through the VdW. The solid blue line is the initial profile, the dash orange line is the equilibrium profile. The simulation is computed at 0659 UTC (yellow), 0806 UTC (purple), 0931 UTC (green), 1104 UTC (light-blue), 1142 UTC (red), 1216 UTC (pink).

simulation is to reproduce the general evolution of the downvalley LLJ. The eddy viscosity K_m used in the Ekman solutions to obtain the equilibrium profile is assumed equal to 0.05 m^2s^{-1}, which is the nocturnal average value retrieved by the flux tower located ad Sagebrush and equipped with sonic anemometers. The eddy viscosity is obtained by

$$K_m = -\frac{\overline{w'u'}}{\frac{d\bar{u}}{dz}}, \tag{6.1}$$

in which $\overline{w'u'}$ (m^2s^{-2}) is the turbulent kinetic momentum flux and $\frac{d\bar{u}}{dz}$ (s^{-1}) is the vertical shear. Figure 6.3 shows the simulation of the IOP4 starting from the sunset, which is chosen as $t = 0$ s. Despite the inertial-oscillations theory proposed by Blackadar (1957) (Sect. 2.8) predicted the LLJ reaches the maximum development after half inertial period (Eq. (2.22)), the LLJ simulated with the VdW continues to grow for a longer time. This phenomenon is also reported by Van de Wiel et al. (2010) (Sect. 2.9). Considering the latitude of the Dugway Valley, the half inertial period is equal to 9 hours and 17 minutes. The magnitude of the LLJ maximum still increases after 9 hours and 53 minutes (1216 UTC, pink line, Fig. 6.3). Fig. 6.4 shows the comparison between each simulated profile with the measured one. The model cannot simulate the growth of the LLJ depth and the resulting increase of the wind-speed maximum height. The model always predicts the maximum located at 35 m, apart from the early stages of the LLJ growth where the simulated maximum is located at 30 m. The model does not give good results of the initial growth of the jet (Fig. 6.4a) because it underestimates the maximum by 1.4 ms^{-1} and the simulated LLJ is wider than the measured one. The agreement between the simulated and the measured LLJ maximum improves during the LLJ growth (Fig. 6.4b), in which the underestimation of the wind-speed maximum is equal to 0.9 ms^{-1} in this

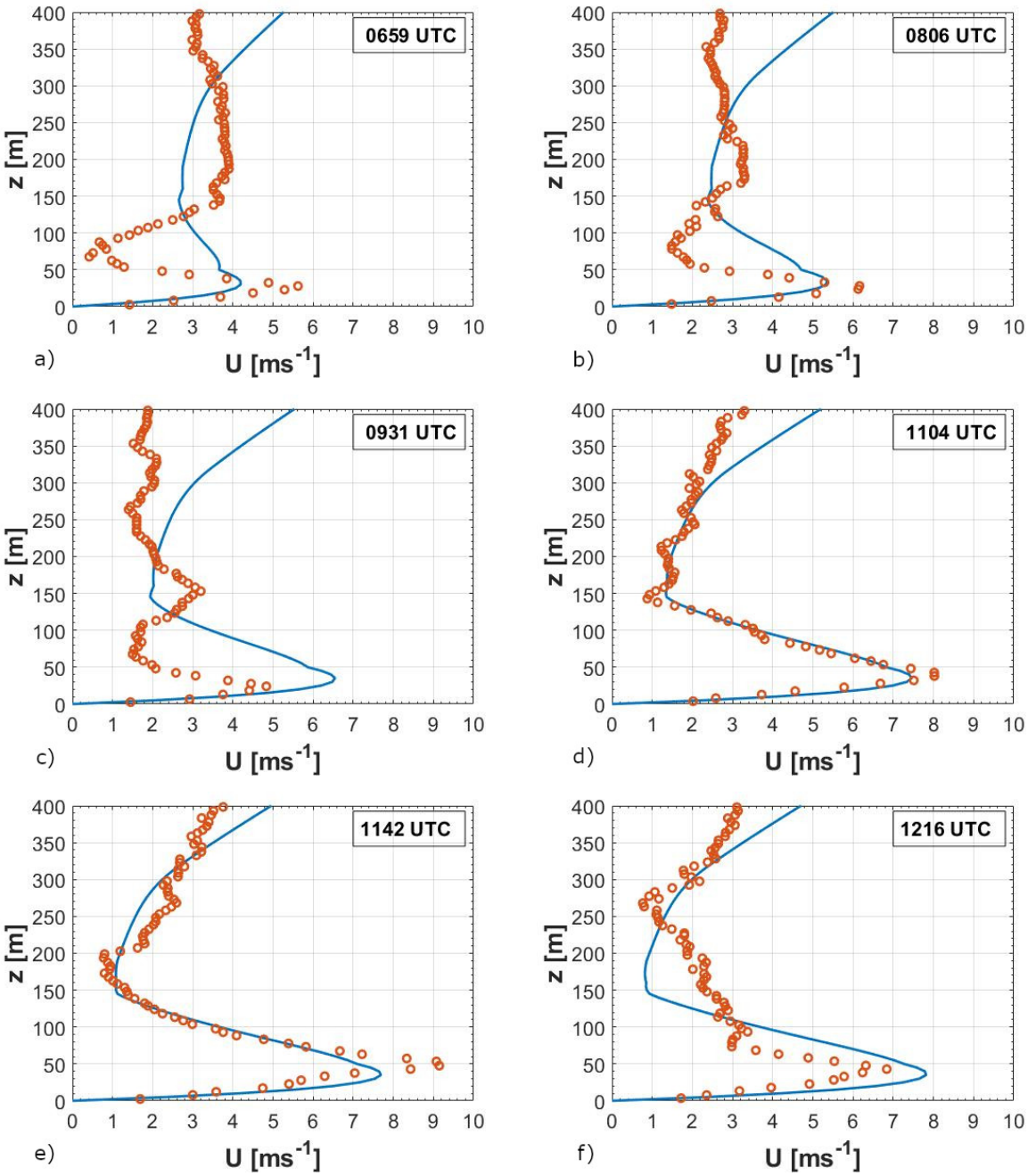

Figure 6.4: Comparison between the simulated (solid blue line) and the measured (dot-marked orange line) tethered-balloon profiles for the IOP4 through the VdW.

profile. The formation of the secondary nose during the IOP4$_a$ case due to the verified vertical momentum transport is not predicted by the model (Fig. 6.4c). This profile is completely different from the measured one, further confirming that the formation of

the secondary nose is not driven by inertial oscillations. When the secondary nose is dissipated, the primary LLJ grows again and the simulation is in good agreement with the measured profile (Fig. 6.4d). The wind-speed maximum is slightly underestimated (0.5 ms^{-1}), but it is located at the same height of the measured one and the shape of the profile is well simulated until 300 m. From the profile in Fig. 6.4d, the wind-speed maximum is observed to increase of 1.0 ms^{-1} in the next 38 minutes (Fig. 6.4e) and from that decreases of 2.3 ms^{-1} in after another 33 minutes (Fig. 6.4f). These abrupt changes are not captured by the simulation, in which the maximum grows of 0.2 ms^{-1} between Fig. 6.4d and Fig. 6.4f. As reported by Van de Wiel et al. (2010), many physical effects can dominate over inertial oscillations, therefore these abrupt changes may not be connected to the inertial-oscillations dynamics. Despite the VdW considers a flat-terrain situation, the general shape of the LLJ is also well simulated when it is fully developed over complex terrain. Nevertheless, the model fails to correctly capture the initial development of the LLJ.

6.1.2 IOP7 Simulation

Following the identification criteria in Sect. 4.1 the first LLJ observed during the IOP7 occurred at 0543 UTC, therefore few hours after the sunset (0241 UTC). This LLJ is

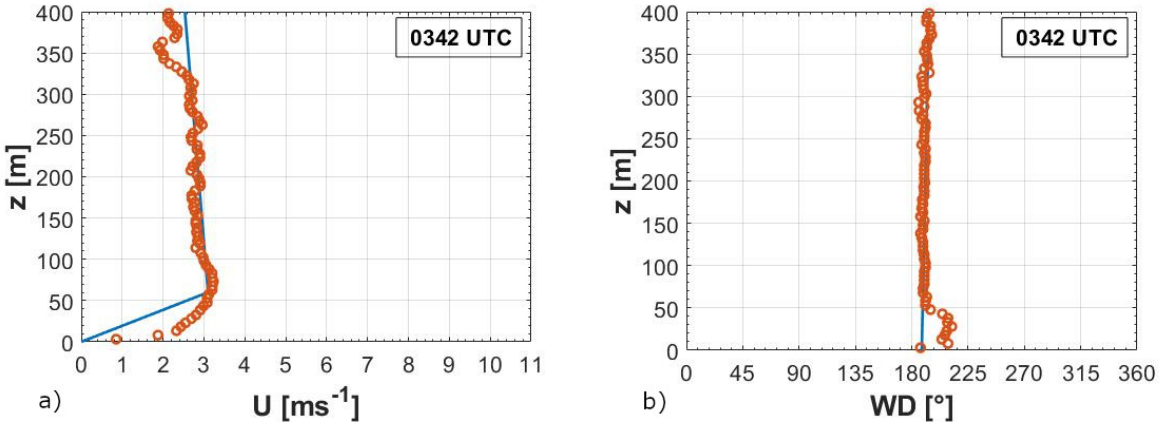

Figure 6.5: Comparison between the initial condition used in the simulation of the IOP7 (solid blue line) and the measured tethered-balloon profile used to extrapolate it (dot-marked orange line). (a) shows the wind speed and (b) the wind direction.

characterised by a wind-speed maximum of 4.4 ms^{-1} located at 25 m. The LLJ grows in magnitude and depth during the night reaching the maximum speed of 11.7 ms^{-1} (66 m) at 1243 UTC, until shortly after the sunrise (1206 UTC). Despite the wind-speed profile measured at 0342 UTC is not classified as a LLJ using the identification criteria (Sect 4.1), is the first profile antecedent to the LLJ formation in which a wind-speed maximum is detected at few tens metres above the surface. Therefore, the initial

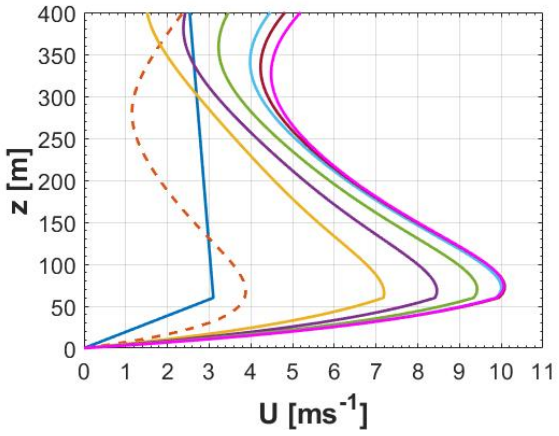

Figure 6.6: Simulation of the IOP7 through the VdW. The solid blue line is the initial profile, the dash orange line is the equilibrium profile. The simulation is computed at 0650 UTC (yellow), 0803 UTC (purple), 0921 UTC (green), 1048 UTC (light-blue), 1120 UTC (red), 1203 UTC (pink).

conditions are chosen in agreement with this profile (Fig. 6.5). Since any radiosonde is launched during the night of the IOP7, the geostrophic profile which is necessary to obtained the equilibrium profile (dash orange line, Fig. 6.6) is built on the basis of the IOP4 one, considering that the fully-developed LLJ is wider and characterised by a wind-speed maximum located at approximately 70 m. The eddy viscosity $K_m = 0.1$ m^{2}s^{-1} is evaluated by flux-tower measurements and used to retrieve the equilibrium profile using the Ekman solutions (Eqs. (2.51), (2.52)). Figure 6.6 shows the simulation of the IOP7 choosing the sunset as $t = 0$ s. The vertical step used in the simulation is 5 m and the measured profile are averaged over 5 m. As during the IOP4, the half inertial period is equal to 9 hr and 17 minutes. A profile measured 9 hr and 34 minutes after the sunset is simulated (1203 UTC, pink line, Fig. 6.6). Differently to the IOP4, The wind-speed maximum decreases in this profile compered to the previous one (1120 UTC, red line, Fig. 6.6). Fig. 6.7 shows the comparison between each simulated profile with the measured one. As during the IOP4, the model cannot capture the growth of the LLJ depth and the resulting increase of the wind-speed maximum height from 25 m to 75 m. However, the model predicts a weak increase of the wind-speed maximum height over the time, which is 65 m at the beginning of the LLJ formation and 75 m when the LLJ is fully developed. Despite this problem influences the simulation during the initial development of the LLJ, the magnitude of the maximum is predicted by the model with an underestimation of only 0.2 ms^{-1} (Fig. 6.7a). The agreement between the shape of the simulated and measured profiles increases during the LLJ growth but the maximum is more underestimated in Fig. 6.7b,c. The underestimation is 0.9 ms^{-1} in these profiles. Then, the LLJ decreases in depth in the measured profiles and the model cannot simulate this change, therefore the simulation worsen in Fig. 6.7d,e and the maximum is respectively overestimated by 0.5 ms^{-1} and underestimated by 0.6 ms^{-1}. The measured LLJ depth grows again when the

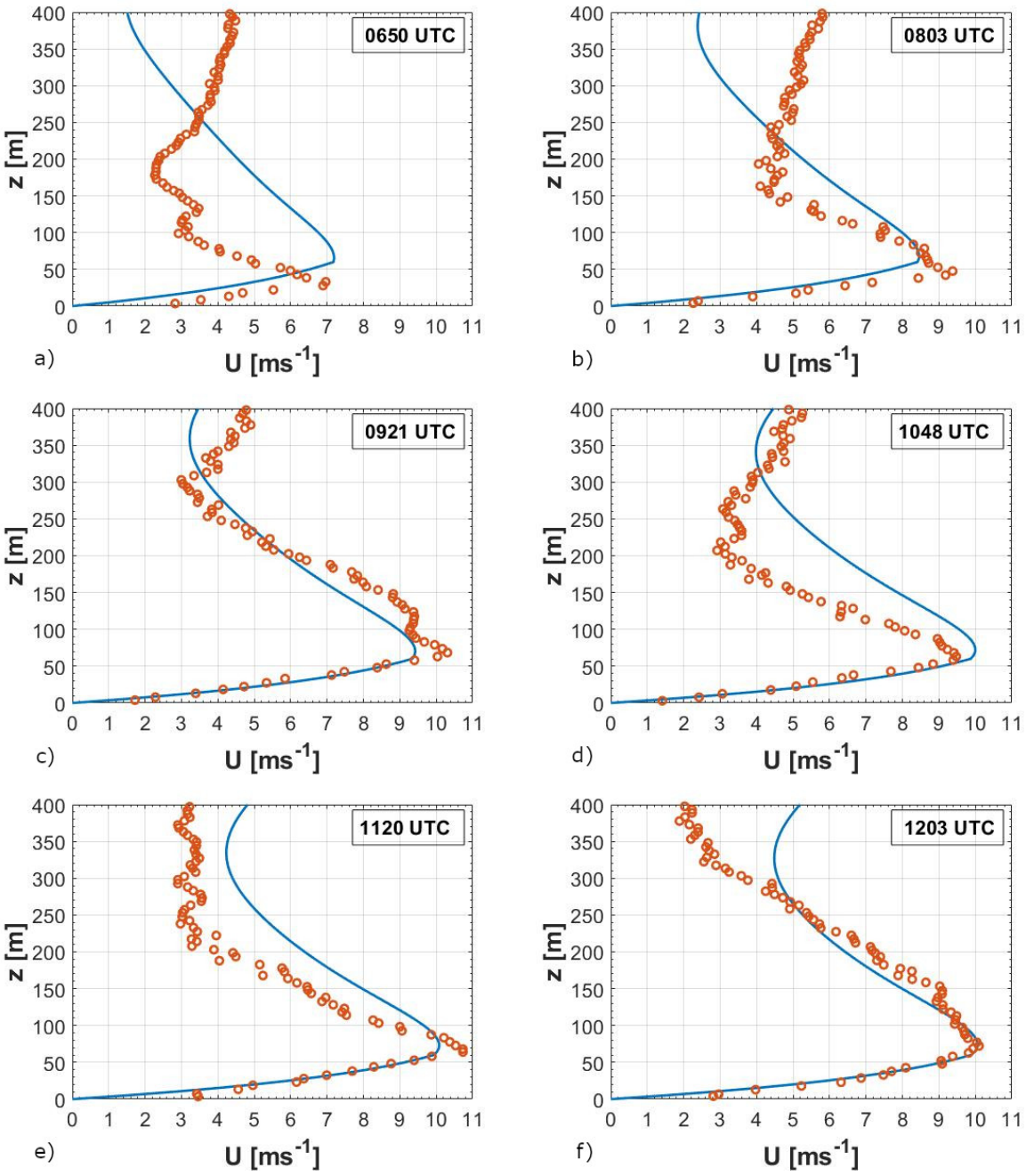

Figure 6.7: Comparison between the simulated (solid blue line) and the measured (dot-marked orange line) tethered-balloon profiles for the IOP7 through the VdW.

LLJ is fully developed and the LLJ is well simulated (Fig. 6.7f). Therefore, the results obtained simulating the IOP7 are in agreement with the one obtained from the IOP4. The IOP7 case confirms the VdW can simulate the general shape and features of the LLJ

over complex terrain when the LLJ is fully developed.

6.2 Shapiro and Fedorovich's Model

Despite the fully-developed LLJs are well simulated with a flat-terrain model as the VdW, the same simulations are repeated through the sloped-terrain model proposed by Shapiro and Fedorovich (2009) to understand if the simulations improve considering the role of buoyancy on the local thermal circulation and introducing information on the sloped terrain which characterises the Dugway Valley. Being the model proposed by Shapiro and Fedorovich (2009) considers the buoyancy, they analysed the case of inertial-gravity oscillations.

6.2.1 Adaption of the Shapiro and Fedorovich's model

The model proposed by Shapiro and Fedorovich (2009) and introduced in Sect. 2.10 is modified before to be used to simulate the two spring quiescent IOPs. From now on this model is referred to as SF. The original version was a two-dimensional model in the (x,y) plan. The modification extends the model to the third dimension applying the model in the range 0 m $< z \leq$ 400 m with vertical spatial step of 5 m. The model is vertical extended in this way because the inertial oscillations are independent on the height. Shapiro and Fedorovich (2009) restricted the analysis to the particular case $\bar{U}_g = (\bar{u}_g = 0, \bar{v}_g > 0)$, instead a variable geostrophic wind with respect to the height is considered in the current analysis. However, the same geostrophic profile used in the VdW cannot be used because in SF the geostrophic profile is the equilibrium one while in VdW served to compute the equilibrium. Therefore, the geostrophic wind-speed maximum cannot be extrapolated at the ground but it must represent a realistic profile. To avoid this problem, the geostrophic-wind profile used in the VdW is modified considering a linear trend between the surface and the height in which the fully-developed LLJ is detected during each analysed IOP. The direct dependence of the SF from the geostrophic-wind profile is a point against the use of this model because it is more sensitive to the choice of this profile which is difficult to evaluate near the surface.
Shapiro and Fedorovich (2009) studied the case of a gentle slope oriented from west to east to simulate the Great Plains. The data analysed in the current thesis were detected in the Dugway Valley, which is oriented from south-east to north-west, therefore the two cases are differently oriented of 135°. The Equations (2.65),(2.66),(2.67) are obtained again for a planar slope oriented from south to north. Despite the orientation from south to north is an approximation, this orientation is close to the one that characterised the Dugway Valley differing of only 45°. The starting equations for the nocturnal case considering the

slope oriented from south to north (subscript sn) are:

$$\frac{\partial \bar{u}_{sn}}{\partial t} = +f\bar{v}_{sn} - f\bar{v}_g \tag{6.2}$$

$$\frac{\partial \bar{v}_{sn}}{\partial t} = -b_{sn}sin(\alpha) - f\bar{u}_{sn} + f\bar{u}_g \tag{6.3}$$

$$\frac{\partial b_{sn}}{\partial t} = \bar{v}_{sn}N^2 sin(\alpha) \tag{6.4}$$

Deriving Eq. (6.3) with respect to time and substituting the derivative of $\bar{u}_{sn}$ and b_{sn} respectively from Eq. (6.2) and (6.4), the following equation is obtained:

$$\frac{\partial^2 \bar{v}_{sn}}{\partial t^2} = -\bar{v}_{sn}N^2 sin(\alpha) - f^2\bar{v}_{sn} + f^2\bar{v}_g. \tag{6.5}$$

Considering the inertial-gravity oscillations frequency ω defined in Eq. (2.63), the Eq. (6.5) can be rewritten as:

$$\frac{\partial^2 \bar{v}_{sn}}{\partial t^2} = -\omega^2\bar{v}_{sn} + f^2\bar{v}_g. \tag{6.6}$$

To find the particular solution, the independence of $\bar{v}_{sn}$ with respect to time is assumed, obtaining

$$\bar{v}_{sn} = \frac{f^2\bar{v}_g}{\omega^2}. \tag{6.7}$$

Then, the associated homogeneous equation is considered:

$$\frac{\partial^2 \bar{v}_{sn}}{\partial t^2} = -\omega^2\bar{v}_{sn}, \tag{6.8}$$

which admits solution of the form

$$\bar{v}_{sn} = A\cos(\omega t) + D\sin(\omega t). \tag{6.9}$$

The general solution for the horizontal wind-speed component $\bar{v}_{sn}$ is

$$\bar{v}_{sn} = A\cos(\omega t) + D\sin(\omega t) + \frac{f^2\bar{v}_g}{\omega^2}. \tag{6.10}$$

Substituting Eq. (6.10) in Eq. (6.2) and integrating with respect to time, the solution for the other horizontal component $\bar{u}_{sn}$ is obtained:

$$\bar{u}_{sn} = \frac{Af}{\omega}\sin(\omega t) - \frac{Df}{\omega}\cos(\omega t) + \frac{f^3\bar{v}_g t}{\omega^2} - f\bar{v}_g t + C. \tag{6.11}$$

Deriving Eq. (6.10) with respect to time and substituting in Eq. (6.3), the solution for the buoyancy b_{sn} is obtained:

$$b_{sn} = \frac{1}{\sin(\omega t)}\left(A\omega\sin(\omega t) - D\omega\cos(\omega t) - f\bar{u}_{sn} + f\bar{u}_g\right). \tag{6.12}$$

The solutions obtained for $\bar{u}_{sn}$ and b_{sn} are not periodic as in the particular case studied by Shapiro and Fedorovich (2009). Imposing the initial conditions $v = v_0$, $u = u_0$, $b = b_0$, the parameters are determined: $A = \bar{v}_0 - \frac{f^2 \bar{v}_g}{\omega^2}$, $D = \frac{1}{\omega}\left[-b_0 sin(\alpha) + f\left(\bar{u}_g - \bar{u}_0\right)\right]$, $C = \bar{u}_0 + \frac{f}{\omega^2}\left[-b_0 sin(\alpha) + f\left(\bar{u}_g - \bar{u}_0\right)\right]$.
The same derivation is repeated considering a valley from west to est (subscript we) as supposed by Shapiro and Fedorovich (2009). The difference from the original model remains the three-dimensionality and the assumption of a variable geostrophic wind with respect to the height. The SF with a slope oriented from west to east will be used in Sect. 6.2.4 to evaluate the improvement in the simulations derived by the rotation of the valley. The final results are:

$$\bar{u}_{we} = A\cos(\omega t) + D\sin(\omega t) + \frac{f^2 \bar{u}_g}{\omega^2} \tag{6.13}$$

$$\bar{v}_{we} = -\frac{Af}{\omega}\sin(\omega t) + \frac{Df}{\omega}\cos(\omega t) - \frac{f^3 \bar{u}_g t}{\omega^2} + f\bar{u}_g t + C \tag{6.14}$$

$$b_{we} = -\frac{1}{\sin(\omega t)}\left(-A\omega\sin(\omega t) + D\omega\cos(\omega t) - f\bar{v}_{we} + f\bar{v}_g\right), \tag{6.15}$$

with parameters $A = \bar{u}_0 - \frac{f^2 \bar{u}_g}{\omega^2}$, $D = \frac{1}{\omega}\left[-b_0 sin(\alpha) - f\left(\bar{v}_g - \bar{v}_0\right)\right]$,
$C = \bar{v}_0 - \frac{f}{\omega^2}\left[-b_0 sin(\alpha) - f\left(\bar{v}_g - \bar{v}_0\right)\right]$. In this case the not-periodic solutions are the ones obtained for $\bar{v}_{we}$ and b_{we}.

6.2.2 IOP4 Simulation

The IOP4 is simulated using the SF considering a valley oriented from south to north. The results are compared to the ones obtained with the VdW. The slope α, the Brunt-Väisälä frequency N and the initial buoyancy b_0 need to be evaluated to use the SF. $\alpha = 0.064°$ is the slope angle measured between Sagebrush and the other flux tower T1, along the orientation of the valley. b_0 is evaluated considering the last convective profile before the sunset (0014 UTC, Fig. 6.8a) to consider the effects of the afternoon heating in the model (Shapiro and Fedorovich, 2009). b_0 is defined as

$$b_0 = g\frac{\theta_0 - \theta_{e0}}{\theta_{r0}}. \tag{6.16}$$

The initial environmental potential temperature θ_{e0} is assumed equal to the average potential temperature detected in the range 395 m $\leq z \leq$ 400 m. This range is chosen because consists of the higher levels measured by the tethered balloon. The initial reference potential temperature θ_{r0} is evaluated considering the average potential temperature detected in the first 5 m above the surface. Since the potential temperature decreases in the first few tens metres above the surface and then it tends to be equal at θ_{e0} (Fig. 6.8a), the initial potential temperature θ_0 is evaluated considering the average potential temperature in the range 0 m $< z \leq$ 50 m. Using Eq. (6.16), b_{0-IOP4}=0.003 ms^{-2} is

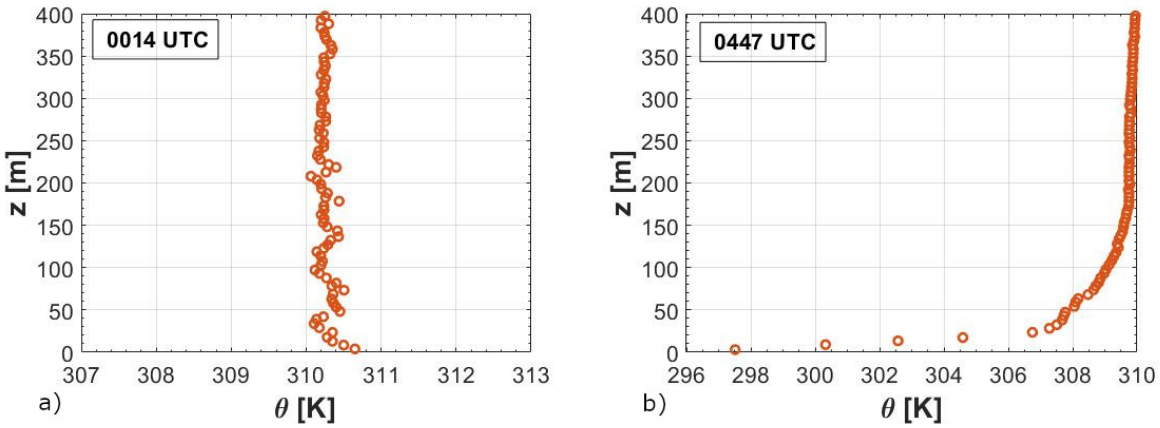

Figure 6.8: Last convective potential-temperature profile (a) and initial potential-temperature profile (b) measured by tethered balloon during the IOP4.

obtained. N, defined by

$$N = \sqrt{\frac{g}{\theta_r}\frac{\mathrm{d}\theta_e}{\mathrm{d}z}}. \tag{6.17}$$

is evaluated considering the initial potential-temperature profile (Fig. 6.8b) because N gives information on the nocturnal stability. The reference potential temperature θ_r is evaluated in the same way of θ_{r0} used in Eq. 6.16, while the gradient of the environmental potential temperature θ_e with respect to the height is assumed equal to the variation of the potential temperature in the range 395 m $\leq z \leq$ 400 m. Using Eq. (6.17), $N = 0.02$ s^{-1} is obtained. Figure 6.9 shows the simulation of the IOP4 obtained through the SF and starting from the sunset. Since the solution of the wind speed components (Eqs. 6.10, 6.11) are not periodic considering the general SF currently analysed, the inertial-gravity period cannot be computed as in the particular case analysed by Shapiro and Fedorovich (2009) (Eq. (2.64)). The simulated LLJ wind-speed maximum still grows during all the simulation (Fig. 6.9). As the VdW, the current one cannot capture the growth of the LLJ depth and the increase of the wind-speed maximum height during the night. The SF predicts the maximum at 40 m, which is 5 m or 10 m higher than the maximum obtained by the VdW. Fig. 6.10 shows the wind-speed difference ΔU (ms^{-1}) between the VdW and the current model. The VdW predicts larger wind speed in all the profiles. ΔU grows with respect to time reaching 2.7 ms^{-1} at 20 m at the end of the simulation. The larger difference are around the predicted wind-speed maxima by the two models. Despite $\Delta U > 1.0$ ms^{-1} in the range 10 m $\leq z \leq$ 50 m, the general shape of the simulated LLJ is similar compering the two models. The main causes that contribute to ΔU in the first 50 m above the surface can be related to the differences in the prediction of the wind-speed maximum height and in the shape of the nose due to the different profiles used as equilibrium. Figure 6.11 shows the comparison between each simulated profile and the measured one. The initial development of the LLJ formation is not well simulated also

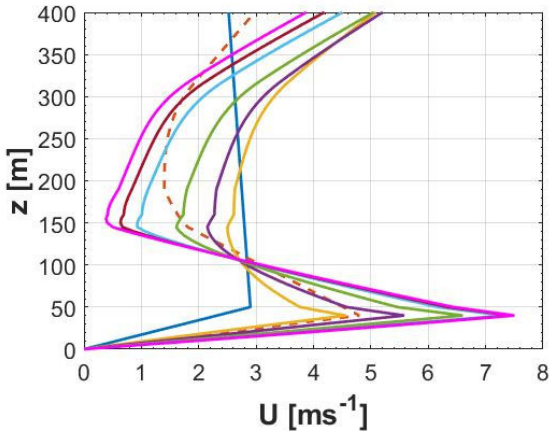

Figure 6.9: Simulations of the IOP4 through the SF considering a slope oriented from south to north. The solid blue line is the initial profile, the dash orange line is the equilibrium profile. The simulation is computed at 0659 UTC (yellow), 0806 UTC (purple), 0931 UTC (green), 1104 UTC (light-blue), 1142 UTC (red), 1216 UTC (pink).

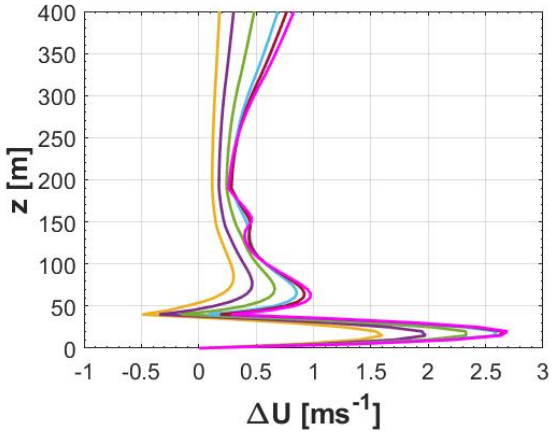

Figure 6.10: The wind-speed difference $\Delta U = U_{VdW} - U_{SF}$ for the IOP4, in which U_{VdW} is the wind-speed profile simulated through the VdW and U_{SF} is the one simulated through the SF considering a slope oriented from south to north. The simulations are computed at 0659 UTC (yellow), 0806 UTC (purple), 0931 UTC (green), 1104 UTC (light-blue), 1142 UTC (red), 1216 UTC (pink).

using the SF because it underestimates the growth of the LLJ during this initial phase and it predicts a wider LLJ (Fig. 6.11a). The wind-speed maximum is underestimates by 1.0 ms^{-1} which is 0.5 ms^{-1} less than the underestimation obtained with the VdW. The agreement between the simulated and the measured LLJ improves when the LLJ grows (Fig. 6.11b), especially in terms of intensity of the wind-speed maximum. This maximum is underestimated by 0.6 ms^{-1} in Fig. 6.11b. Since the model only contains the

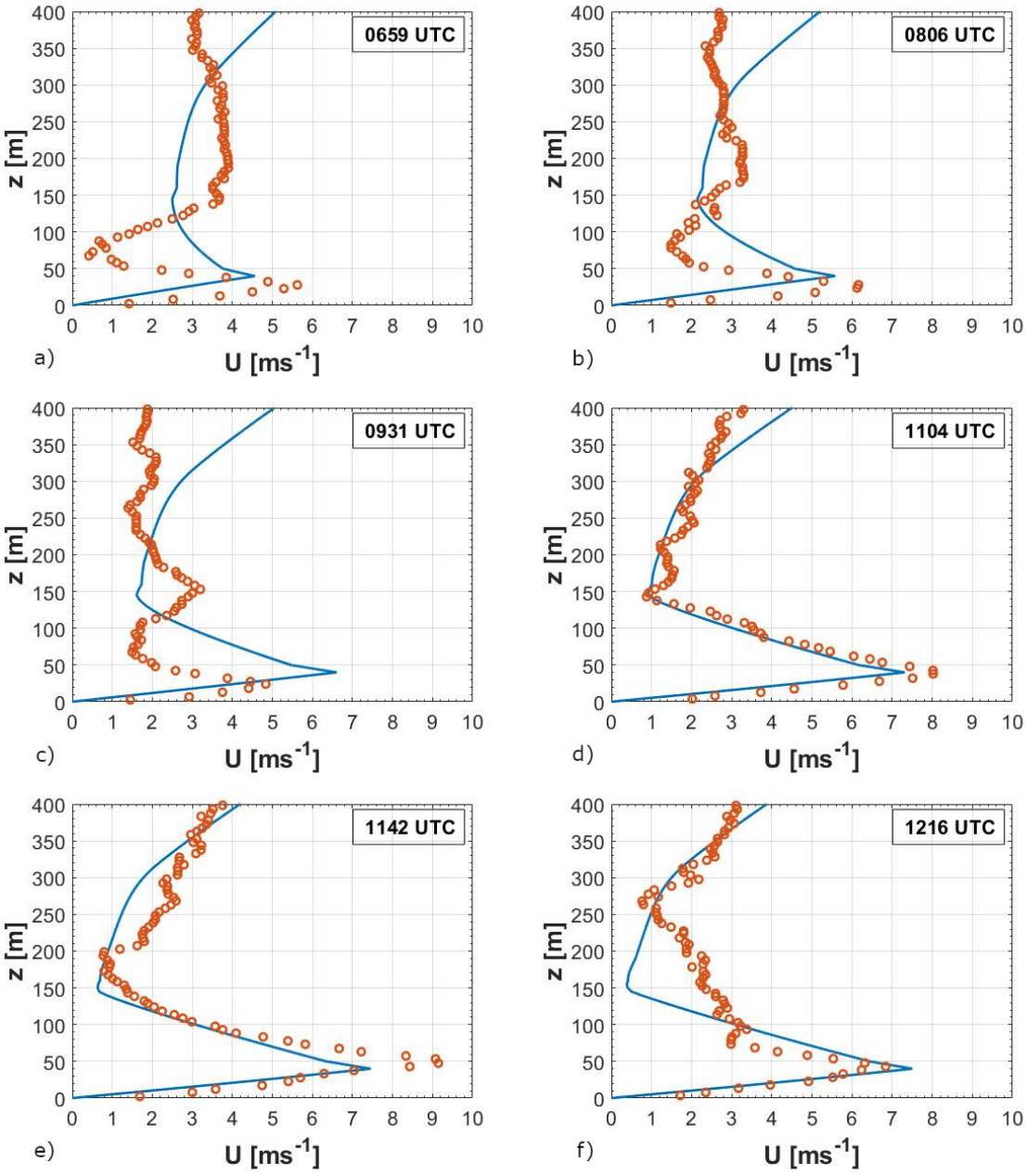

Figure 6.11: Comparison between the simulated (solid blue line) and the measured (dot-marked orange line) tethered-balloon profiles for the IOP4 through the SF considering a slope oriented from south to north.

inertial-oscillation dynamics over a sloped terrain, the double-nose LLJ formation is not predicted (Fig. 6.11c). Despite the maximum is underestimated by 0.7 ms^{-1}, which is 0.2 ms^{-1} more than the underestimation retrieved by the VdW, the general structure of the

LLJ is well simulated when the secondary nose is dissipated (Fig. 6.11d). As the VdW, the current one cannot simulate the large variations of the wind-speed maximum retrieved in the following LLJ profiles (Fig. 6.11e,f). However, the general shape of these LLJs is well predicted. Therefore, the SF predicts LLJ maximum larger than the VdW during the initial formation, partially compensating the underestimation compered to the measured profiles. Despite the general shape of the fully-developed profiles is well simulated, the current SF maintains the same problems observed simulating the spring quiescent IOPs using the VdW as it does not capture the growth of the LLJ depth. Therefore, using this sloped-terrain model does not considerably improve the simulation over the analysed complex terrain.

6.2.3 IOP7 Simulation

The parameters used in the simulation of the IOP7 are evaluated as for the IOP4 (Sect. 6.2.2). $\alpha = 0.064°$ is chosen to the IOP4 case, while b_{0-IOP7}=0.02 ms^{-2} and $N_{IOP7} = 0.3$ s^{-1}. b_{0-IOP7} is obtained from the last convective potential-temperature profile (0055 UTC, Fig. 6.12a), while N_{IOP7} is evaluated considering the initial potential-temperature profile (0342 UTC, Fig. 6.12b). Figure 6.13 shows the simulation of the IOP7 obtained through the SF, starting from the sunset. As the simulation obtained using the VdW, the

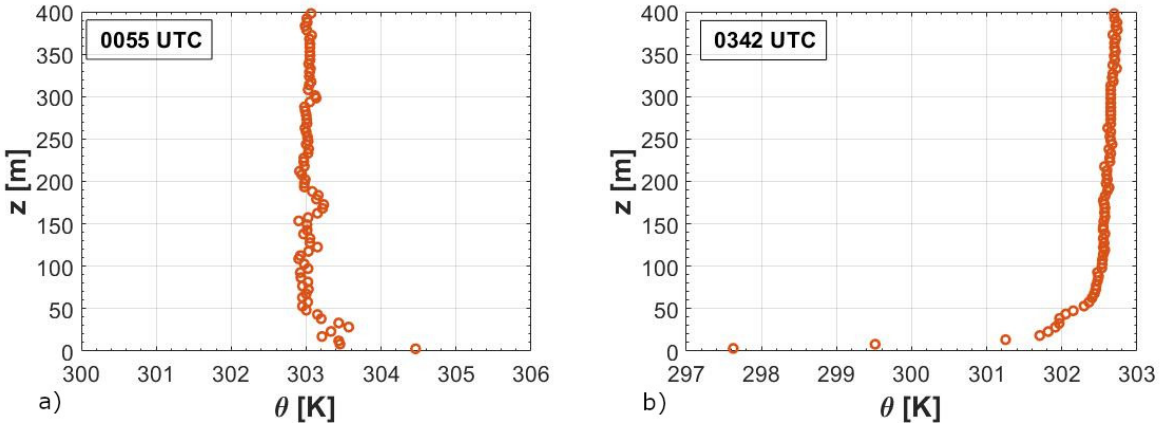

Figure 6.12: Last convective potential-temperature profile (a) and initial potential-temperature profile (b) measured by tethered balloon during the IOP7.

simulated wind-speed maximum decreases in the last profile (1203 UTC, pink line, Fig. 6.13) compered to the previous one (1120 UTC, red line, Fig. 6.13). The maximum is always predicted at 70 m, therefore the model cannot reproduce the increase of the wind-speed maximum height and the growth of the LLJ depth. The predicted height is in the range obtained using the VdW. Figure 6.14 shows the difference ΔU between the VdW and the SF. Also during the IOP7, the VdW predicts larger wind speed, with maximum difference of 2.1 ms^{-1} at 30 m. $\Delta U > 1.0$ ms^{-1} is retrieved between 0 m $<$ z $\leq$ 50 m,

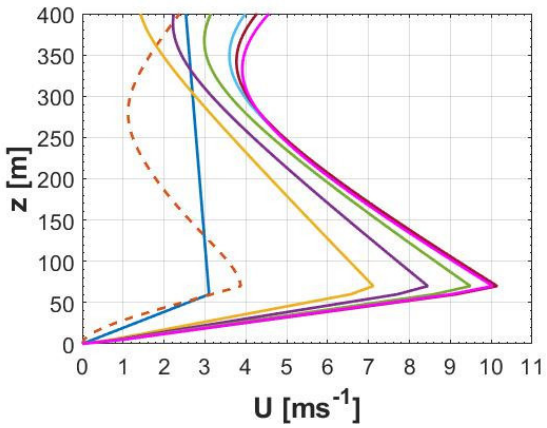

Figure 6.13: Simulations of the IOP7 through the SF considering a slope oriented from south to north. The solid blue line is the initial profile, the dash orange line the equilibrium profile. The simulation is computed at 0650 UTC (yellow), 0803 UTC (purple), 0921 UTC (green), 1048 UTC (light-blue), 1120 UTC (red), 1203 UTC (pink).

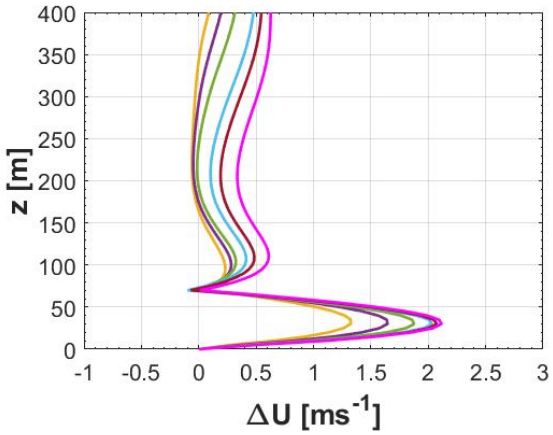

Figure 6.14: The wind-speed difference $\Delta U = U_{VdW} - U_{SF}$ for the IOP7, in which U_{VdW} is the wind-speed profile simulated through the VdW and U_{SF} is the one simulated through the SF considering a slope oriented from south to north. The simulations are computed at 0650 UTC (yellow), 0803 UTC (purple), 0921 UTC (green), 1048 UTC (light-blue), 1120 UTC (red), 1203 UTC (pink).

therefore at lower heights than the wind-speed maximum height. ΔU is approximately null at the wind-speed maximum height predicted by the current model. The discrepancy at the lower heights highlighted by ΔU can depend on the direct use of the geostrophic profile as equilibrium one in the SF.
Figure 6.15 shows the comparison between the simulated profiles and the measured ones. Despite ΔU is not negligible, the general shape and the wind-speed maximum are also well predicted by the SF considering a slope oriented from south to north. Analogously

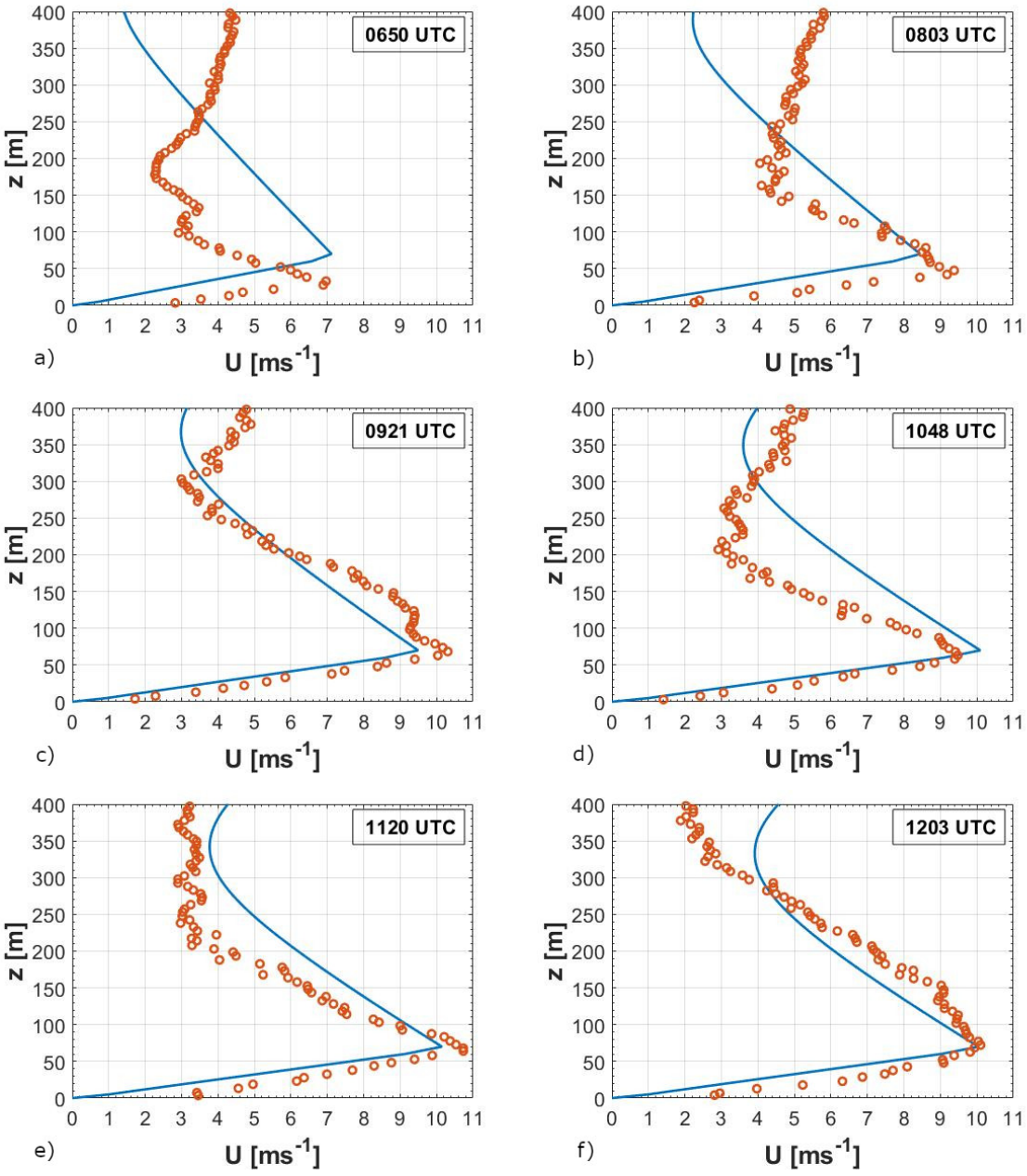

Figure 6.15: Comparison between the simulated (solid blue line) and the measured (dot-marked orange line) tethered-balloon profiles for the IOP7 through the SF considering a slope oriented from south to north.

to the other simulations retrieved by both the analysed models, the SF cannot capture the initial development of the LLJ (Fig. 6.15a). However, the maximum is equal to the VdW and it is underestimated only by 0.2 ms^{-1} with respect to the measured profile.

The prediction of the general shape gives good results considering the profiles in Fig. 6.15b,c. The maxima retrieved by SF differs by 0.1 ms^{-1} from the one obtained by VdW. Analogously to the VdW, the SF cannot simulate the subsequent changes in the width of the measured LLJ limiting the prediction of the general shape (Fig. 6.15d,e). The maximum is overestimated by 0.5 ms^{-1} in Fig.6.15d and underestimated by 0.6 ms^{-1} in Fig. 6.15e, as in the simulation retrieved by the VdW. Another similarity is the well simulation of the fully-developed LLJ both in therms of width and wind-speed maximum (Fig. 6.15f). Despite the difference highlighted through ΔU, the evolution of the wind-speed maximum predicted by the two models is equal. The agreement between the two models is better compared to the simulations of the IOP4, confirming that the information over the sloped terrain does not considerably improve the simulation of the analysed LLJs in complex terrain.

6.2.4 Comparison with the East-West Oriented Slope

A sensitivity investigation is here proposed to address the possible differences in the SF simulations considering a west to east oriented slope instead of a south to north one (Fig. 6.16) using the same initial and geostrophic profiles and assuming the same values for the parameters. Considering the south to north case, the simulations should improve

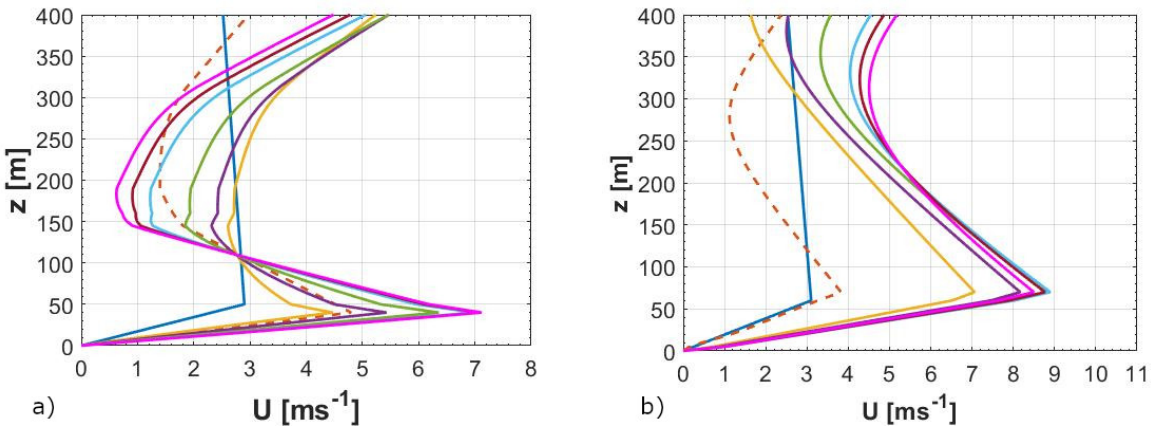

Figure 6.16: Simulations through the SF considering a slope oriented from west to east. (a) shows the IOP4 and (b) the IOP7. The solid blue line is the initial profile, the dash orange line the equilibrium profile. In (a) the simulation is computed at 0659 UTC (yellow), 0806 UTC (purple), 0931 UTC (green), 1104 UTC (light-blue), 1142 UTC (red), 1216 UTC (pink). In (b) the simulation is computed at 0650 UTC (yellow), 0803 UTC (purple), 0921 UTC (green), 1048 UTC (light-blue), 1120 UTC (red), 1203 UTC (pink).

than the west to east case because the difference in orientation compered to the Dugway Valley (which is from south-east to north-west) decreases from 135° to 45°. Compering the simulations obtained by the two cases, the wind-speed maximum height is the same

both in the IOP4 and IOP7. In the west to east case, the LLJ grows during all the current simulation considering the IOP4, while the larger wind speed is retrieved at 1048 UTC simulating the IOP7. Considering the south to north case, the LLJ grows until the profile simulated at 1120 UTC during the IOP7, therefore the time in which the larger wind speed is retrieved depends on the orientation of the slope. Figure 6.17 shows the difference ΔU between the south to north case and the west to east one. Considering the IOP4, the difference grows over time. $\Delta U > 0$ ms^{-1} is obtained between 0 m < z < 70 m, while $\Delta U < 0$ ms^{-1} is retrieved above. The wind-speed maximum height is the one in

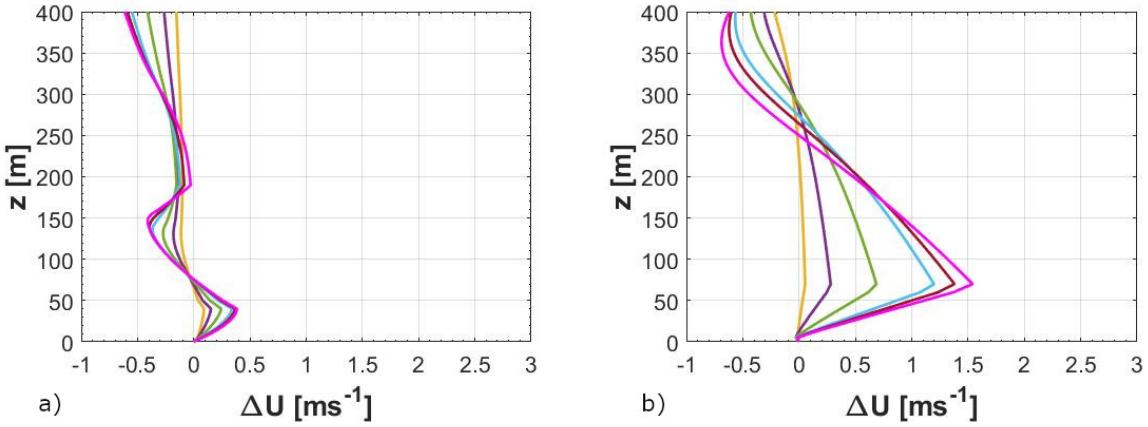

Figure 6.17: The wind-speed difference $\Delta U = U_{SFsn} - U_{SFwe}$ for the IOP4, in which U_{SFsn} is the wind-speed profile simulated through the SF considering a slope oriented from south to north and U_{SFwe} is the one simulated through the SF considering a slope oriented from west to east. In (a) the simulation is computed at 0659 UTC (yellow), 0806 UTC (purple), 0931 UTC (green), 1104 UTC (light-blue), 1142 UTC (red), 1216 UTC (pink). In (b) the simulation is computed at 0650 UTC (yellow), 0803 UTC (purple), 0921 UTC (green), 1048 UTC (light-blue), 1120 UTC (red), 1203 UTC (pink).

which the maximum of ΔU is retrieved. This maximum is 0.4 ms^{-1} when the LLJ is fully developed. The difference also grows over time during the IOP7. $\Delta U > 0$ ms^{-1} is obtained between 0 m and a variable height ranging from 225 m to 290 m, while $\Delta U < 0$ ms^{-1} is retrieved above. Also during the IOP7, the wind-speed maximum height is the height in which the maximum of ΔU is located. However ΔU is more accentuated at this height compered to the IOP4, indeed it is equal to 1.5 ms^{-1} when the LLJ is fully developed. In conclusion, the results obtained with the SF are dependent on the considered orientation of the slope. As expected, the simulation is improved considering the south to north case, because the west to east one is characterised by a larger underestimation of the wind-speed maximum.

6.3 Hodographs Simulation Using the Two Models

The hodograph is a diagram in the plane of the horizontal wind-speed components (u,v), useful to visualised the changes of the wind vector. Figure 6.18 shows the hodographs measured during the night of the IOP4 and simulated through the VdW and the SF considering a slope oriented from north to south. Analogously, Fig. 6.19 shows the hodographs at the same heights for the IOP7. They are simulated from sunset to sunrise at the elevation

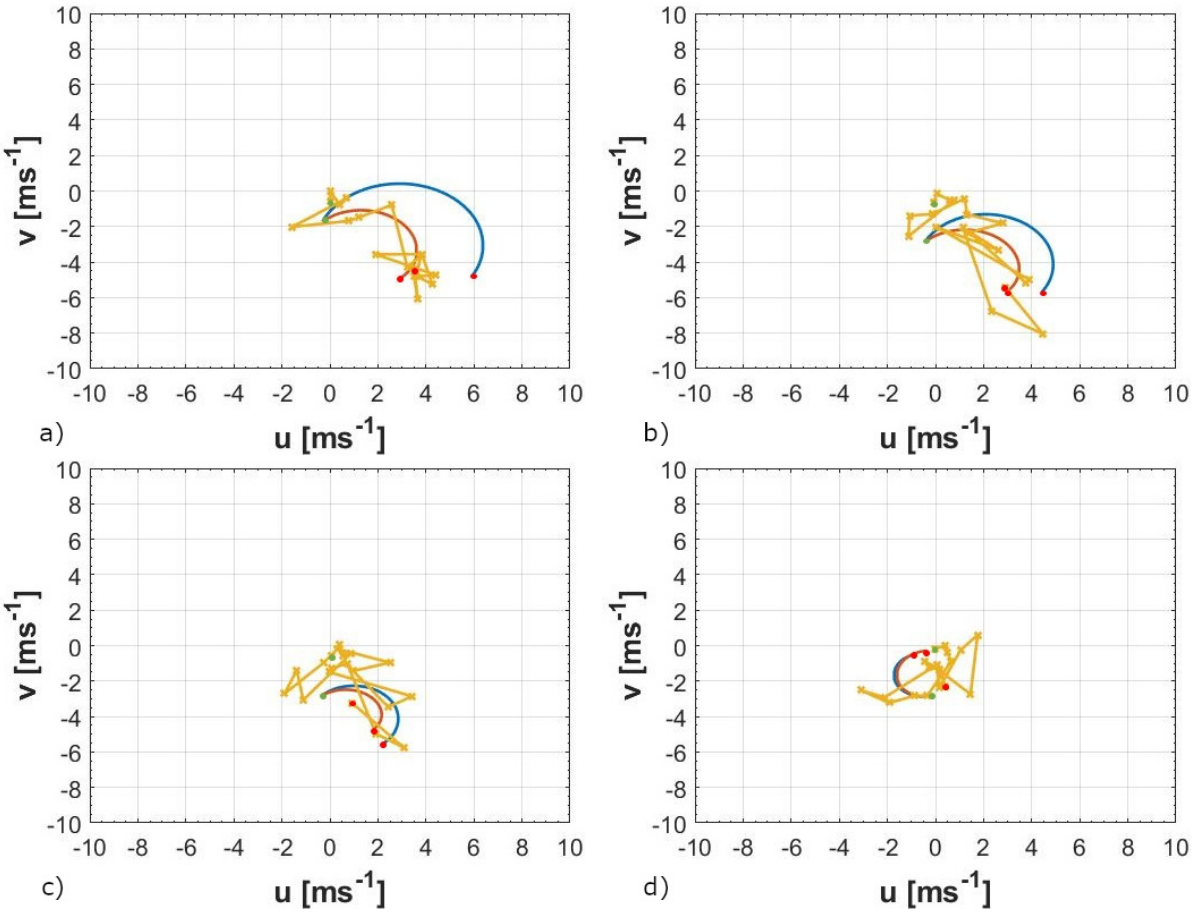

Figure 6.18: Comparison between the hodographs measured during the IOP4 (yellow lines) and simulated through the VdW (blue lines) and the SF considering a slope oriented from south to north (orange line). (a) shows the hodographs at 30 m, (b) at 50 m, (c) at 70 m, (d) at 150 m. The green dots indicate the beginning of each hodograph, the red dots the end of each one.

of 30 m, 50 m, 70 m, 150 m. 50 m and 70 m are chosen because the wind-speed maximum is approximately at these heights when the LLJ is fully developed respectively during the IOP4 and during the IOP7. Considering the LLJ increases in depth during the night, 30 m is chosen to evaluate the hodographs at a smaller height in which the maximum is

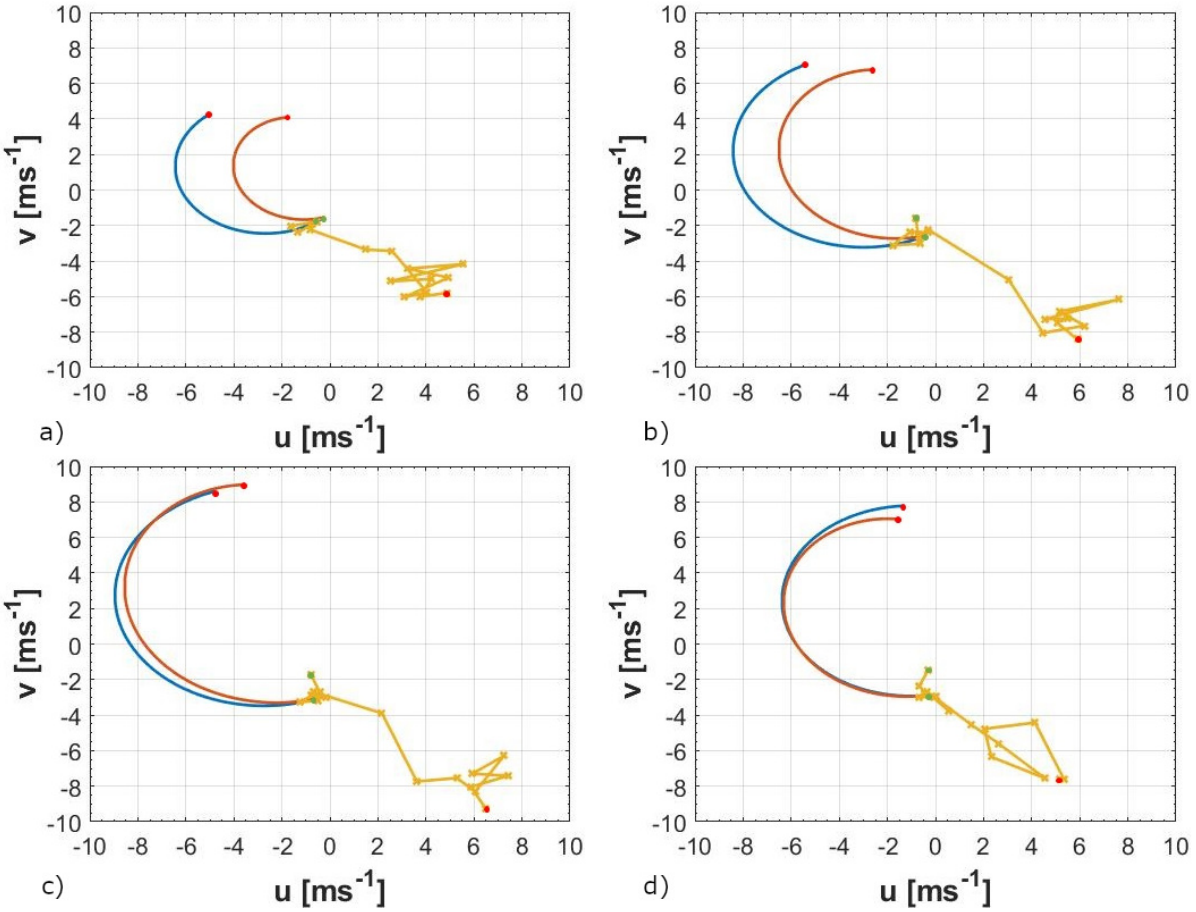

Figure 6.19: Comparison between the hodographs measured during the IOP7 (yellow lines) and simulated through the VdW (blue lines) and the SF considering the slope oriented from south to north (orange line). (a) shows the hodographs at 30 m, (b) at 50 m, (c) at 70 m, (d) at 150 m. The green dots indicate the beginning of each hodograph, the red dots the end of each one.

located when the LLJ is still not fully developed. 150 m is chosen because is the height in which the secondary maximum is located in the double-nose LLJ profile measured at 0931 UTC during the IOP4 (the IOP4$_a$ case). The VdW produces circular hodographs around the equilibrium-wind profile with radius equal to the vectorial difference between the equilibrium wind vector and the initial one. The particular case analysed by Shapiro and Fedorovich (2009) in which $\bar{U}_g = (\bar{u}_g = 0, \bar{v}_g > 0)$ produces elliptical hodographs, where the eccentricity is not dependent on the initial and the equilibrium conditions. Considering the general case used in the current analysis, the SF is characterised by a periodic solution for the horizontal wind-speed component v and a non-periodic one for the other horizontal component u (Eqs. (6.10), (6.11)). Therefore, the hodographs simulated with this model have not a closed shape as the ellipses obtained in the particular

case analysed by Shapiro and Fedorovich (2009).
During the IOP4, the more the considered height is, the lower the regularity of the measured hodographs will be. As expected in the North Hemisphere, the clockwise rotation is observed at each eight except at 150 m in which the measured hodograph has a more irregular form (Fig. 6.18d). This structure could depend on the perturbations that dominates over the inertial-oscillations dynamics modifying the usual form of the hodograph. The hodograph at 30 m is well simulated by the SF (Fig. 6.18a), which also gives good results at 50 m (Fig. 6.18b). The simulation obtained using the VdW are worst. The approximations concerning the turbulence, the buoyancy and the geometry of the valley in both the models could have caused this difference in the prediction of the hodographs. Despite the hodograph measured at 70 m is more irregular than the one measured at the lower heights, both the models capture the general structure (Fig. 6.18c). The measured hodographs are more regular during the IOP7, in which the shape is similar between each height. They are linear or as a clockwise curve characterised by a large eccentricity. The measured hodophaph at 30 m is very similar to the one retrieved during the IOP4. This can be connected to the similarity between the stratification retrieved during the two IOPs ($N_{IOP4} \approx N_{IOP7}$). The results obtained simulating the IOP7 do not capture the evolution of the wind vector at any height (Fig. 6.19). This failure is probably caused by the choice of the equilibrium wind profile. Since any radiosonde was launched in the night of the IOP7, this profile was built considering the one used during the IOP4. Despite the wind speed are well captured (Sects. 6.1.2, 6.2.3), the wind direction may not, determining an error in the horizontal wind-speed components u and v. Therefore, the simulation of the hodograph for the IOP7 case is conditioned by the lack of radiosonde data, useful to extrapolate the equilibrium-wind profile.

Summary

The objective of the current chapter was to verify if the evolution of the downvalley LLJs retrieved during the MATERHORN Program is in agreement with the inertial-oscillations dynamics. To achieve this objective, the spring quiescent IOPs were simulated using a flat-terrain model as the one proposed by Van de Wiel et al. (2010) (addressed as VdW) and a sloped-terrain model as the one proposed by Shapiro and Fedorovich (2009) (addressed as SF). This latter model was extended to the three-dimensional case and considering a general geostrophic-wind vector. Furthermore, the slope considered in the SF was rotated from the west to east case proposed in the original model by Shapiro and Fedorovich (2009) to the south to north case to better simulate the orientation of the Dugway Valley. The improvement given by the rotation was confirmed comparing the results obtained by the two cases. The VdW and the SF cannot capture the growth of the LLJ depth and the resulting increase of the wind-speed maximum height. Despite the initial development of the LLJ is underestimated by both the models, the fully-developed LLJ is well simulated verifying that the LLJs detected during the MATERHORN field campaigns were driven by inertial oscillations. When the analysed LLJs retrieved in complex terrain over

a gently sloped terrain are fully developed, the general shape of the measured profiles and the magnitude of the wind-speed maximum are captured by both the models. The improvement given by the application of a sloped-terrain model, as the SF, was obtained simulating the hodographs. The general shape of the hodographs measured at the two lowest heights (30 m and 50 m) is well simulated by the SF. The simulation is worst using the VdW. Both the models fail to simulate the measured hodographs at the highest heights (70 m and 150 m) because these hodographs are less regular than the ones retrieved at the lowest heights. This less regular shape could depend on the occurrence of more perturbations at the highest heights, which dominates on the inertial-oscillations dynamics. The different prediction of the hodograph through the VdW and the SF could have been caused by the approximations concerning the turbulence, the buoyancy and the geometry of the valley in both the models. During the IOP7, the measured hodographs are less perturbed and more regular. At each considered height, the shape is linear or as a curve characterised by a large eccentricity. Both the VdW and the SF fails to simulate the hodographs measured during the IOP7. The reason of this failure could be due to the choice of the equilibrium profile used to simulate the IOP7, which is conditioned by a lack of radiosonde launch during the night of the IOP7.

Chapter 7

Conclusions

The main objectives of this thesis were 1) to define new criteria for the identification of both LLJs and multiple LLJs, and then used them 2) to identify and analyse in-depth the driving mechanisms responsible for the formation of double-nose LLJs. Furthermore, 3) the temporal evolution of the analysed LLJs were investigated by means of two models retrieved from the literature, according to which nocturnal inertial oscillations are conducive of a LLJ and may influence its strength and dynamics. The analysed LLJs and double-nose LLJs were observed within the Dugway Valley (Utah) during the MATERHORN field campaigns. Only the data collected during quiescent intensive observing periods (IOPs) were selected for the present study, in order to role out the hypothesis of a synoptically driven (or significantly altered) mountain/valley circulation. The analyses focused on the identification and characterisation of downvalley LLJs driven by inertial oscillations, as observed within a stable nocturnal boundary layer. Due to the complexity of the terrain, the downvalley LLJ was found to be occasionally perturbed by lateral flows, as channelling currents or katabatic fronts. These perturbations can interfere with the growth of the downvalley LLJ during the night, by temporarily modifying the LLJ shape and generating unusual behaviours such as the formation of a double-nose LLJ.
In the first part of this work, an extensive literature review of methods and criteria for the identification of LLJ and multiple LLJs was carried out. Existing criteria were tested against MATERHORN data and further refined to better capture the observed LLJ characteristics. The analysis resulted in a new criterion which allows for the detection of both wind-speed maxima and minima along a profile, by means of comparison with arbitrary thresholds. Specifically, the criterion on the wind-speed maxima (Eq. (4.3)) was formulated adapting the criteria proposed in previous studies by Banta et al. (2002) and by Baas et al. (2009) accounting for the complexity of the analysed domain and the high instrumental resolution. An identification criterion for the wind-speed minima (Eq. (4.4)) was also proposed to better detail the complex shape of the multiple LLJs, starting from the criterion suggested by Baas et al. (2009). Furthermore, new variables as nose width (Eq. (4.6)) and symmetry ratio (Eq. (4.7)) were defined to better characterise the LLJs and multiple LLJs shape in terms of width and symmetry. Through the newly-defined LLJ identification criterion, 18 nocturnal double-nose LLJs profiles were identified and

classified on the basis of the two driving mechanisms theorised in the second part of this thesis. The first one is the wind-driven mechanism, which identifies double-nose LLJs as driven by two air masses flowing in different directions within two consecutive atmospheric layers. This first mechanism was found to be the most commonly observed in the dataset used in this thesis (13 out of 18 double-nose LLJs identified by the criteria). The second mechanism is the wave-driven one, in which the formation of the secondary nose relies on the vertical transport of momentum from the primary nose caused by the propagation of an inertial-gravity wave originated from a horizontal flow perturbation occurred at the surface. This perturbation was identified as a katabatic front, which brakes the downvalley LLJ dynamics inducing a damp of the wind speed and a tilt of the direction in the surface layer. Consequently, an inertial-gravity wave is generated and mean momentum is carried upwards by this wave, causing the formation of a secondary nose. The verification of this newly-introduced wave-driven mechanism was done by means of measurements from the MINISAMS network, which describe a katabatic front descending the western slopes and intruding the valley. The momentum transport attributed to an inertial-gravity wave was corroborated by the agreement between this thesis findings and results obtained by an observative bulk estimation (Eq. (4.9)) as well as by the wave momentum transport evaluation proposed by Kim and Mahrt (1992) (Eq. (2.17)).
The last part of this thesis is devoted at verifying if the evolution of the downvalley LLJ in Dugway Valley follows the inertial-oscillations dynamics by means of simple models proposed in literature. This hypothesis was tested for two different quiescent IOPs (spring IOP4 and IOP7) using the flat-terrain model proposed by Van de Wiel et al. (2010) as well as the sloped-terrain one proposed by Shapiro and Fedorovich (2009), the latter being modified to better account for the features of the Dugway Valley. Despite the analysed data are representative of complex terrain characterised by a gentle slope, both model was able to satisfactorily reproduce the LLJ wind-speed maximum and the LLJ shape only during those time intervals corresponding to a fully-developed LLJ. Results provided by the two models were similar, although the application of the sloped-terrain model proposed by Shapiro and Fedorovich (2009) provided some improvement in the simulation of the hodographs retrieved in the range $0\ \text{m} < z \leq 50\ \text{m}$ during the IOP4.
In conclusion, the newly-proposed criteria have allowed to identify the nocturnal double-nose LLJs, which were classified on the basis of the newly-introduced mechanisms that drive their formation. In this two mechanisms, which are the wind-driven and the wave-driven ones, the double-nose LLJs are originated by perturbations that temporarily modify the already established downvalley LLJ. Except for this transitory perturbations, the evolution of the downvalley LLJ was found to follow the inertial-oscillations dynamics. No significant differences were observed between the representation of the LLJs driven by inertial oscillations in flat terrain and in a valley characterised by gently sloped terrain.

Appendix A

The Atmospheric Scale

Figure A.1 reports the several atmospheric-scale definitions adapted after Thunis and Bornstein (1996) and the relative atmospheric phenomena. The atmospheric scale is the

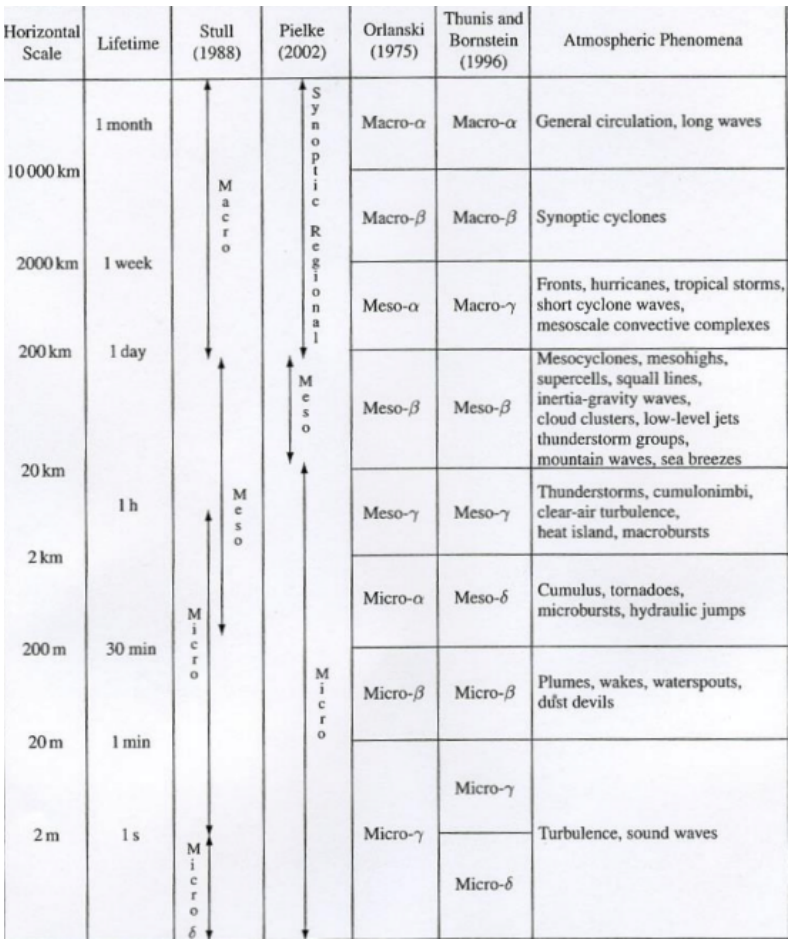

Figure A.1: Atmospheric scale definition (Adapted after Thunis and Bornstein (1996))

characteristic horizontal scale of the atmospheric phenomena. The Micro-scales are typical of the turbulence phenomena, the Meso-scales characterised the mesoscale ones and the Macro-scales the synoptic ones.

Appendix B

Ekman Solutions

The Ekman solutions are particular solutions of the Navier-Stokes equations considering the following approximations: the pressure gradients are substituted through the geostrophic equations

$$\frac{\partial \bar{P}}{\partial x} = f\rho\,\bar{v}_g \tag{B.1}$$

$$\frac{\partial \bar{P}}{\partial y} = -f\rho\,\bar{u}_g, \tag{B.2}$$

and the turbulent fluxes are parameterised through flux-gradient relationships in analogy to the molecular diffusion, i.e.

$$\frac{\partial \overline{u'w'}}{\partial z} = -K_m \frac{\partial^2 \bar{u}}{\partial z^2} \tag{B.3}$$

$$\frac{\partial \overline{v'w'}}{\partial z} = -K_m \frac{\partial^2 \bar{v}}{\partial z^2}. \tag{B.4}$$

Considering the steady state case, the Ekman balance is obtained:

$$-f\bar{v} + f\bar{v}_g - K_m \frac{\partial^2 \bar{u}}{\partial z^2} = 0 \tag{B.5}$$

$$f\bar{u} - f\bar{u}_g - K_m \frac{\partial^2 \bar{v}}{\partial z^2} = 0, \tag{B.6}$$

where the eddy viscosity K_m and the Coriolis parameter f are assumed as constant. Multiplying Eq. (B.5) for the complex number i and subtracting it to Eq. (B.6), the following equation is obtained:

$$if\bar{v} - if\bar{v}_g + iK_m \frac{\partial^2 \bar{u}}{\partial z^2} + f\bar{u} - f\bar{u}_g - K_m \frac{\partial^2 \bar{v}}{\partial z^2} = 0. \tag{B.7}$$

A complex velocity $\bar{\omega}$ and a geostrophic complex velocity $\bar{\omega}_g$ are defined as:

$$\bar{\omega} = \bar{u} + i\bar{v} \tag{B.8}$$

$$\bar{\omega}_g = \bar{u}_g + i\bar{v}_g. \tag{B.9}$$

Using these velocities, Eq. (B.7) can be rewritten as

$$-\frac{if}{K_m}\bar{\omega} + \frac{if}{K_m}f\bar{\omega}_g + \frac{\partial^2\bar{\omega}}{\partial z^2} = 0. \tag{B.10}$$

To find the particular solution, $\bar{\omega}$ is assumed to be independent on z, so that

$$-\frac{if}{K_m}\bar{\omega} = -\frac{if}{K_m}f\bar{\omega}_g. \tag{B.11}$$

Thus the particular solution is $\bar{\omega} = \bar{\omega}_g$.
Then the associated homogeneous equation is considered:

$$+\frac{\partial^2\bar{\omega}}{\partial z^2} - \frac{if}{K_m}\bar{\omega} = 0. \tag{B.12}$$

A solution of the form $\bar{\omega} = A\exp^{\lambda z}$ is assumed, in which $\lambda^2 = \frac{if}{K_m}$. Defining $\gamma = \sqrt{\frac{f}{2K_m}}$ the two possible values of λ are obtained: $\lambda_+ = (1+i)\,\gamma$ and $\lambda_- = (-1-i)\,\gamma$.
Thus the general solution is

$$\bar{\omega} = Ae^{\lambda_+ z} + Be^{\lambda_- z} = Ae^{\gamma z}e^{i\gamma z} + Be^{-\gamma z}e^{-i\gamma z}. \tag{B.13}$$

The initial conditions $\bar{\omega} = 0$ at $z = 0$ and $\bar{\omega} \to \bar{\omega}_g$ at $z \to \infty$ are assumed and the term $Ae^{\gamma z}e^{i\gamma z}$ that grows exponentially is rejected. Therefore, the complete solution is

$$\bar{\omega} = \bar{\omega}_g + Be^{-\gamma z}e^{-i\gamma z}. \tag{B.14}$$

Imposing the condition at $z = 0$, $B = -\bar{\omega}_g$ is found and Eq. B.14 becomes

$$\bar{\omega} = \bar{\omega}_g[1 - e^{-\gamma z}e^{-i\gamma z}]. \tag{B.15}$$

Expanding the real and the imaginary parts the following equation is obtained:

$$\bar{u} + i\bar{v} = (\bar{u}_g + i\bar{v}_g)\,[1 - e^{-\gamma z}cos(\gamma z) + ie^{-\gamma z}sin(\gamma z)]. \tag{B.16}$$

Assuming $\bar{v}_g = 0$ for simplicity, the following equations are obtained:

$$\bar{u}_{Ek} = \bar{u}_g[1 - e^{-\gamma z}cos(\gamma z)] \tag{B.17}$$
$$\bar{v}_{Ek} = \bar{u}_g[e^{-\gamma z}sin(\gamma z)], \tag{B.18}$$

which are the Ekman solutions.

Appendix C

Instrumental specifications

C.1 Young 81000

The sonic anemometers Young81000 (Fig. C.1) have been equipped on the T1 and T4 flux towers. They measure the wind vector components and the speed of sound considering the transit of ultrasonic acoustic signals and correcting for crosswind effects. The speed of sound is useful to derive the sonic temperature. The wind direction WD is obtained from the horizontal wind components as

$$WD = \arctan\left(-\frac{v}{u}\right) + a, \tag{C.1}$$

in which a is an offset to align the derived wind direction to the meteorological reference systems (Fig. C.2). Normally, a would be equal to 90°, however to compensate a wrong setting or instrumentation orientation, a different rotation was necessary to fit the meteorological reference systems. This new offset was verified to be $a = 270°$. The following list summarises the specifications for this instrumentation.

Figure C.1: Young Company 81100 sonic anemometer.

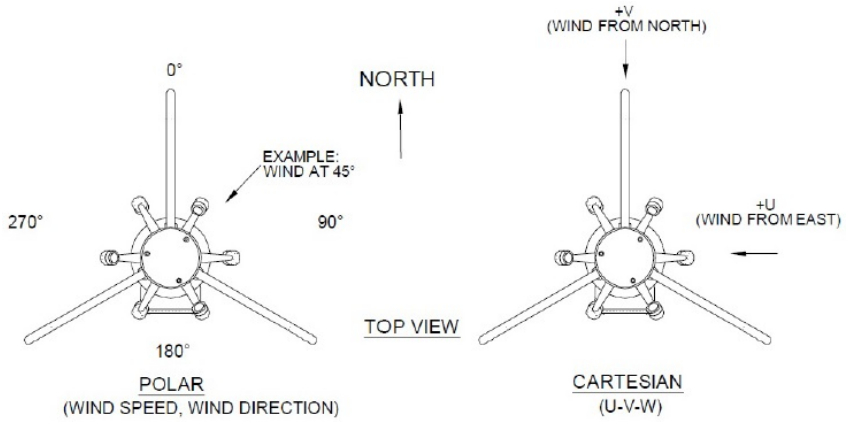

Figure C.2: Young Company 81100 reference system.

Wind speed
Range: 0 to 40 ms^{-1}.
Resolution: 0.01 ms^{-1}.
Threshold: 0.01 ms^{-1}.
Accuracy:
$\pm 1\%$ rms ± 0.05 ms^{-1} from 0 to 30 ms^{-1},
$\pm 3\%$ rms from 30 to 40 ms^{-1}.

Wind direction
Azimuth range: 0 to 360 °.
Elevation Range: ±60.0°.
Resolution: 0.1°.
Accuracy:
$\pm 2°$ from 0 to 30 ms^{-1},
$\pm 5°$ from 30 to 40 ms^{-1}.

Sonic temperature
Range: -50 to 50 °C.
Resolution: 0.01 °C.
Accuracy: ±2 °C from 0 to 30 ms^{-1}.

C.2 Campbell CSAT3

The sonic anemometers Campbell CSAT3 (Fig. C.3) were equipped the Sagebrush flux tower. They allow to measure three orthogonal wind components in the anemometer reference frame, which is arbitrary oriented. The speed of sound, necessary to retrieve the sonic temperature, is determined from three acoustic path and corrected for crosswind

effects. Eq. (C.1) is used to obtain the wind direction, however the offset a to adapt the measured directions to the meteorological reference system is arbitrary because it derives by the choice of the anemometer orientation. In the current study a is equal to 0° at all the levels except at 20 m in which it is 230°. The following list summarised the specifications for this instrumentation.

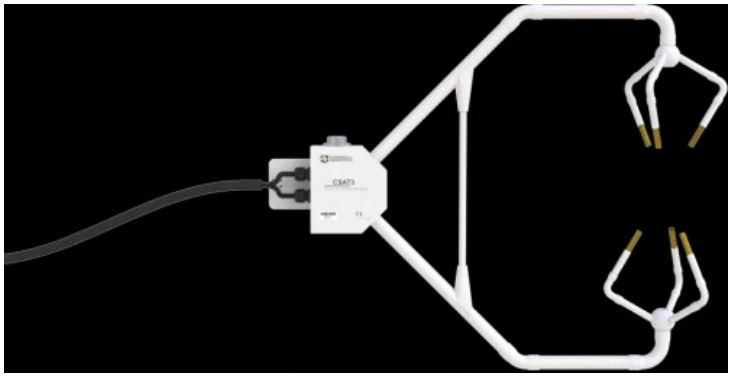

Figure C.3: Campbell Scientific CSAT3 sonic anemometer.

Wind speed
Range: ±30 to ±60 ms^{-1} for u and v, ±8 ms^{-1} for w.
Resolution: 0.001 ms^{-1} rms for u and v, 0.005 ms^{-1} rms for w.
Accuracy:
$<$ ±2% of reading for wind vectors within ±5° of horizontal,
$<$ ±3% of reading for wind vectors within ±10° of horizontal,
$<$ ±6% of reading for wind vectors within ±20° of horizontal.

Wind direction
Azimuth range: ±170°.
Elevation Range: ±60.0°.
Resolution: 0.06°.
Accuracy: ±0.7° for horizontal wind of 1 ms^{-1}.

Sonic temperature
Range: -30 to 50 °C.
Resolution: 0.01 °C.
Accuracy: ±2°C.

C.3 Vaisala TTS111

The Vaisala TTS111 (Fig. C.4) was the operative tethered-balloon at Sagebrush. The temperature is detected using a bead sensor, while the relative humidity is retrieved

thanks to a thin-film polymer sensor, i.e. a thin film of polymer deposited between two conductive electrodes. The tethered-balloon is equipped with a three-cup anemometer coupled with a light chopper disk to measure the wind speed. The wind direction is detected with a digital compass. The following list summarised the specifications for this instrumentation.

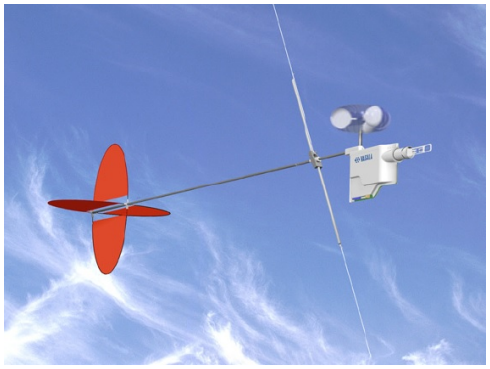

Figure C.4: Vaisala TTS111 tethered-balloon.

Wind speed
Range: 0 to 20 ms^{-1}.
Resolution: 0.1 ms^{-1}.

Wind direction
Range: 0 to 360 °.
Resolution: 1°.

Temperature
Range: -50 to 60 °C.
Resolution: 0.1 °C.
Accuracy: ±0.5 °C.

Relative Humidity
Range: 0 to 100 %.
Resolution: 0.1%.
Accuracy: ±5%.

C.4 Graw DFM-09

The radiosondes Graw DFM-09 (Fig. C.5) were launched in Sagebrush to measure the geostrophic wind, temperature and humidity profiles. The following list summarised the specifications for this instrumentation.

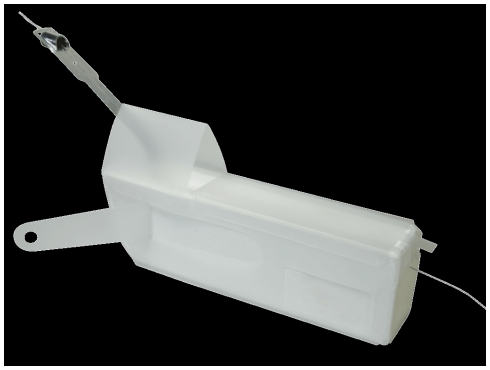

Figure C.5: Graw Radiosondes DFM-09.

Accuracy of horizontal position: < 5 m.

Wind speed Accuracy: < 0.2 ms^{-1}.

Temperature
Resolution: 0.1 °C.
Accuracy: < 0.22 °C.

Relative Humidity
Resolution: 1%.
Accuracy: < 4%.

C.5 Young 05103

The Young 05103 is the vane anemometer, the MINISAMS and SAMS are equipped with. The wind-speed sensor consists of four blade helical propeller, while the wind direction sensor is a rugged yet lightweight vane. The following list summarised the specifications for this instrumentation.

Wind speed
Range: 0 to 100 ms^{-1}.
Accuracy: ± 0.3 ms^{-1} or 1% of reading.
Threshold: 1.0 ms^{-1}.

Wind direction
Range: 0 to 360 °.
Accuracy: ± 3°.
Threshold: 1.1 ms^{-1}.

C.6 Campbell HMP45C

The Campbell HMP45C are the temperature and relative-humidity probes, the MIN-ISAMS, SAMS and flux towers are equipped with. The temperature is measured through a Platinum Resistance Thermometer (PRT), while the relative humidity is detected thanks to a thin-film polymer sensor. The following list summarised the specifications for this instrumentation.

Temperature
Range: -39.2 to 60 °C.
Accuracy:
±0.5 °C at -40 °C,
±0.4 °C at -20 °C and 60 °C,
±0.3 °C at 0 °C and 40 °C,
±0.2 °C at 20 °C.

Relative Humidity (RH)
Range: 0.8 to 100 %.
Accuracy:
±2% for RH from 0 to 90 %,
±3% for RH from 90 to 100 %.
Temperature dependence: ±0.05% RH $°C^{-1}$.

C.7 Campbell CS106

The Campbell CS106 are the barometers, which were equipped on the flux towers. Each of them is a silicon sensor, i.e. silicon membrane deposited between two conductive electrodes. The following list summarised the specifications for this instrumentation.

Pressure
Range: 500 to 1100 hPa.
Accuracy:
±0.3 hPa at 20 °C,
±0.6 hPa from 0 °C to 40 °C,
±1.0 hPa from -20 °C and 45 °C,
±1.5 hPa from -40 °C and 60 °C.

Bibliography

Albini FA, Latham DJ, Baughman RG (1982) Estimating upslope convective wind speeds for predicting wildland behaviour. 257, Forgotten Books

Allwine KJ, Shinn JH, Streit GE, Clawson KL, Brown M (2002) Overview of Urban 2000: a Multiscale Field Study of Dispersion through an Urban Environment. Bull Am Meteorol Soc 83(4):521–536, DOI 10.1175/1520-0477(2002)083<0521:OOUAMF>2.3.CO;2

Andreas EL, Claffey KJ, Makshtas AP (2000) Low-Level Atmospheric Jets and Inversions over the Wester Weddell Sea. Boundary-Layer Meteorol 97(3):459–486, DOI 10.1023/A:1002793831076

Baas P, Bosveld FC, Baltink HK, Holtslag AAM (2009) A climatology of Nocturnal Low-Level Jets at Cabauw. J Appl Meteorol Clim 48(8):1627–1642, DOI 10.1175/2009JAMC1965.1

Baklanov AA, Grisogono B, Bornstein R, Mahrt L, Zilitinkevich SS, Taylor P, Larsen SE, Rotach MW, Fernando HJ (2011) The Nature, Theory, and Modeling of Atmospheric Planetary Boundary Layers. Bull Am Meteorol Soc 92(2):123–128, DOI 10.1175/2010BAMS2797.1

Banta RM (2008) Stable-boundary-layer regimes from the perspective of the low-level jet. Acta Geophys 56(1):58–87, DOI 10.2478/s11600-007-0049-8

Banta RM, Senff CJ, White AB, Trainer M, McNider RT, Valante RJ, Mayor SD, Alvarez RJ, Hardesty RM, Parrish D, Fehsenfeld FC (1998) Daytime buildup and nighttime transport of urban ozone in the boundary layer during a stagnation episode. J Geophys Res Atmos 103(D17):22,519–22,544, DOI 10.1029/98JD01020

Banta RM, Newsom RK, Lundquist JK, Pichugina YL, Coulter RL, Mahrt L (2002) Nocturnal Low-Level Jet Characteristic over Kansas During CASES-99. Boundary-Layer Meteorol 105(2):221–252, DOI 10.1023/A:1019992330866

Banta RM, Pichugina YL, Newsom RK (2003) Relationship between Low-Level Jet Properties and Turbulence Kinetic Energy in the Nocturnal Stable Boundary Layer. J Atmos Sci 60(20):2549–2555, DOI 10.1175/1520-0469(2003)060<2549:RBLJPA>2.0.CO;2

BIBLIOGRAPHY

Banta RM, Darby LS, Fast JD, Pinto JO, Whiteman DC, Shaw WJ, Orr BW (2004) Nocturnal Low-Level Jet in a Mountain Basin Complex. Part I: Evolution and Effects on Local Flows. J Appl Meteorol 43(10):1348–1365, DOI 10.1175/JAM2142.1

Banta RM, Pichugina YL, Brewer WA (2006) Turbulent Velocity-Variance Profiles in the Stable Boundary Layer Generated by a Nocturnal Low-Level Jet. J Atmos Sci 63:2700–2719, DOI 10.1175/JAS3776.1

Banta RM, Pichugina YL, Kelley ND, Hardesty RM, Brewer WA (2013) Wind Energy Meteorology: Insight into Wind Properties in the Turbine-Rotor Layer of the Atmosphere from High-Resolution Doppler Lidar. Bull Am Meteorol Soc 94(6):883–902, DOI 10.1175/BAMS-D-11-00057.1

Belušić D, Mahrt L (2012) Is geometry more universal than physics in atmospheric boundary layer flow? J Geophys Res 117(9), DOI 10.1029/2011JD016987

Beyrich F (1994) Sodar observations of the stable boundary layer height in relation to the nocturnal low-level jet. Meteorol Z 25(22):29 – 34, DOI 10.1127/metz/3/1994/29

Blackadar AK (1957) Boundary Layer Wind Maxima and Their Significance for the Growth of Nocturnal Inversions. Bull Am Meteorol Soc 38(5):283–290, DOI 10.1175/1520-0477-38.5.283

Bonner WD (1968) Climatology of the Low Level Jet. Mon Weather Rev 96(12):833–850, DOI 10.1175/1520-0493(1968)096<0833:COTLLJ>2.0.CO;2

Bowen BM (1996) Example of Reduced Turbulence during Thunderstorm Outflow. J Appl Meteorol 35(6):1028–1032, DOI 10.1175/1520-0450(1996)035<1028:EORTDT>2.0.CO;2

Carroll BJ, Demoz BB, Delgado R (2019) An Overview of Low-Level Jet Winds and Corresponding Mixed Layer Depths During PECAN. J Geophys Res Atmos 124(16):9141–9160, DOI 10.1029/2019JD030658

Charney JJ, Bian X, Potter BE, Heilman WE (2003) Low Level Jet Impacts on Fire Evolution in the Mack Lake and Other Severe Wildfires. In: 5th Symposium on Fire and Forest Meteorology, American Meteorological Society, Boston

Chemel C, Staquet C, Largeron Y (2009) Generation of internal gravity waves by a katabatic wind in an idealized alpine valley. Meteorol Atmos Phys 103(1-4):187–194, DOI 10.1007/s00703-009-0349-4

Chimonas G (2005) The Nighttime Accelerations of the Wind in the Boundary Layer. Boundary-Layer Meteorol 116(3):519–531, DOI 10.1007/s10546-005-0609-x

Clark RD, Philbrick CR, Ryan WF, Doddridge BG, Stehr JW (2002) The Effects of Local and Regional Scale Circulations on Air Pollutants AIR During NARSTO-NEOPS 1999-2001. In: Fourth Conference on Atmospheric Chemistry, Am Meteorol Soc, Orlando, FL

Cole RE, Allan SS, Miller DW (2000) Vertical Wind Shear Near Airports as an Aviation Hazard. In: Ninth Conference on Aviation, Range, and Aerospace Meteorology, American Meteorological Society, Orlando

Conangla L, Cuxart J (2006) On the turbulence in the upper part of the low-level jet: an experimental and numerical study. Boundary-Layer Meteorol 118(2):379–400, DOI 10.1007/s10546-005-0608-y

Curtis RC, Panofsky HA (1958) The Relation Between Large-Scale Vertical Motion and Weather in Summer. Bull Am Meteorol Soc 39(10):521–531, DOI 10.1175/1520-0477-39.10.521

Darby LS, Banta RM, Brewer WA, Neff WD, Marchbanks RD, McCarty BJ, Senff CJ, White AB, Angevine WM, Williams EJ (2002) Vertical variations in O3 concentrations before and after a gust front passage. J Geophys Res Atmos 107(13), DOI 10.1029/2001JD000996

De Wekker S (2017) Grawmet Radiosonde System Sage Brush Launch site Data. Version 1.0. UCAR/NCAR - Earth Observing Laboratory. DOI 10.5065/D6GX490T

Delgado R, Rabenhorst SD, Demoz BB, Hoff RM (2015) Elastic lidar measurements of summer nocturnal low level jet events over Baltimore, Maryland. J Atmos Chem 72(3-4):311–333, DOI 10.1007/s10874-013-9277-2

Drake VA, Farrow RA (1988) The Influence of Atmospheric Structure and Motions on Insect Migration. Ann Rev Entomol 33:183–210, DOI 10.1146/annurev.en.33.010188.001151

Drazin PG (2002) Introduction to Hydrodynamics Stability. Cambridge University Press, DOI 10.1017/CBO9780511809064

Droegemeier KK, Wilhelmson RB (1987) Numerical Simulation of Thunderstorm Outflow Dynamics. Part I: Outflow Sensitivity Experiments and Turbulence Dynamics. J Atmos Sci 44(8):1180–1210, DOI 10.1175/1520-0469(1987)044<1180:NSOTOD>2.0.CO;2

Ellis AW, Hildebrandt ML, Thomas WM, Fernando HJS (2000) Analysis of the climatic mechanisms contributing to the summertime transport of lower atmospheric ozone across metropolitan Phoenix, Arizona, USA. Clim Res 15:13–31, DOI 10.3354/cr015013

Farquharson SJ (1939) The Diurnal Variation of Wind Over Tropical Africa. Q J R Meteorol Soc 65:165–183, DOI 10.1002/qj.49706528004

Fernando HJ, Verhoef B, Di Sabatino S, Leo LS, Park S (2013) The Phoenix Evening Transition Flow Experiment (TRANSFLEX). Boundary-Layer Meteorol 147(3):443–468, DOI 10.1007/s10546-012-9795-5

Fernando HJS (2017) Vaisala DigiCORA Tethersonde System Data Sage Brush Site. Version 1.0. UCAR/NCAR - Earth Observing Laboratory. DOI 10.5065/D6XS5SVV

Fernando HJS, Weil JC (2010) Whither the stable boundary layer? A shift in the research agenda. Bull Am Meteorol Soc 91:1475–1484, DOI 10.1175/2010BAMS2770.1

Fernando HJS, Pardyjak ER, Di Sabatino S, Chow FK, De Wekker SFJ, Hoch SW, Hacker J, Pace JC, Pratt T, Pu Z, Steenburgh WJ, Whiteman CD, Wang Y, Zajic D, Balsley B, Dimitrova R, Emmitt GD, Higgins CW, Hunt JCR, Knievel JC, Lawrence D, Liu Y, Nadeau DF, Kit E, Blomquist BW, Conry P, Coppersmith RS, Creegan E, Felton M, Grachev A, Gunawardena N, Hang C, Hocut C, Huynh G, Jeglum ME, Jensen D, Kulandaivelu V, Lehner M, Leo LS, Liberzon D, Massey JD, McEnerney K, Pal S, Price T, Sghiatti M, Silver Z, Thompson M, Zhang H, Zsedrovits T (2015) THE MATERHORN Unraveling the Intricacies of Mountain Weather. Bull Am Meteorol Soc 96(11):1945–1967, DOI 10.1175/BAMS-D-13-00131.1

Fiedler S, Schepanski K, Heinold B, Knippertz P, Tegen I (2013) Climatology of nocturnal low-level jets over North Africa and implications for modeling mineral dust emission. J Geophys Res Atmos 118(12):6100–6121, DOI 10.1002/jgrd.50394

Goualt J (1938) Vents en Altitude a Fort Lamy (Tchad). Annales de Physique du Globe de la France d'Outre-Mer 5:70–91

Grachev AA, Leo LS, Di Sabatino S, Fernando HJ, Pardyjak ER, Fairall CW (2016) Structure of Turbulence in Katabatic Flows Below and Above the Wind-Speed Maximum. Boundary-Layer Meteorol 159(3):469–494, DOI 10.1007/s10546-015-0034-8

Hang C, Nadeau DF, Jensen DD, Hoch SW, Pardyjak ER (2016) Playa Soil Moisture and Evaporation Dynamics During the MATERHORN Field Program. Boundary-Layer Meteorol 159(3):521–538, DOI 10.1007/s10546-015-0058-0

Hejstrup J (1993) A Statistical Data Screening Procedure. Meas Sci Technol 4:153–157, DOI 10.1088/0957-0233/4/2/003

Higgins RW, Yao Y, Yarosh ES, Janowiak JE, Mo KC (1997) Influence of the Great Plains Low-Level Jet on Summertime Precipitation and Moisture Transport over the Central United States. J Clim 10(3):481–507, DOI 10.1175/1520-0442(1997)010<0481:IOTGPL>2.0.CO;2

Hoecker WHJ (1963) Three Southerly Low-Level Jet Systems Delineated by the Weather Bureau Special Pibal Network of 1961. Mon Weather Rev 91:573–582, DOI 10.1175/1520-0493(1963)091<0573:TSLJSD>2.3.CO;2

Holton JR (1967) The diurnal boundary layer wind oscillation above sloping terrain. Tellus 19(2):200–205, DOI 10.3402/tellusa.v19i2.9766

Hu XM, Klein PM, Xue M, Lundquist JK, Zhang F, Qi Y (2013) Impact of Low-Level Jets on the Nocturnal Urban Heat Island Intensity in Oklahoma City. J App Meteor Clim 52(8):1779–1802, DOI 10.1175/JAMC-D-12-0256.1

Hunt JCR (1985) Diffusion in the Stably Stratified Atmospheric Boundary Layer. J Clim Appl Meteorol 24(11):1187–1195, DOI 10.1175/1520-0450(1985)024<1187:DITSSA>2.0.CO;2

Isard SA, Gage SH (2001) Flow of Life in the Atmosphere: an Airscape Approach to Understanding Invasive Organisms. Michigan State University Press

Jensen DD, Nadeau DF, Hoch SW, Pardyjak ER (2016) Observations of Near-Surface Heat-Flux and Temperature Profiles Through the Early Evening Transition over Contrasting Surfaces. Boundary-Layer Meteorol 159(3):567–587, DOI 10.1007/s10546-015-0067-z

Kallistratova MA, Kouznetsov RD (2012) Low-Level Jets in the Moscow Region in Summer and Winter Observed with a Sodar Network. Boundary-Layer Meteorol 143(1):159–175, DOI 10.1007/s10546-011-9639-8

Kalverla PC, Duncan JBJ, Steeneveld GJ, Holtslag AA (2019) Low-level jets over the North Sea based on ERA5 and observations: together they do better. Wind Energy Sci 4(2):193–209, DOI 10.5194/wes-4-193-2019

Kang Y, Belušić D, Smith-Miles K (2014) Detecting and Classifying Events in Noisy Time Series. J Atmos Sci 71(3):1090–1104, DOI 10.1175/JAS-D-13-0182.1

Karipot A, Leclerc MY, Zhang G, Martin T, Starr G, Hollinger D, McCaughey JH, Hendrey GR (2006) Nocturnal CO2 exchange over a tall forest canopy associated with intermittent low-level jet activity. Theor Appl Clim 85(3-4):243–248, DOI 10.1007/s00704-005-0183-7

Kim J, Mahrt L (1992) Momentum Transport by Gravity Waves. Americ Meteorol Soc 49(9):735–748

Klein PM, Hu XM, Xue M (2014) Impacts of Mixing Processes in Nocturnal Atmospheric Boundary Layer on Urban Ozone Concentrations. Boundary-Layer Meteorol 150(1):107–130, DOI 10.1007/s10546-013-9864-4

Kotroni V, Lagouvardos K (1993) Low-Level Jet Streams Associated with Atmospheric Cold Fronts: Seven Case Studies from the FRONTS 87 Experiment. Geophys Res Lett 20(13):1371–1374, DOI 10.1029/93GL01701

BIBLIOGRAPHY

Leo LS, Thompson MY, Di Sabatino S, Fernando HJ (2016) Stratified Flow Past a Hill: Dividing Streamline Concept Revisited. Boundary-Layer Meteorol 159(3):611–634, DOI 10.1007/s10546-015-0101-1

Lettau HH (1967) Small to large scale features of boundary !ayer structure o ver mountain slopes. In: Proceedings of the Symposium on Mountain Meteorology, Fort Collins, pp 10–74

Liechti F, Schaller E (1999) The Use of Low-Level Jets by Migrating Birds. Naturwissenschaften 86:549–551, DOI 10.1007/s001140050673

Lu R, Turco RP (1994) Air Pullutant Transport in a Coastal Environment. Part I: Two-Dimensional Simulations of Sea-Breeze and Mountain Effects. J Atmos Sci 51(15):2285–2308, DOI 10.1175/1520-0469(1994)051<2285:APTIAC>2.0.CO;2

Lundquist JK, Mirocha JD (2008) Interaction of Nocturnal Llow-Level Jets with Urban Geometries as Seen in Joint Urban 2003 Data. J Appl Meteorol Clim 47(1):44–58, DOI 10.1175/2007JAMC1581.1

Mahrt L (1989) Intermittency of Atmospheric Turbulence. J Atmos Sci 46(1):79–95, DOI 10.1175/1520-0469(1989)046<0079:IOAT>2.0.CO;2

Mahrt L (2009) Characteristics of Submeso Winds in the Stable Boundary Layer. Boundary-Layer Meteorol 130(1):1–14, DOI 10.1007/s10546-008-9336-4

Mahrt L (2010) Common microfronts and other solitary events in the nocturnal boundary layer. Q J R Meteor Soc 136(652):1712–1722, DOI 10.1002/qj.694

Mahrt L, Richardson S, Seaman N, Stauffer D (2012) Turbulence in the nocturnal boundary layer with light and variable winds. Q J R Meteorol Soc 138(667):1430–1439, DOI 10.1002/qj.1884

Mamrosh RD, Daniels TS, Moninger WR (2006) Aviation Applications of TAMDAR Aircraft Data Reports. In: 12th Conference on Aviation Range and Aerospace Meteorology, American Meteorological Society, Atlanta

Mathieu N, Strachan IB, Leclerc MY, Karipot A, Pattey E (2005) Role of low-level jets and boundary-layer properties on the NBL budget technique. Agric For Meteorol 135(1-4):35–43, DOI 10.1016/j.agrformet.2005.10.001

Mayr GJ, Armi L, Gohm A, Zängl G, Durran DR, Flamant C, Gaberšek S, Mobbs S, Ross A, Weissmann M (2007) Gap flows: Results from the Mesoscale Alpine Programme. Q J R Meteorol Soc 133(625 B):881–896, DOI 10.1002/qj.66

McMillen RT (1988) An Eddy Correlation Technique with Extended Applicability to Non-Simple Terrain. Boundary-Layer Meteorol 43(3):231–245, DOI 10.1007/BF00128405

Means LL (1952) On Thunderstorm Forecasting in the Central United States. Mon Weather Rev 80(10):165–189, DOI 10.1175/1520-0493(1952)080<0165:OTFITC>2.0.CO;2

Mitchell MJ, Arritt RW, Labas K (1995) A Climatology of the Warm Season Great Plains Low-Level Jet Using Wind Profiler Observations. Weather Forecast 10:576–591, DOI 1520-0434(1995)010<0576:ACOTWS>2.0.CO;2

Monti P, Fernando HJS, Princevac M, Chan WC, Kowalewski TA, Pardyjak ER (2002) Observations of Flow and Turbulence in the Nocturnal Boundary Layer over a Slope. J Atmos Sci 59(17):2513–2534, DOI 10.1175/1520-0469(2002)059<2513:OOFATI>2.0.CO;2

Nieuwstadt FTM (1985) A model for the stationary, stable boundary layer. Clarendon Press

Ohya Y, Nakamura R, Uchida T (2008) Intermittent Bursting of Turbulence in a Stable Boundary Layer with Low-Level Jet. Boundary-Layer Meteorol 126(3):349–363, DOI 10.1007/s10546-007-9245-y

Orlanski I (1975) A Rational Subdivision of Scales for Atmospheric Processes. Bull Am Meteorol Soc 56(5):527–530

Orr A, Hunt J, Capon R, Sommeria J, Cresswell D, Owinoh A (2005) Coriolis effects on wind jets and cloudiness along coasts. Weather 60(10):291–299, DOI 10.1256/wea.219.04

Pace J (2016a) Surface Atmospheric Measurement Stations Mini Network 1 Minute Average Data located to East and South East of granite Peak. Version 1.0. UCAR/NCAR - Earth Observing Laboratory. DOI 10.5065/D6J101K8

Pace J (2016b) Surface Atmospheric Measurement Systems 5 Minute Average Data Surrounding Granite Peak. Version 1.0. UCAR/NCAR - Earth Observing Laboratory. DOI 10.5065/D6DB806T

Pace J (2017) MATERHORN-X Tower Data. Version 1.0. UCAR/NCAR - Earth Observing Laboratory. DOI 10.5065/D67W69X5

Paegle J, Rasch GE (1973) Three-Dimensional Characteristics of Diurnally Varying Boundary-Layer Flows. Mon Weather Rev 101(10):746–756, DOI 10.1175/1520-0493(1973)101<0746:TCODVB>2.3.CO;2

Parish TR (1982) Barrier Winds Along the Sierra Nevada Mountains. J Appl Meteorol 21(7):925–930, DOI 10.1175/1520-0450(1982)021<0925:BWATSN>2.0.CO;2

Parish TR (2000) Forcing of the Summertime Low-Level Jet along the California Coast. J Appl Meteorol 39(12):2421–2433, DOI 10.1175/1520-0450(2000)039<2421:FOTSLL>2.0.CO;2

Parish TR (2017) On the Forcing of the Summertime Great Plains Low-Level Jet. J Atmos Sci 74(12):3937–3953, DOI 10.1175/JAS-D-17-0059.1

Pichugina YL, Banta RM, Kelley ND (2007) Analysis of the Southern Colorado Low-Level Jet by High Resolution Doppler Lidar Data. Comparison to the Great Plains LLJ Climatologies. In: 87th AMS Annual Meeting, Third Symposium on LIDAR Atmospheric Applications, San Antonio, Texas

Pitchford KL, London J (1962) The Low-Level Jet as Related to Nocturnal Thunderstorms over Midwest United States. J Appl Meteorol 1(1):43–47, DOI 10.1175/1520-0450(1962)001<0043:TLLJAR>2.0.CO;2

Politovich MK, Goodrich RK, Morse CS, Yates A, Barron R, Cohn SA (2011) The Juneau Terrain-Induced Turbulence Alert System. Bull Am Meteorol Soc 92(3):299–313, DOI 10.1175/2010BAMS3024.1

Princevac M, Fernando HJS (2008) Morning breakup of cold pools in complex terrain. J Fluid Mech 616:99–109, DOI 10.1017/S0022112008004199

Princevac M, Fernando HJS, Whiteman CD (2005) Turbulent entrainment into natural gravity-driven flows. J Fluid Mech 533:259–268, DOI 10.1017/S0022112005004441

Pu B, Dickinson RE (2014) Diurnal Spatial Variability of Great Plains Summer Precipitation Related to the Dynamics of the Low-Level Jet. J Atmos Sci 71(5):1807–1817, DOI 10.1175/JAS-D-13-0243.1

Ranjha R, Tjernström M, Semedo A, Svensson G, Cardoso RM (2015) Structure and variability of the Oman coastal low-level jet. Tellus A 67(1), DOI 10.3402/tellusa.v67.25285

Renfrew IA, Anderson PS (2006) Profiles of katabatic flow in summer and winter over Coats Land, Antarctica. Q J R Meteorol Soc 132(616):779–802, DOI 10.1256/qj.05.148

Schmid HP, Grimmond CSB, Cropley F, Offerle B, Su HB (2000) Measurements of CO2 and Energy Fluxes over a Mixed Hardwood Forest in the Mid-Western United States. Agric For Meteorol 103(4):357–374, DOI 10.1016/S0168-1923(00)00140-4

Shapiro A, Fedorovich E (2009) Nocturnal low-level jet over a shallow slope. Acta Geophys 57(4):950–980, DOI 10.2478/s11600-009-0026-5

Song J, Liao K, Coulter RL, Lesht BM (2005) Climatology of the Low-Level Jet at the Southern Great Plains Atmospheric Boundary Layer Experiments Site. J Appl Meteorol 44(10):1593–1606, DOI 10.1175/JAM2294.1

Staquet C, Sommeria J (2002) Internal Gravity Waves: From Instabilities to Turbulence. Annu Rev Fluid Mec 34:559–593

Stauffer DR, Warner TT (1987) A Numerical Study of Appalachian Cold-Air Damming and Coastal Frontogenesis. Mon Weather Rev 115(4):799–821, DOI doi:10.1175/1520-0493(1987)115<0799:ANSOAC>2.0.CO;2

Stommel H (1948) The Westward Intensification of Wind-Driven Ocean Currents. Trans AGU 29(2):202–206, DOI 10.1029/TR029i002p00202

Storm B, Dudhia J, Basu S, Swift A, Giammanco I (2009) Evaluation of the weather research and forecasting model on forecasting low-level jets: implications for wind energy. Wind Energy 12(1):81–90, DOI 10.1002/we.288

Stull RB (1988) An introduction to boundary layer meteorology. Kluwer Academic Publishers

Su J, Felton M, Lei L, McCormick MP, Delgado R, St Pé A (2016) Lidar remote sensing of cloud formation caused by low-level jets. J Geophys Res Atmos 121(10):5904–5911, DOI 10.1002/2015JD024590

Sun J, Nappo CJ, Mahrt L, Belušic D, Grisogono B, Stauffer DR, Pulido M, Staquet C, Jiang Q, Pouquet A, Yagüe C, Galperin B, Smith RB, Finnigan JJ, Mayor SD, Svensson G, Grachev AA, Neff WD (2015) Review of wave-turbulence interactions in the stable atmospheric boundary layer. Rev Geophys 53(3):956–993, DOI 10.1002/2015RG000487

Thunis P, Bornstein R (1996) Hierachy of Mesoscale Flow Assumptions and Equations. J Atmos Sci 53(3):380–397, DOI 10.1175/1520-0469(1996)053<0380:HOMFAA>2.0.CO;2

Tuononen M, O'Connor EJ, Sinclair VA, Vakkari V (2017) Low-level Jets over Utö, Finland, Based on Doppler Lidar Observations. J Appl Meteorol Clim 56(9):2577–2594, DOI 10.1175/JAMC-D-16-0411.1

University of Utah (2017) University of Utah Project Photographs. Version 1.0. UCAR/NCAR - Earth Observing Laboratory. DOI 10.5065/D6765D1G

Van de Wiel BJH, Moene A, Hartogensis O, de Bruin HAR, Holtslag AAM (2002) Intermittent turbulence in the stable boundary layer over land. Part I: a bulk model. J Atmos Sci 59:942–958, DOI 10.1175/1520-0469(2002)059<0942:ITAOIT>2.0.CO;2

Van de Wiel BJH, Moene AF, Steeneveld GJ, Baas P, Bosveld FC, Holtslag AAM (2010) A conceptual view on inertial oscillations and nocturnal low-level jets. J Atmos Sci 67(8):2679–2689, DOI 10.1175/2010JAS3289.1

Van Ulden AP, Wieringa J (1996) Atmospheric Boundary Layer Research at Cabauw. Boundary-Layer Meteorol 78:39–69, DOI 10.1007/978-94-017-0944-6_3

Vanderwende BJ, Lundquist JK, Rhodes ME, Takle ES, Irvin SL (2015) Observing and Simulating the Summertime Low-Level Jet in Central Iowa. Mon Weather Rev 143(6):2319–2336, DOI 10.1175/MWR-D-14-00325.1

Vickers D, Mahrt L (1997) Quality Control and Flux Sampling Problems for Tower and Aircraft Data. J Atmos Ocean Technol 14(3):512–526, DOI 10.1175/1520-0426(1997)014<0512:QCAFSP>2.0.CO;2

Walters CK, Winkler JA, Shadbolt RP, van Ravensway J, Bierly GD (2008) A Long-Term Climatology of Southerly and Northerly Low-Level Jets for the Central United States. Ann Assoc Am Geographers 98(3):521–552, DOI 10.1080/00045600802046387

Wang Y, Klipp CL, Garvey DM, Ligon DA, Williamson CC, Chang SS, Newsom RK, Calhoun R (2007) Nocturnal Low-LeveL-Jet-Dominated Atmospheric Boundary Layer Observed by a Doppler Lidar over Oklahoma City during JU2003. J Appl Meteorol Clim 46(12):2098–2109, DOI 10.1175/2006JAMC1283.1

Westbrook JK (2008) Noctuid migration in Texas within the nocturnal aeroecological boundary layer. Integr Compar Biol 48(1):99–106, DOI 10.1093/icb/icn040

Westbrook JK, Isard SA (1999) Atmospheric scales of biotic dispersal. Agric For Meteorol 97:263–274, DOI 10.1016/S0168-1923(99)00071-4

Wexler H (1961) A Boundary Layer Interpretation of the Low-level Jet. Tellus 13(3):369–378, DOI https://doi.org/10.1111/j.2153-3490.1961.tb00098.x

Whiteman CD, Bian X, Zhong S (1997) Low-Level Jet Climatology from Enhanced Rawinsonde Observations at a Site in the Southern Great Plains. J Appl Meteorol 36(10):1363–1367, DOI 10.1175/1520-0450(1997)036<1363:LLJCFE>2.0.CO;2

Winters HA, Galloway Jr GA, Reynolds WJ, Rhyne DW (2001) Battling the Elements: Weather and Terrain in the Conduct of War. Johns Hopkins University Press

Wolf WW, Westbrook JK, Raulston J, Pair SD, Hobbs SE, Riley JR, Mason PJ, Joyce RJV (1990) Recent Airborne Radar Observations of Migrant Pests in the United States [and Discussion]. Philos Trans R Soc 328(1251):619–630, DOI doi.org/10.1098/rstb.1990.0132

Zhang F, Pu Z (2019) Sensitivity of numerical simulations of near-surface atmospheric conditions to snow depth and surface albedo during an ice fog event over Heber Valley. J Appl Meteorol Clim 58(4):797–811, DOI 10.1175/JAMC-D-18-0064.1

Zhu M, Radcliffe EB, Ragsdale DW, MacRae IV, Seeley MW (2006) Low-level jet streams associated with spring aphid migration and current season spread of potato viruses in the U.S. northern Great Plains. Agric For Meteorol 138(1-4):192–202, DOI 10.1016/j.agrformet.2006.05.001

Zilitinkevich SS (1972) On the Determination of the Height of the Ekman Boundary Layer. Boundary-Layer Meteorol 3:141–145, DOI 10.1007/BF02033914

Ringraziamenti

In primis, ringrazio i miei genitori. Non è facile scrivere delle motivazioni per questo primo ringraziamento, o meglio, è difficile elencare tutte le motivazioni.
Ringrazio la Professoressa Silvana Di Sabatino per avermi guidato magistralmente durante questo anno di lavoro. La ringrazio sia per il supporto professionale e la dedizione nel seguirmi, che per come trasmette passione per gli argomenti trattati.
Ringrazio il Dottore Francesco Barbano per l'incommensurabile aiuto e la Dottoressa Laura Sandra Leo per esserci sempre stata nel momento del bisogno.
Ringrazio i dottorandi per avermi accolto e trasmesso serenità.
Ringrazio i miei compagni di corso perchè mi sono trovato molto bene con loro. Senza di loro quest'avventura durata 2 anni circa sarebbe stata peggiore.
Ringrazio tutto il mondo Camplus, specialmente il mio compagno di stanza Davide per avermi sopportato (nel vero senso della parola). Spesso altri studenti Camplus mi hanno detto che appaio sempre felice e sorridente, ma credo che, senza loro, lo sarei stato di meno durante la mia esperienza bolognese.
Ringrazio tutte le persone che ho incontrato nella vita e che ancora oggi rappresentano un solido supporto per me, come nonna Maria, zia Graziella, zio Francesco e i miei tre cugini Maria, Giovanni e Ivan; gli ex professori con cui ho ancora contatto; i miei amici Chiara, Francesca R., Francesca T. e Walter.
Concludo con un ringraziamento strano: ringrazio il Forum di Cosenza Meteo, ormai non più esistente, ma che ha contribuito in modo sostanziale a far crescere in me la passione per la meteorologia quando ero piccolo.